Chapter 1

Review

1.1 Introduction

One of the most fundamental problems of Wind Engineering is the estimation of cross flow vibration response amplitudes of slender structures with circular cross sections. Examples of the structures concerned are chimney stacks, flare towers and oil-rig jacket members. Typically the flows involved are characterized by high Reynolds numbers ($Re > 10^5$) and moderate turbulence intensities ($I_u < 20\%$). Vibration response amplitudes usually must lie below 5% of diameter, to prevent the possibility of large amplitudes and stresses caused by lock-in effects.

Despite the fundamental nature of the problem, estimates of cross flow response of full scale structures are still relatively inaccurate. Estimates of response of chimney stacks published by Vickery and Basu (1984) show a coefficient of variation between measured and estimated responses of 25%, while data presented in ESDU 85038 (1985) reveal a similar level of variation. Part of the variation can be attributed to difficulties with the observed responses, but the lack of relevant aerodynamic data is a large contributing factor. The data required are the co-spectra of cross flow forces acting on different sections of the structure, and description of motion-dependent forces, which are observed even at low amplitudes of motion. Very few wind tunnel measurements of cross flow forces in turbulent flows and at the required Reynolds numbers have been published. Only one study (Jones, Cincotta & Walker 1969) has dealt with motion-dependent forces on smooth cylinders at these Reynolds numbers, and that was carried out in smooth flow.

1.1.1 Research Aims

The research described in this thesis is concerned with measuring cross flow (lift) forces which act on smooth circular cylinders in turbulent flows. As implied above, the overall goal of the work is to provide data relevant to the prediction of cross flow response amplitudes of slender circular cylindrical structures (such as chimney stacks) in turbulent flows of high Reynolds number. Emphasis is placed on responses of comparatively low amplitudes (less than 5% of diameter), which are relevant to many civil engineering structures.

In particular, the role of turbulence in changing lift forces which act on motionless cylinders in the supercritical and transcritical Reynolds number regimes is examined. The first aim in this section of work is to discover if high Reynolds number, highly turbulent flows exhibit Reynolds number independence at lower Reynolds numbers than is the case in smooth flows. The second is to establish if the forces measured in wind tunnel turbulence of comparatively small integral scale to diameter ratios are similar to those which act on full scale structures in natural flows, where the integral scale of turbulence is comparatively much larger.

The influence of forced, low amplitude cylinder oscillation on lift forces in smooth and turbulent flows is then examined. The aim is to measure the magnitude of motion-induced forces in turbulent flows, and to establish the extent to which cylinder motion is able to influence the vortex shedding processes. In addition, the forces which act on a cylinder in smooth subcritical flow are studied with the aim of understanding the mechanism of motion-induced forces at low cylinder oscillation amplitudes.

1.1.2 Outline of Thesis

The thesis describes an experimental programme which was designed to answer questions raised in relation to the aims discussed above.

This chapter is a review of material relevant to the study of cross flow forces and prediction of response amplitudes.

Chapters 2, 3 and 4 describe the experimental equipment, wind tunnel flows and data processing methods respectively.

The results obtained with a fixed cylinder in smooth and turbulent flows for the Reynolds number range $1 \times 10^5 < Re < 6 \times 10^5$ are discussed in chapter 5.

In chapter 6, the results for a cylinder which was forced to oscillate cross flow at amplitudes up to 3% of diameter are presented and discussed.

Finally, in chapter 7, the overall conclusions for the experimental programme are drawn, and recommendations for future research are made.

1.1.3 Review Outline

In this chapter, space is given in § 1.2 to a description of the vortex shedding process, the fundamental cause of both along and cross flow forces. Then, because of its importance in the study of flows past circular cylinders, the topic of Reynolds number transitions is dealt with in § 1.3. This is followed in § 1.4 by a discussion of the characteristics of the interaction which occurs between vortex shedding and cylinder motion.

After the general nature of the discussion in those sections, more direct emphasis is placed on cross flow forces in §§ 1.5 and 1.6 which deal with forces on stationary and oscillating cylinders. Finally the problem of cross flow response prediction is addressed, and various different models for this task are surveyed in § 1.7.

The chapter ends with § 1.8, a summary of the various specific issues which were addressed in the experimental programme.

In general, the thesis nomenclature has been adhered to, except in cases where data have been reproduced from other works, in which case their nomenclature may have been used and defined.

1.1.4 Dimensionless Groups

Before tackling the properties of vortex-structure interaction, it is useful to consider the relevant dimensionless groups. In smooth flows past fixed cylinders of given geometry, the Reynolds number $Re = UD/\nu$ is the most important parameter; in the simplest case of turbulent flow (isotropic turbulence), the turbulence length scale ratio (LSR) L_u^x/D and the intensity $I_u = \sigma_u/U$ are also important. The geometry of the cylinder is described by the aspect ratio (AR = L/D). The surface roughness of the cylinder can have a pronounced effect on the flow; the roughness is described by a characteristic length ϵ, or non-dimensionally by ϵ/D.

For an oscillating cylinder free to move, the dimensionless amplitude $\alpha = y/D$ and the reduced velocity $V_r = U/fD$ describe the amplitude and frequency of oscillation. The reduced velocity may be interpreted in a number of ways; perhaps the most useful is to consider it as the number of cylinder diameters the mean flow moves in one cylinder oscillation period.

For the simplest case of a freely-vibrating cylinder, the cylinder translates uniformly, and mode shapes do not need to be considered. For a cylinder with distributed properties mass per unit length (m), damping coefficient per unit length (c) and stiffness per unit length (k) (or equivalently m, ζ and f_n), the critical damping ratio ζ and the mass ratio $m/\rho D^2$ appear as additional dimensionless variables.

If the structure is at resonance, the mass and stiffness forces are in balance and the structural damping and mass ratio may be combined into one parameter, the so-called mass-damping parameter[1] $K_s = \zeta m/\rho D^2$. As Vandiver (1985) points out, this parameter helps to characterize the ratio of the forces produced by the fluid flow per unit length to the structural damping forces per unit length, which is more obvious when K_s is rearranged to give $K_s = c/4\pi f_n \rho D^2$. The mass of the structure serves to influence the frequency of oscillation.

1.2 The Vortex Shedding Process

Vortex shedding is caused by interaction between oppositely signed vorticity which is convected away from the two sides of the cylinder by the mean flow. Despite the seeming simplicity of the boundary conditions, the flow which results is complex and not fully understood, even though considerable research effort has been expended on it. The detailed character of the flow is sensitive to Reynolds number, cylinder surface roughness and turbulence in the oncoming flow, as well as the aspect ratio of the cylinder. The flow is also influenced by motion of the cylinder, but in this section attention is restricted to vortex shedding for fixed cylinders.

[1] This is related to the Scruton number $2\delta m/\rho D^2 = 4\pi K_s$. Here δ is the log-decrement of the structural damping.

At very low Reynolds numbers, convection and diffusion of vorticity compete for dominance of the flow around the cylinder. At Reynolds numbers near 6, convection of vorticity to the downstream side of the cylinder produces a pair of closed, counter-rotating standing vortices, known as Föppl vortices. Similar vortices are produced by impulsively starting a cylinder from rest (see e.g. Batchelor 1967, pl. 10). The remainder of the fluid flows past this separated region and converges downstream to form a laminar wake. At low Reynolds numbers (< 30), the vorticity in the wake is able to cross-annihilate to form a stable flow. The transition of flows at these low Reynolds numbers has been described by Batchelor.

Starting at $\mathrm{Re} = 40$, instability is observed as a waviness in the wake, progressing to laminar vortex shedding by $\mathrm{Re} = 70$. This progression, visualized by dye streaklines, is illustrated by Tritton (1988, fig. 3.5). Many flow visualization studies of the laminar regime have been carried out; Van Dyke (1982) gives a representative selection.

The streaklines of vortex shedding reveal a characteristic array of interlaced vortices of opposite sign. This array is known as a Kármán vortex street, since the mathematical analysis which shows that only a regular staggered array of linear vortices is stable was first published by von Kármán in 1912[2]. Birkhoff (1953) showed that the fixed ratio of transverse to longitudinal spacing of the vortices deduced by von Kármán does not generally hold true, as examination of experimental results such as those in Van Dyke's book reveals. The vortices of each sign are produced by the rolling up of vorticity-bearing fluid produced on each side of the cylinder, alternately from one side and the other. It is this rolling up behind the cylinder which constitutes the vortex shedding process.

Although there are many transitions in the boundary and shear layers produced by progression of Reynolds number, as discussed by Zdravkovich (1990, see table 1.3.4) and in § 1.3 below, it seems likely that the basic mechanism of vortex shedding remains unchanged from Reynolds numbers of around 100 up to the highest observed ($\sim 10^9$). This hypothesis is supported by the fact that vortex shedding has been observed for a wide range of Reynolds numbers and for a variety of bluff shapes, from flat plates to mountains. The fact that the Strouhal number for a circular cylinder remains relatively constant near the value of 0.2 over a very wide range of Reynolds numbers also indicates that the basic mechanism remains the same. Despite this, no simple physical explanation for the mechanism of vortex shedding has achieved widespread acceptance.

Recent work (see Huerre & Monkewitz 1990, Oertel 1990) shows that the cause of vortex shedding is a region of absolute instability immediately downstream of the cylinder. This is shown by applying the Orr-Sommerfeld equation to the steady-state solution of the Navier-Stokes equations for the flow around the cylinder. These explanations for the source of the instability are not yet able to describe the mechanics of the "saturation state" which results—vortex shedding.

Vortex shedding may be suppressed by the introduction of objects such as "splitter plates" into the wake, thus preventing the interaction of shear layers (Roshko 1954). Other passive means, such as the "control cylinder" used by Strykowski and Sreenivasan (1990), have been shown to suppress vortex shedding, while helical strakes act to disrupt vortex shedding by reducing the spanwise coherence of vortices. Programmed

[2]The analysis is also presented by Lamb (1945).

(open loop) control by means of spinning the cylinder about its longitudinal axis near the vortex shedding frequency has been shown capable of producing large reduction or increase in the strength of shed vortices (Tokumaru & Dimotakis 1991). The mechanism here is a timed introduction of boundary-layer vorticity into the wake. Active (closed loop) control of vortex shedding by introduction of free-stream velocity perturbations which are phase-locked to a wake velocity signal is also possible (Ffowcs-Williams & Zhao 1989), but not yet well understood.

Various review papers which deal with the vortex shedding process in a general manner have been published, for example those by Morkovin (1964) and Berger and Wille (1972). While some of their material is now out of date, they still provide useful discussion and background. More recently, a paper by Perry, Chong and Lim (1982) has addressed some of the fundamental aspects of the description of the vortex shedding process, dealing in particular with instantaneous streamline patterns and their relationship with streakline patterns. These points are taken up in more detail in the rest of the current section, which deals with observations of vortex shedding downstream of circular cylinders.

1.2.1 Flow Visualization

This section is a review of work related to physical understanding of the vortex shedding process and concentrates on flow visualization results. While many flow visualization experiments have been carried out on the wake flow of cylinders, few have concentrated on the region closest to the cylinder where vortex shedding occurs. In addition, most flow visualization experiments have been carried out at the low end of the Reynolds number range, since they are much easier to conduct at low Reynolds numbers. For this reason, they can only serve as a guide to what happens at higher Reynolds numbers.

Instantaneous Streamlines Instantaneous streamlines of unsteady flows are of interest because they can illustrate indirectly where the low pressure regions in the flow lie, and so give indication of how the forces which act on the body producing the vortices change with time. A complication is that the instantaneous streamlines are not unique: their shape depends on the relative velocity of the observer. The instantaneous streamlines of the vortex shedding process have only begun to be studied quite recently, due in part to the difficulties of measuring them. The measurement methods may be grouped into two sets; those which rely on an instantaneous photographic record of one plane in the flow, and those which give an average picture of the flow at one phase of the vortex shedding process by averaging numerous point measurements of velocity, obtained for example by hotwire or laser-doppler velocimetry.

Of the first set of methods, the simplest to implement is that described by Perry, Chong and Lim (1982), in which a few successive frames of a cine-film of particles moving with the fluid are exposed on one piece of film. If the length of time over which the total exposure is made is short, the streaklines approximate the instantaneous isoclines of the flow field which can be joined up by hand to show the instantaneous streamlines. A related method, which relies on photographic recording of particles carried by the flow, is Particle Image Velocimetry (Pickering & Halliwell 1985). Here, two images of

fluid-bourne particles are captured on one exposure, using rapidly pulsed laser light. Particle velocities may be deduced using Fourier transformation of the captured image.

The methods which rely on many point measurements of velocity made at different times suffer from the lack of simultaneity, since the measurements must be related to a particular phase of the vortex shedding process. This is usually done by using a reference signal which is related to the vortex shedding process, for example a hotwire probe placed near the cylinder but not in the wake. Since the vortex shedding is usually at least slightly random, in that one cycle is never quite the same as the next, the results at each point and at each phase of the process must be averaged to produce the average instantaneous streamlines. This averaging can also be done for the single-image methods discussed above, and is useful in both cases for revealing the "coherent structures" of turbulent flows, including the turbulent wake of cylinders at high Reynolds numbers. Examples of the point measurement method, in which "flying hotwires" were used, are given by Cantwell and Coles (1983), and by Perry and Steiner (1987).

As an alternative to experimental determination of streamlines, computer simulation can be used to examine the streamlines of low Reynolds number flows. Difficulties of measurement do not exist on the computer, although the degree to which local flow details can be resolved depends of course on the accuracy and resolution of the numerical method used. The simulations performed so far have assumed two dimensional flow, so no possibility of three dimensional effects exists, however, to the degree that the vortex shedding process may be considered locally two-dimensional, these simulations provide a useful adjunct to experimental measurements. Eaton (1987) gives details of the computed flow about a circular cylinder at a Reynolds number of 110, including the instantaneous streamlines. A sketch of the instantaneous streamlines computed by Eaton are presented here in figures 1.1 and 1.2. To simplify the sketch, only the *separatrices* (separators) of the instantaneous flow for an observer fixed to the cylinder are shown in figures 1.1 and 1.2. Separatrices join the saddle points of the flow, which are one of the two kinds of critical points which can occur in two-dimensional flows. The closed loops formed by separatrices in the sketch contain pressure minima of the flow which produce fluctuating lift and drag forces on the cylinder. For an extended discussion of critical point terminology, the reader is referred to Perry and Fairlie (1974), Perry and Chong (1987) and Chong, Perry and Cantwell (1990).

The instantaneous streamlines presented by Eaton (1987) compare well with those shown for the free surface of a flow around a cylinder by Perry, Chong and Lim (1982). They also show a striking similarity to those measured by Perry and Steiner (1987) in the (three-dimensional) turbulent wake behind a flat plate; see figure 1.3. This kind of similarity between three different results lends weight to the argument that one vortex shedding mechanism exists for all nominally two-dimensional bluff bodies, over a range of Reynolds numbers.

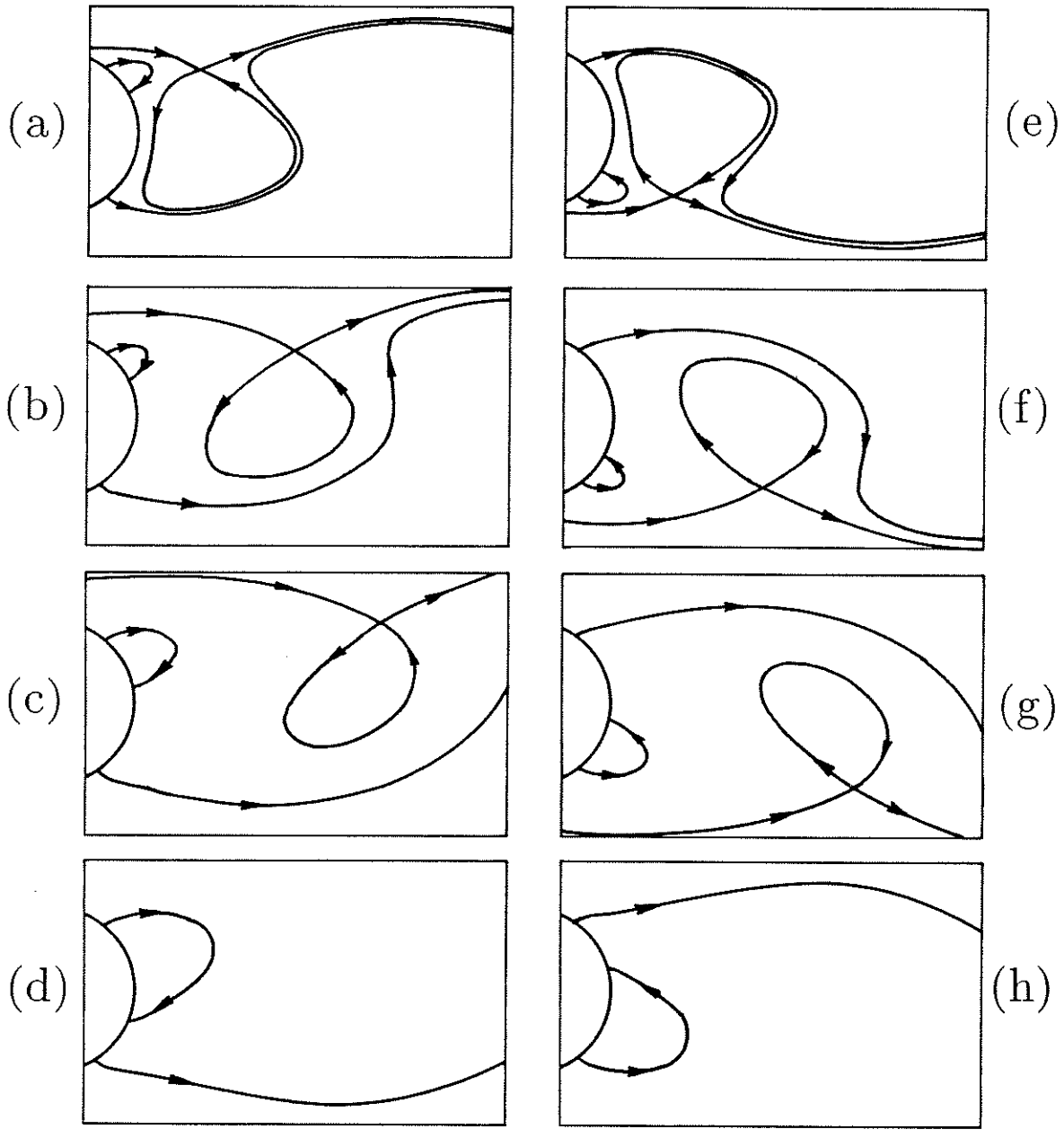

FIGURE 1.1: Separatrix (streamline) pattern showing the vortex shedding cycle behind a circular cylinder (one-eighth period phases). After Eaton (1987).

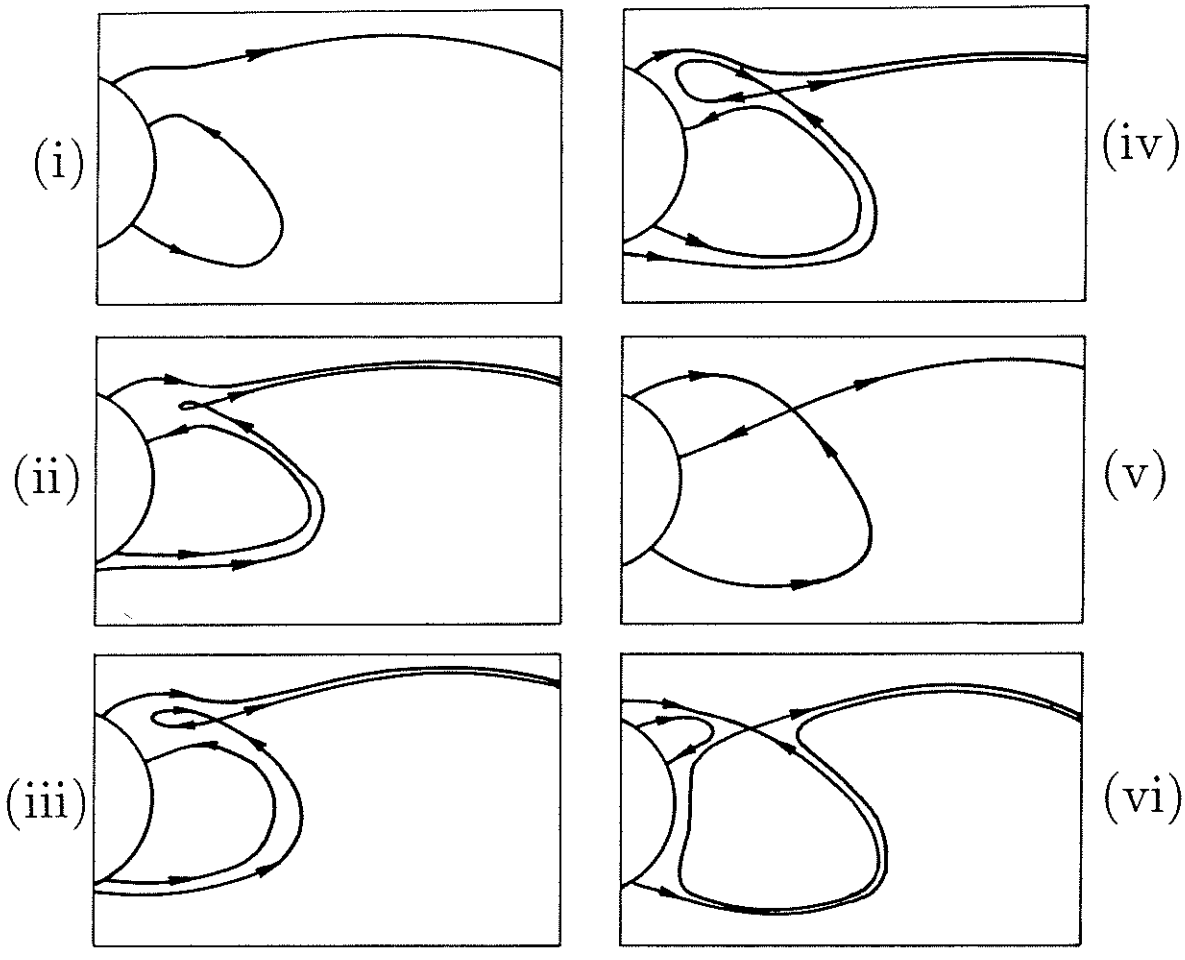

FIGURE 1.2: Showing in detail the process connecting frames H & A of fig. 1.1. After Eaton (1987).

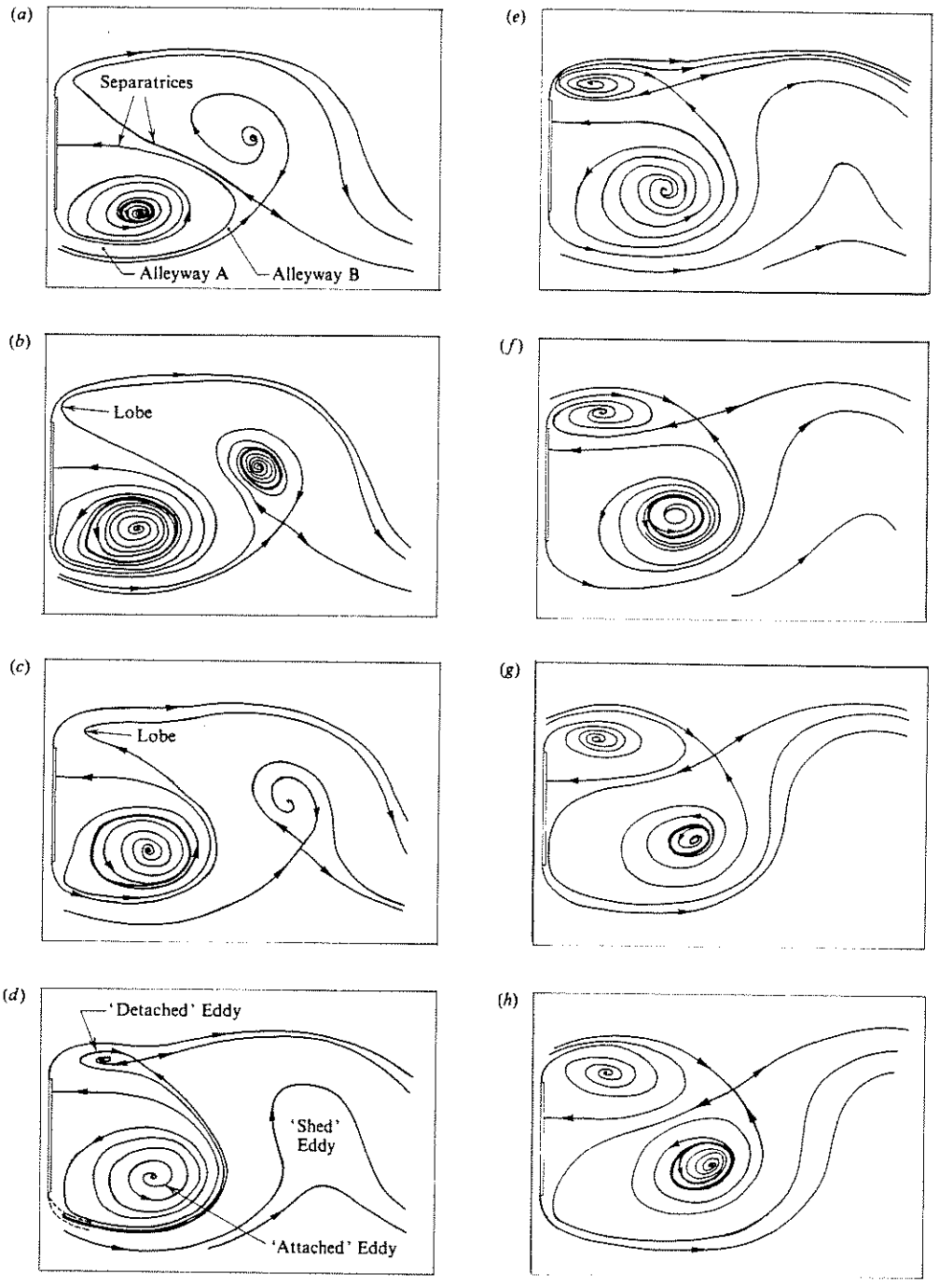

FIGURE 1.3: Eight phases of the vortex shedding process behind a flat plate. After Perry & Steiner (1987). $\mathrm{Re} = 2 \times 10^4$.

Streaklines Due to the greater ease with which streaklines of unsteady flows can be observed, most of the flow visualization results presented in the literature for bluff-body flows have been of streaklines. In most of these cases, the emphasis has been on the wake flow, rather than on the detail of what occurs close to the cylinder where the processes which dominate the forces on the cylinder occur. Streaklines show the locus of fluid particles which have passed through points fixed in the flow; usually some kind of marker that travels with the fluid (e.g. dye or hydrogen bubbles) is injected into the flow to be carried with it. Because vorticity also has the property in incompressible flows that it travels with the fluid (Helmholtz's theorem), streaklines which originate at points of high vorticity indicate[3] the distribution of vorticity in the flow.

Perry, Chong and Lim (1982) presented colour photographs of the streaklines originating from the upstream faces of a circular cylinder in a steady flow at $\mathrm{Re} = 80$. The use of red and blue dyes on the opposite sides of the cylinder provided clear indication of where the vorticity of opposite signs resided in the flow. Incidentally, the apparently planar array formed by the streaklines indicates that the vortex shedding process and wake flow is quite two-dimensional at this Reynolds number, something that does not appear to be true at higher Reynolds numbers (Hama 1957, Gerrard 1978, Williamson 1988 a, 1988 b, 1989). Close-ups of the region just downstream of the cylinder show that during each cycle of vortex shedding, unmarked fluid which originates outside the separation points is pumped into the "cavity" region behind the cylinder: the small amount entrained each time is shed some cycles later in the core of the vortices which separate and move downstream. This pumping action produces an intricate folding of the dye-bearing material lines in the cavity region which become difficult to resolve after more than a few vortex shedding cycles, due to diffusion of dye. A schematic diagram of this folding process is shown in figure 1.4. The computer-aided flow visualization of Eaton (1987) shows in detail the progress of material lines from cycle to cycle: the agreement with the process described by Perry, Chong and Lim (1982) is good. It is in this region of folding that the "attached vortices" shown by the streamline plots of figures 1.1 and 1.2 form. No recognizable vortex is shown by the material lines in the region closest to the cylinder, however the presence could be deduced from the large

[3]Due to the different diffusion rates of dye and vorticity, the correspondence is not always exact, especially for low Reynolds number flows. This is well illustrated by the results of Cimbala, Nagib & Roshko (1988).

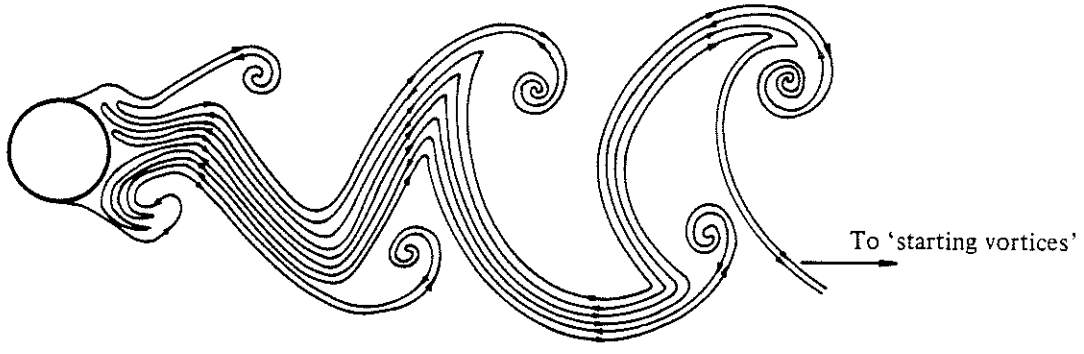

FIGURE 1.4: Diagram of the folding process for the streaklines in the vortex formation region and at the start of the wake. After Perry, Chong & Lim (1982).

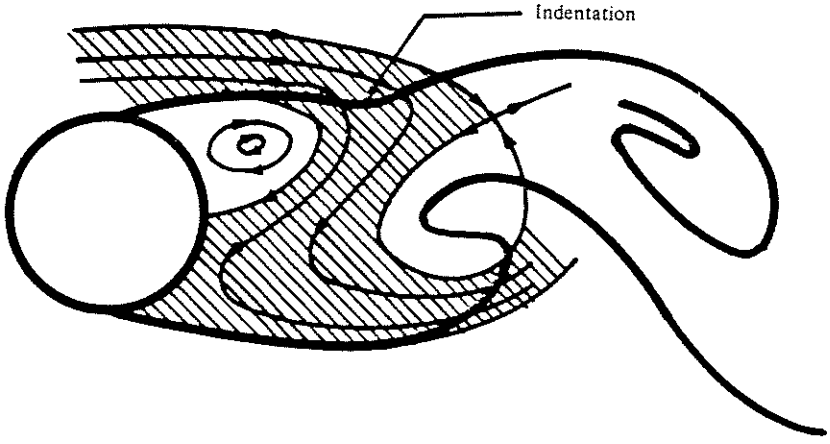

FIGURE 1.5: Interpretation given by Perry, Chong & Lim (1982) to a simultaneous photograph of streak & streamlines. Cross-hatching indicates an "instantaneous alleyway" formed between the top surface of the cylinder and the free separatrix above it.

amount of vorticity associated with the closely folded lines. These vortices closest to the cylinder produce the localized regions of low pressure nearest to the cylinder and hence are responsible for a large proportion of the fluctuating forces on the cylinder.

The fact that the eddy formation region is difficult to visualize using streaklines shows by contrast the importance of the instantaneous streamline pictures discussed above. The relationship between the two types of line is complex in unsteady flows: figure 1.5 shows the interpretation given by Perry, Chong and Lim to a simultaneous photograph of streak and streamlines.

Far downstream from the cylinder, when the wake structure becomes stable, the streamline and streakline patterns will be almost the same for an observer travelling at the speed of the vortices.

Pressure Field Visualization of the pressure field of the flow around a circular cylinder is uncommon, despite the close correspondence between the pressure field and the forces on the cylinder. Nakagawa (1986) produced interferograms of the unsteady pressure field for a Reynolds number of 1.4×10^5. His results clearly show that at this Reynolds number at least, vortices initially form directly downstream of the separation points, in agreement with the instantaneous streamline sketches of figures 1.1 and 1.2.

A point to note in passing is that there need not be any direct correspondence between the magnitude of the pressure fluctuations and the size of "vortices" in the near-wake, since the flow is unsteady. This implies that it may be difficult to identify regions of low pressure in the near-wake merely by inspection of streakline or streamline patterns.

1.3 Reynolds Number Transitions

The description of the vortex shedding process given above was based mainly on work carried out at low Reynolds numbers, but as discussed, it seems that the vortex shedding process is basically similar for a wide range of bluff shapes, and over a wide range of Reynolds numbers. Some qualification to this statement is needed because of the many transitions undergone by the process as the Reynolds number changes. Once the vortex shedding process is established, at Reynolds number below 100, the transitions which occur result from instabilities in the shear flows of the attached and separated boundary layers.

The discussion here centres around observations made in smooth flow; the effects of surface roughness and turbulence will be dealt with later. The nomenclature for different flow regimes as Reynolds number rises is that of Roshko (1961): subcritical is followed by critical, supercritical and transcritical regimes.

1.3.1 Subcritical Wake Transitions

The transitions which occur in so-called subcritical flows all take place in the wake downstream of the cylinder. The main defining characteristic of subcritical flows is that the boundary layers remain laminar up to separation. At higher Reynolds numbers, the transitions take place either in the boundary layer while it is still attached to the cylinder, or immediately after separation. For completeness, a brief description of wake transitions in smooth subcritical flow will be given here, although later emphasis will be on high Reynolds number flows.

From the onset of recognizable vortex shedding at $Re \approx 70$ to $Re \approx 150$, the vortex street wake is entirely laminar and periodic, as reported by Roshko (1953). The frequency of oscillation of the wake is described in dimensionless terms by the Strouhal number $St = fD/U$. Due to diffusion of vorticity, the vortex street gradually disappears downstream of the cylinder, until at a few hundred diameters downstream, no periodicity can be observed (Cimbala, Nagib & Roshko 1988). In fully two-dimensional flow, the shed vortices lie parallel to the cylinder when viewed from above the street, but slantwise shedding, where the vortices are regular and parallel to one another but lie oblique to the cylinder, can also occur. Williamson (1988 a, 1989) showed that this effect can be controlled by adjusting conditions at the cylinder ends, and he proposed it as the explanation for a discontinuity observed in the Strouhal/Reynolds number relationship by Tritton (1959) at Reynolds numbers near 70.

At $Re > 150$, the wake becomes irregular downstream of the vortex formation region as a result of three-dimensional disturbances. Roshko (1953) found that the disturbances are characterized by the appearance of irregular bursts of velocity in the wake, becoming more frequent as the Reynolds number is increased. Similar events are shown in the hotwire traces presented by Tritton (1988, fig. 3.10). Williamson (1988 b) showed that there are two three-dimensional transitions to irregular and eventually turbulent flow in the wake, one at Reynolds numbers near 170, the other near $Re = 230$. Both are associated with production and stretching of streamwise vorticity in the regions between the primary or Strouhal vortices.

At higher Reynolds numbers, the transition to turbulence in the wake seems to be associated with shear layer instabilities which are primarily two-dimensional at inception, but become three-dimensional in the vortex formation region. At Reynolds numbers above 1×10^3, Bloor (1964) found that hotwire traces from the shear layers showed rapid oscillations superimposed on those at the primary vortex shedding frequency. These transition waves, as she called them, have become accepted as signs of Tollmien-Schlichting instability in the shear layers. Flow visualization results of Gerrard (1978) indicate that the transition waves may be evident at lower Reynolds numbers, down to $Re = 500$. His results show that at $Re \approx 1 \times 10^3$, the transition waves have progressed to become recognizable as Kelvin-Helmholtz vortices, of higher frequency than the vortex street, visible in the separated shear layers before primary vortex roll-up.

More recent results such as those of Wei and Smith (1986) and Kourta et al. (1987) also show these "secondary vortices", with frequencies initially comparable to the Strouhal frequency at $Re = 1.2 \times 10^3$, increasing to about 20 times the Strouhal frequency at $Re = 1.6 \times 10^4$. Wei and Smith concentrated on the three-dimensional aspects of the secondary vortices, showing with flow visualization that the secondary vortices, initially evident with a spanwise orientation, undergo three-dimensional instability in the stretching of the shear layers induced by vortex roll-up to produce pairs of counter-rotating streamwise vortices superimposed on the primary Strouhal vortices. They speculated that the additional mixing of fluid inside and outside the wake produced by these vortices contributes to the transition to turbulence in the wake.

The degree to which the secondary vortices interact with the Strouhal vortices has been the subject of debate. At the lower end of the Reynolds number range in which they are observed ($1 \times 10^3 < Re < 2 \times 10^3$), the frequency of secondary vortices is comparable with that of the Strouhal vortices. Over the same range of Reynolds numbers, flow visualizations and base pressure measurements made by Unal and Rockwell (1988) show that the main vortices form much further downstream than they do at Reynolds numbers above and below this range (see fig. 1.6). Consequently, the base pressure in this range rises, and it may be expected that the fluctuating forces which act on the cylinder drop. The drop in base pressure and rise in forces which occur as Re increases above the range is a result of vortex formation again moving closer to the rear of the cylinder. In Unal and Rockwell's flow visualization, the upstream movement of vortex formation was accompanied by the appearance of clearly visible secondary instabilities in the shear layers.

As the Reynolds number rises, the ratio between the frequencies of the secondary and Strouhal vortices increases, and the relative scale of the secondary vortices drops. As this occurs in the Reynolds number range 2×10^3 to 1.6×10^4, Kourta et al. found that the distance downstream from the cylinder at which roll-up of the Strouhal vortices was seen to occur decreased, in agreement with the findings of Unal and Rockwell.

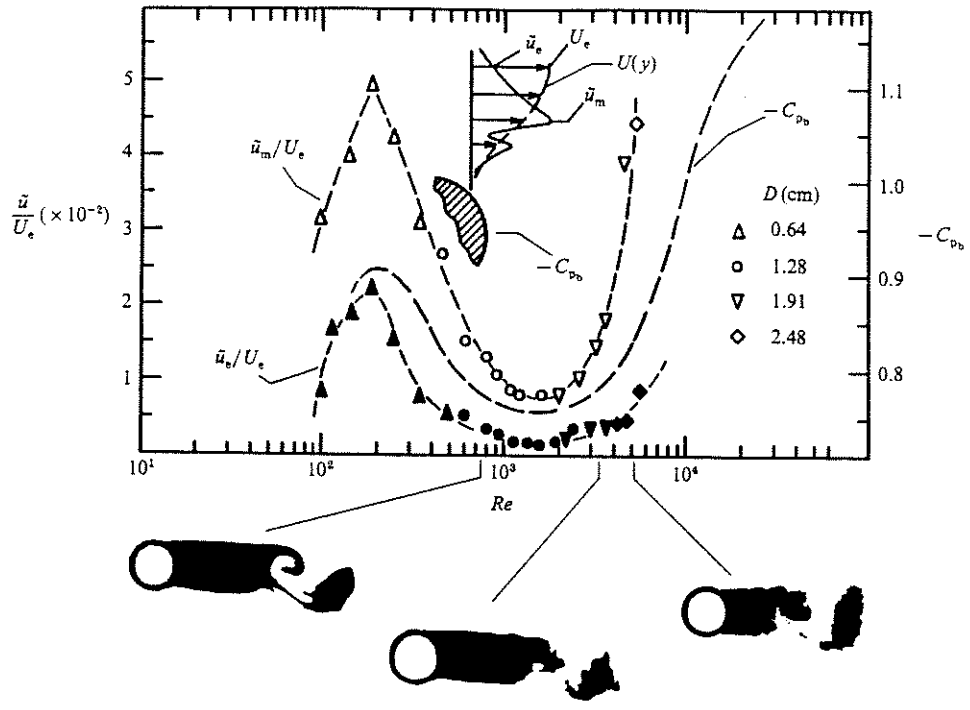

FIGURE 1.6: Variation of base pressure and fluctuating shear layer velocities with Reynolds number, from Unal & Rockwell (1988). Velocity fluctuations at edge ($\tilde{u}_e/U_e$) and at maximum amplitude location within shear layer ($\tilde{u}_m/U_e$). Also shown are visualizations of the near-wake structure from dye injections into wake region. Base pressure line is from Roshko & Fiszdon (1969).

Kourta et al. reported that at Reynolds numbers above 1.6×10^4 the spectra of shear layer velocities exhibited no recognizable frequency peak which could be associated with secondary vortices; the only peaks found were at the Strouhal frequency and its harmonics, superimposed on a smooth distribution attributed to random small-scale motions. Correspondingly it may be assumed that the shear layers progress to fine-scale turbulence shortly after their separation from the cylinder and before their roll-up into primary vortices at these and higher Reynolds numbers. It is found however that the Strouhal vortices which form from them, while turbulent to an extent, still exhibit a strongly dominant frequency, and on average are well organized. All the force coefficients reach a maximum in the upper subcritical range of Reynolds numbers ($1.6 \times 10^4 < Re < 2 \times 10^5$). Probability densities of wake velocities and forces exerted on the cylinder in this regime show a near-Gaussian distribution (Schewe 1983), indicating that the vortex shedding is narrow-band random, rather than periodic.

The next transition which occurs has a very dramatic effect on the vortex shedding process in smooth flow, and occurs when the transition to turbulence in the separating boundary layers takes place very close to separation.

1.3.2 The Critical Regime

In a narrow range of Reynolds numbers ($3 \times 10^5 < Re < 4 \times 10^5$ in smooth flow), an abrupt change occurs in the flow around the cylinder: as Re increases through this range the mean drag force drops, mean lift forces may appear, the magnitude of the fluctuating forces drop, and the frequency of vortex shedding roughly doubles. As a result of these changes, this has come to be called the critical transition.

It needs to be pointed out that the details of the transition behaviour are sensitive to disturbances in the forms of variations in cylinder surface roughness, free-stream turbulence, Mach number, blockage and end-effects. This is true for all Reynolds number transitions in the flow around a circular cylinder, but partly because of the large changes in the forces on the cylinder, it is the effect of disturbances on this transition which have received the most attention. In particular increasing surface roughness and turbulence can reduce the Reynolds numbers at which transition begins, although the effects are not the same as a step increase in Re. It has been observed that the Reynolds number at which transition to the critical regime begins in turbulent flows can be correlated in terms of the Taylor parameter $Ta = I_u(L_u^x/D)^{-1/5}$. On the basis of the Reynolds number at which the mean coefficient of drag first drops to 0.8, Kiya et al. (1982) produced the correlation

$$Re_{\text{crit}}^{1.34} Ta = 1.98 \times 10^5 \, . \tag{1.1}$$

The origin of the changes is in the behaviour of the shear layers, close to the separation points. For a wide range of Reynolds numbers below critical, separation occurs near 80° downstream of the front generator of the cylinder. The boundary layers are laminar at separation, but soon undergo transition to turbulence when the Reynolds number is close to the end of the sub-critical regime. In their turbulent state, the shear layers are able to entrain external fluid more rapidly than before, and it is thought to be due to this that they are then able to become reattached to the surface of the cylinder, subsequently separating again further downstream. An explanation, according to Tani (1964), is that the slow backflow in the separated region of the wake just downstream of separation is unable to supply fluid at a sufficient rate to satisfy the entrainment of the shear layers, which consume the available fluid and then re-attach to the cylinder. The occurrence of this laminar-turbulent separation bubble influences the whole flow around the cylinder, and the final separation can take place as far as 140° degrees from the front of the cylinder (Farell & Blessmann 1983). The progressive appearance of separation bubbles, first on one and then on both sides of the cylinder, accounts for the critical transition. The progression of boundary layer separation through the sub-, super- and transcritical regimes is well illustrated by figure 1.7, taken from Basu (1982).

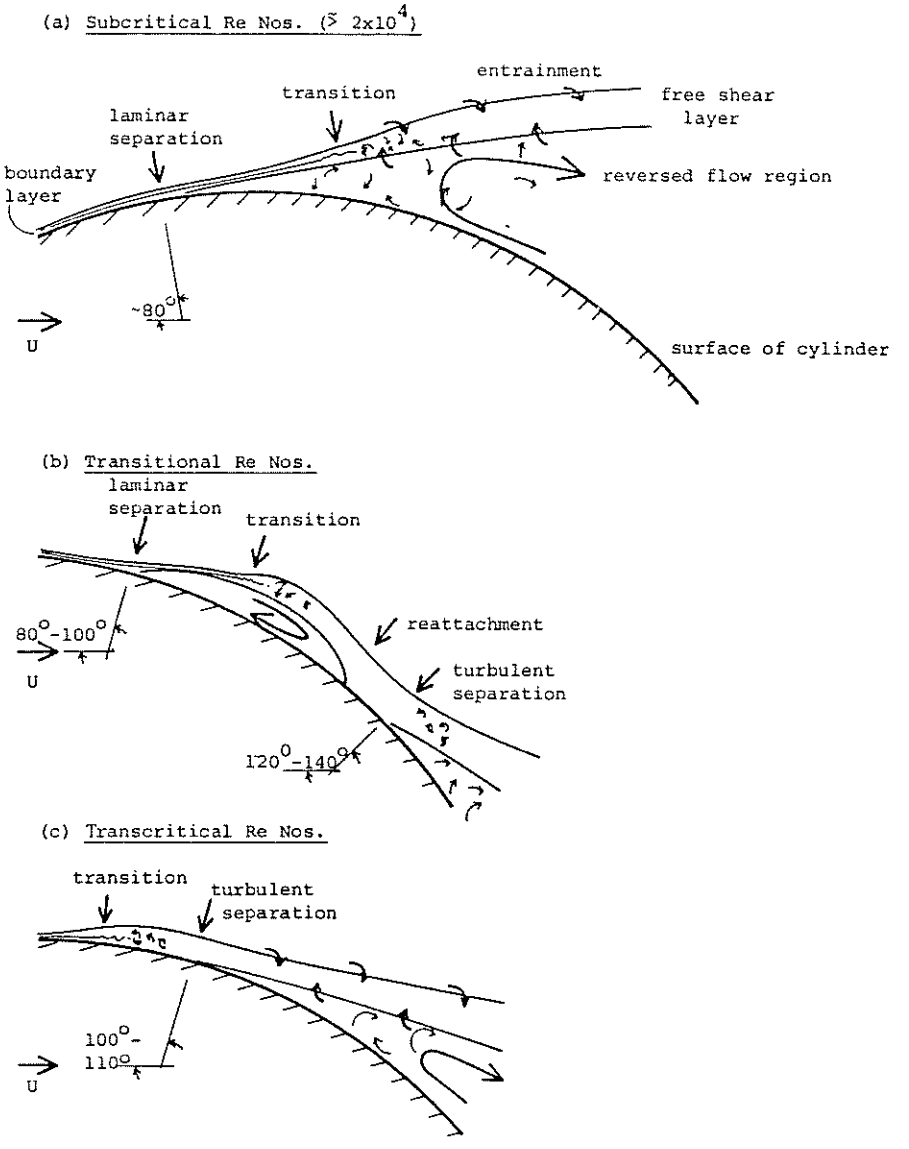

FIGURE 1.7: Schematic diagram of boundary layer separation in the sub-, super-, and transcritical regimes (after Basu 1982).

The main experimental results covering the transition have been published by Bearman (1968 a, 1969 a), Achenbach and Heinecke (1981), Schewe (1983), and Farell and Blessmann (1983).

Bearman made observations of the mean pressure distribution around and along a 12:1 aspect ratio cylinder through the critical transition, also studying the wake velocity spectra. The turbulence intensity was 0.2%, with a tunnel blockage of 6.5%. He found a sharp change in the Strouhal number between Reynolds numbers of 3×10^5 and 4×10^5, with a discontinuity in the transition occurring at $Re \approx 3.4 \times 10^5$. Over this transition range the Strouhal number rose from around 0.2 to 0.46, with the value at the discontinuity being 0.32. Corresponding to this, the pressure drag coefficient, C_d, dropped from 1.14 to 0.23, with an intermediate plateau of 0.45. From observations of the pressure distributions, he concluded that at the high end of this Reynolds number range two separation bubbles existed, while in the transition discontinuity there was one, stretching the whole span of the cylinder. The single bubble produced asymmetry in the pressure distribution, resulting in a *mean* coefficient of lift of 1.3. The fact that the single separation bubble was found to recur on the same side of the cylinder during successive trials left open the possibility that it was peculiar to Bearman's experimental equipment, but Achenbach and Heinecke's later (1981) work showed similar variation in wake Strouhal numbers.

The investigation of Schewe (1983) covered measurements of mean and fluctuating forces acting on a cylinder of 10:1 aspect ratio over the Reynolds number range $2.3 \times 10^4 < Re < 7.1 \times 10^6$. The nominally smooth flow had a turbulence intensity $I_u = 0.4\%$, while the blockage was 10%. Schewe's measurements of the critical transition confirm Bearman's observations, although the numerical values are slightly different, partly due to the fact that Bearman, unlike Schewe, applied a blockage correction to his results. Figure 1.8 shows Schewe's measurements of RMS coefficient of lift, Strouhal number, and coefficient of drag. Reynolds number ranges for the sub-, super- and transcritical regimes are indicated on the figure.

In the asymmetrical, single bubble state, Schewe also found a mean coefficient of lift of 1.3, while spectra of lift and drag had the same dominant frequency, indicating that vortices shed from one side of the cylinder dominated the fluctuating forces. A simplified sketch of the asymmetric flow state provided by Schewe is presented as figure 1.9.

It was found that the asymmetric state was bi-stable, in that once established it remained as long as the Reynolds number was kept constant, and that, in contrast to Bearman's experiment, it showed no preference for one orientation or the other, changing sides at random from one run to the next. In a later paper, Schewe (1986) demonstrated that this orientation could be selected by introducing a small perturbation of the boundary layer on either side of the cylinder. A slight hysteresis effect was found by Schewe in the critical transition range, so that the Reynolds numbers at which the changes between the subcritical, single-bubble and two-bubble states took place varied depending on whether the Reynolds number was being increased or decreased.

Typical spectra of lift forces found by Schewe in the various Reynolds number ranges are presented in figure 1.10. The spectra have been normalized so that with reduced frequency $f_r = fD/U$ on the abscissa scale, the areas under the graphs are the variances of the coefficients of lift force. The spectra will be discussed in more detail below but the

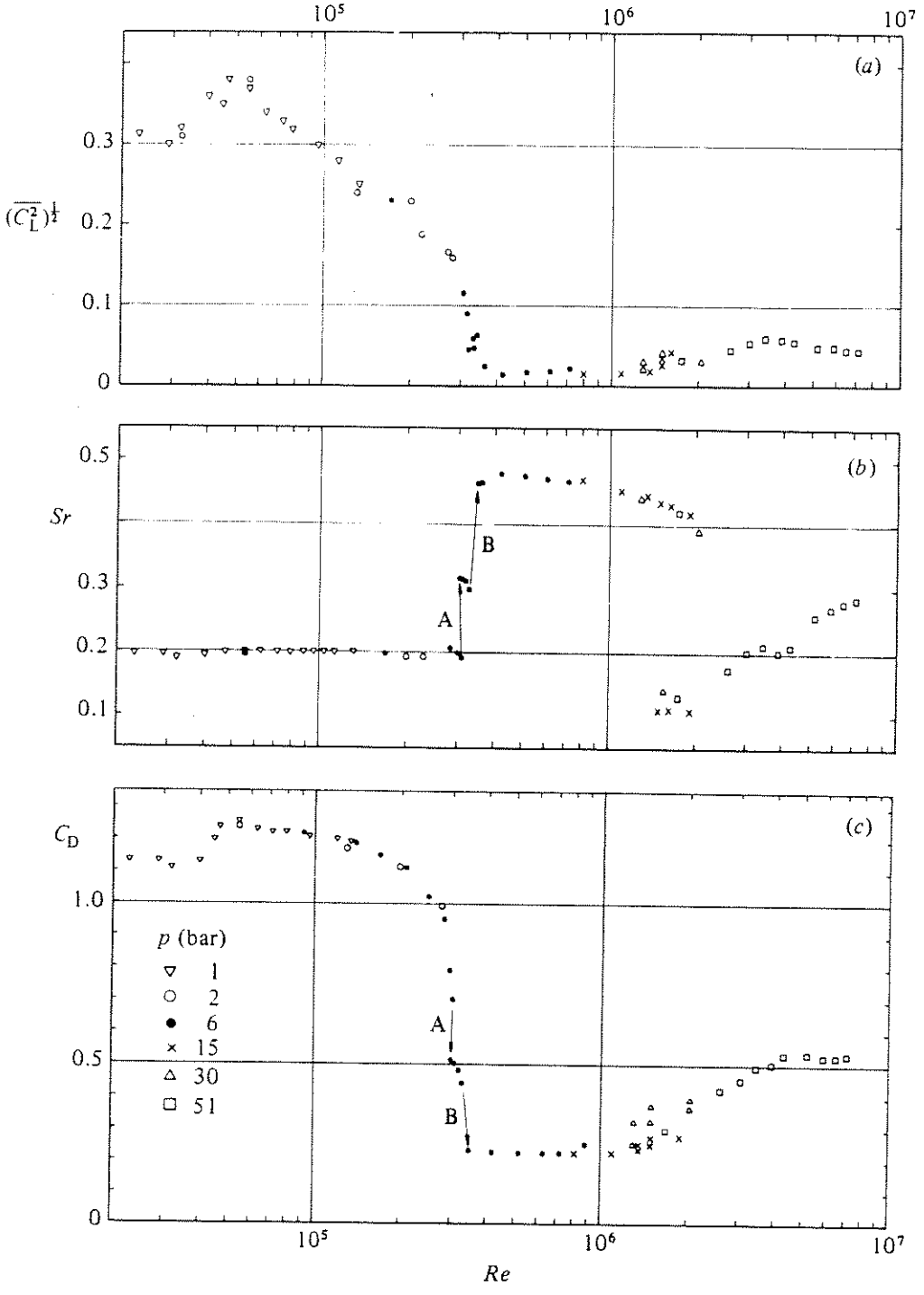

FIGURE 1.8: Measured values of (a) RMS coefficient of lift, (b) Strouhal number of lift forces, (c) mean drag coefficient, from subcritical to transcritical Reynolds numbers. After Schewe (1983).

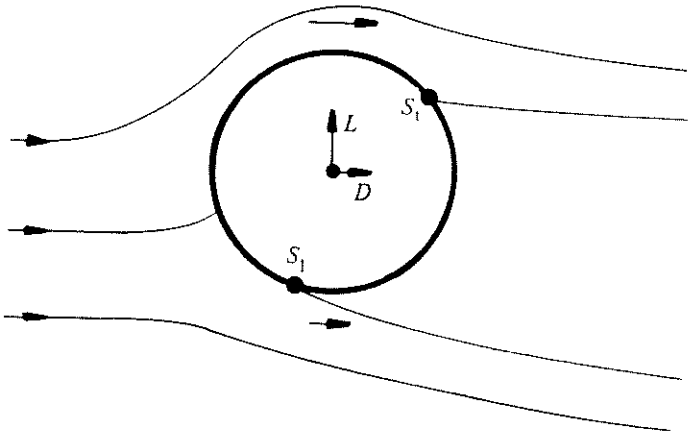

FIGURE 1.9: Simplified sketch of the asymmetric flow state in the critical regime. After Schewe (1983). Simplified sketch of the asymmetric flow state in the critical regime (L = lift, D = drag, S_t = turbulent separation, S_l = laminar separation). After Schewe (1983).

narrow-band nature of the forces in the fully-established (a) subcritical, (b) supercritical (two-bubble), and (f) transcritical regimes is immediately apparent.

The data presented in figure 1.8 indicate that before the critical transition the RMS coefficient of lift and the drag coefficient both decline, while the Strouhal number remains more or less constant near 0.19. This behaviour might be taken to indicate signs of impending transition, but the force spectra in this region with declining coefficients are narrow-banded, indicating that the flow structure is stable. The fine structure of the critical transition is illustrated in figure 1.11.

Very near the step changes in Strouhal number, Schewe found that the onset of transition was indicated by the appearance of broad-band low frequency fluctuations. At the end of the subcritical range, the onset of low-frequency fluctuations coincided with the point in the drag force curve of figure 1.11(c') at which the drag force started to drop. The lift force spectra of figure 1.12 show the low-frequency fluctuations, and again show that vortex-shedding peaks in the various stable states are sharp and distinct.

Mean pressure distributions around a cylinder for the critical regime were published by Farell and Blessmann (1983). Their cylinder had an aspect ratio of 6.14:1, 12% blockage, and the flow had a turbulence intensity $I_u = 0.4\%$. The surface of the cylinder was left in the "as machined" condition. Although they saw asymmetrical distributions in the critical transition, these were unstable, with the flow fluctuating between symmetrical and asymmetrical states for a fixed Reynolds number. What caused the lack of stability of the asymmetric state is unclear; the main differentiating factors from the other investigators were the machined surface of the cylinder and lower aspect ratio. The asymmetrical distributions also displayed a lack of spanwise uniformity, unlike the symmetrical distributions. A sample of the pressure distributions obtained in the critical transition at $Re = 3.4 \times 10^5$ is shown in figure 1.13. Since there was no one stable state, Farell and Blessmann showed three different pressure distributions on the same figure. A point of note is that in the asymmetric state (Sample 1), the most negative pressure coefficients C_p are obtained on the side of the cylinder where final separation occurs furthest towards the base generator of the cylinder, in

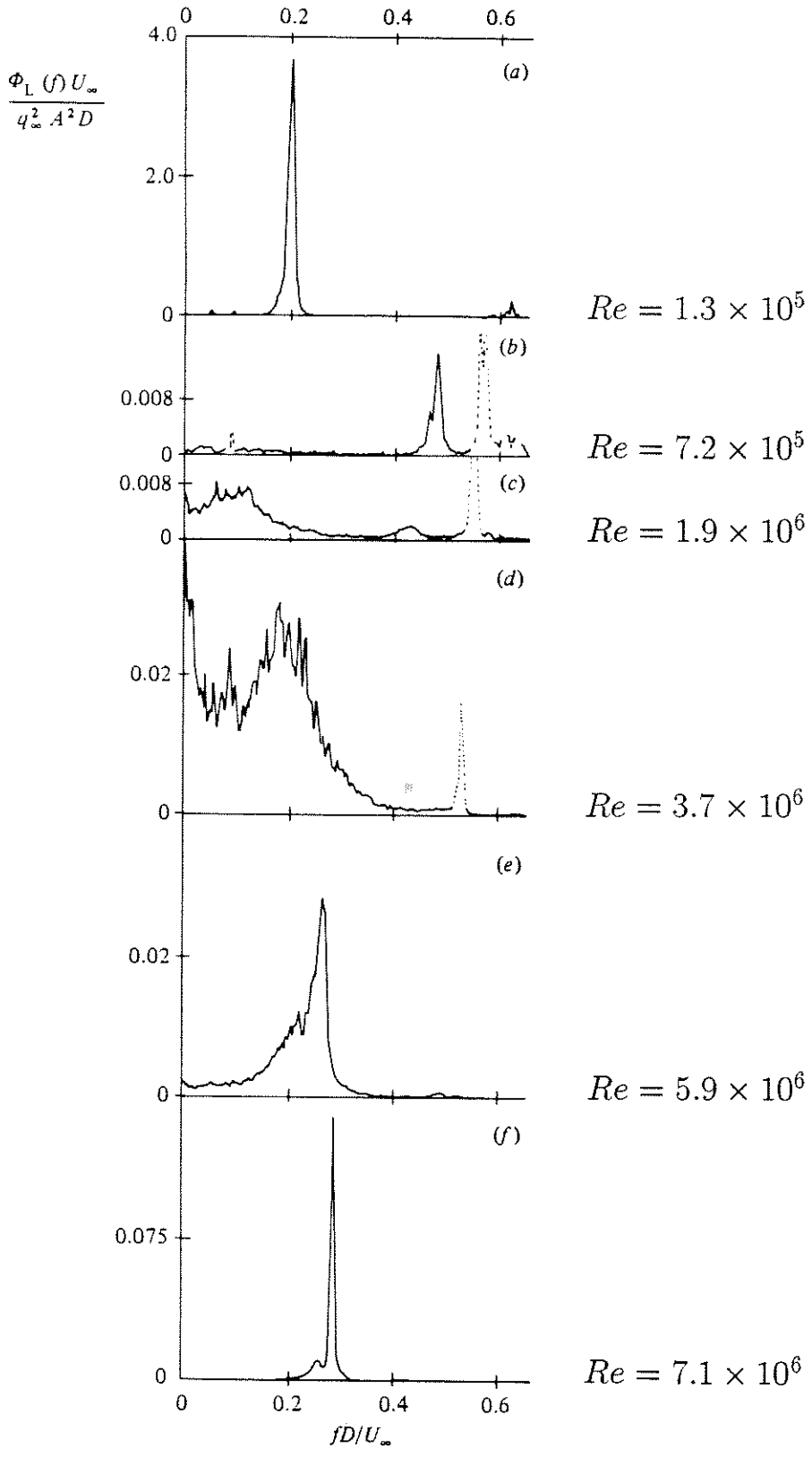

FIGURE 1.10: Power spectra of lift fluctuations measured by Schewe at different values of Reynolds number. Spectra are normalized such that the area under the curve gives the variance of the coefficient of lift. (a); Subcritical. (b); Supercritical. (f); Transcritical. After Schewe (1983).

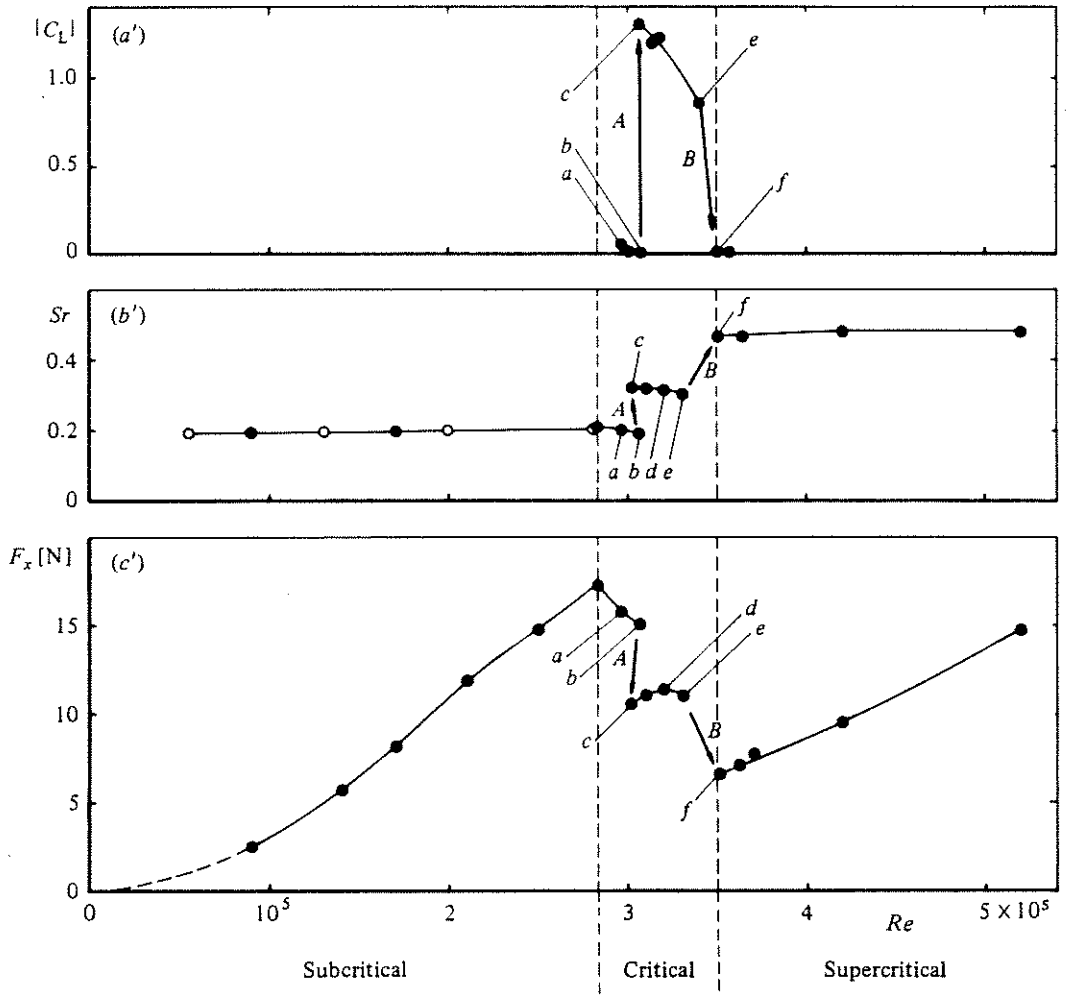

FIGURE 1.11: Fine structure of the critical range found by Schewe. (a') Absolute value of steady lift coefficient $|C_L|$. (b') Strouhal number Sr. (c') Drag force F_x. (Lower-case letters on the figures refer to the spectra of figure 1.12.) After Schewe (1983).

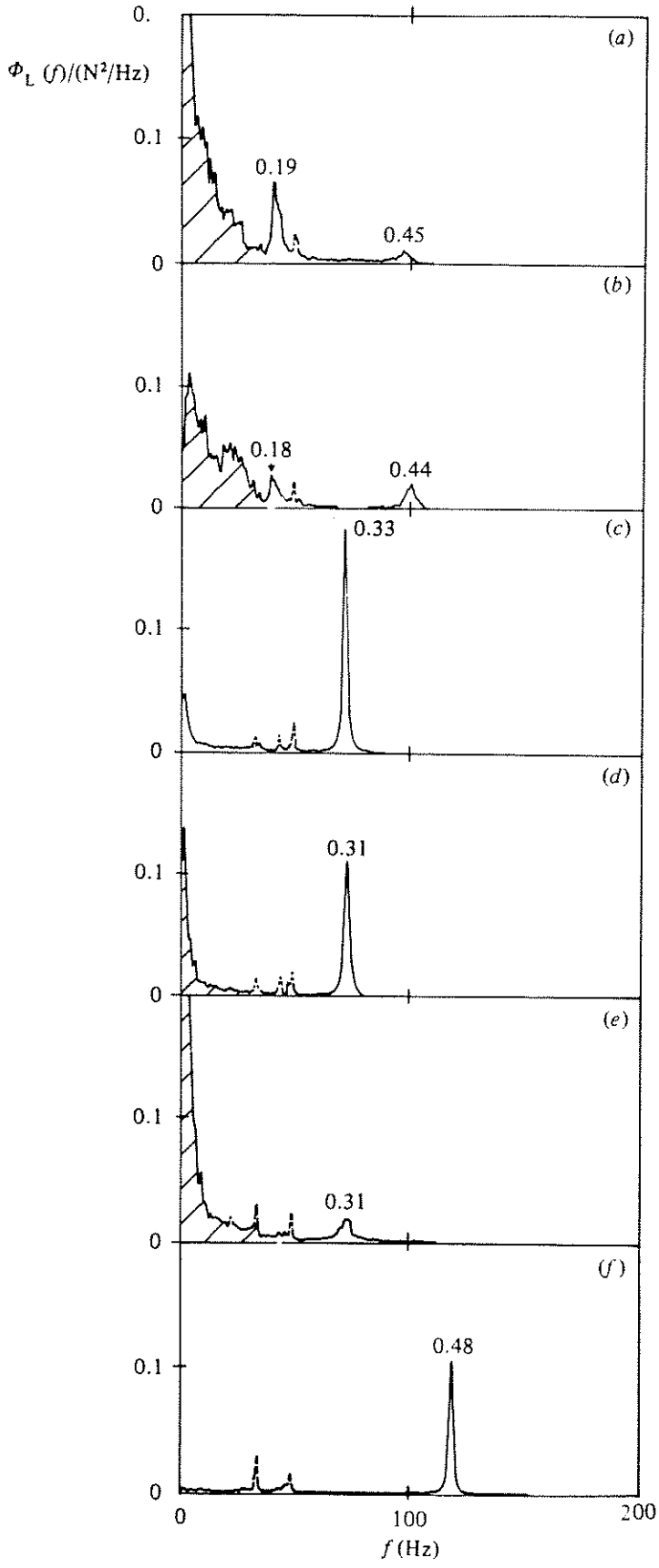

FIGURE 1.12: Spectra of lift forces for the critical transition. (a)–(f) correspond to states in figure 1.11. After Schewe (1983).

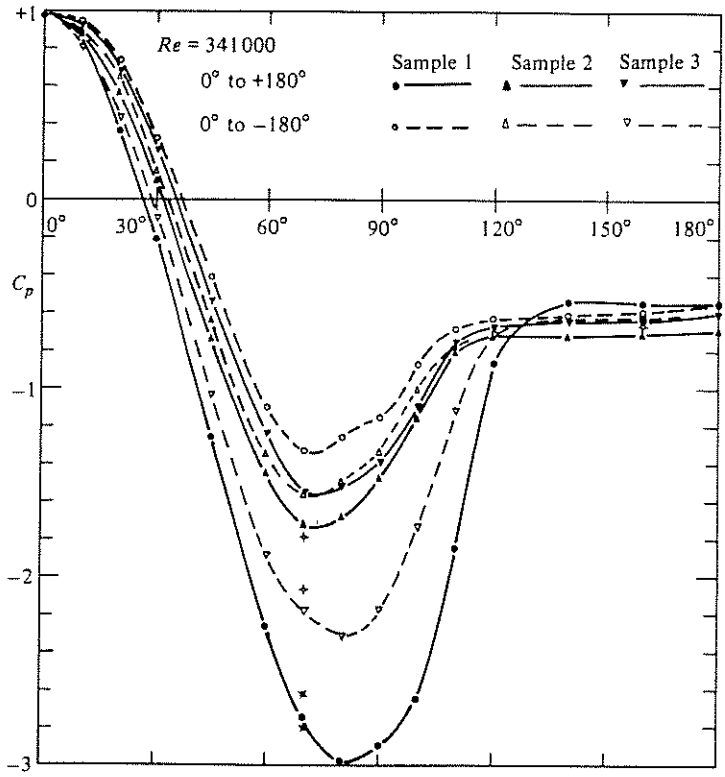

FIGURE 1.13: Pressure coefficient C_p as a function of circumferential angle. Three sample distributions at $Re = 3.4 \times 10^5$. After Farell & Blessmann (1983).

agreement with figure 1.9.

In the work of Bearman (1969 a) and Schewe (1983) it was observed that prior to the critical transition, the magnitude of force and pressure coefficients for the cylinder begin to drop, while the Strouhal number remains relatively constant right up to transition. This is the regime which was called precritical by Zdravkovich (1982, 1990). Zdravkovich maintains that in the precritical state, three-dimensional disturbances in the near wake result in the vortex formation region moving downstream of the cylinder, with reduced spanwise coherence of shedding, but without reduction in wake width. This would produce a drop in force coefficients, with the Strouhal number remaining constant.

Three-dimensional flow phenomena in the critical regime have not been directly discussed above. The three-dimensional behaviour which occurs in subcritical flow seems to be associated with instabilities which appear in the separated shear layers, as described in § 1.3.1. While these effects can lead to lack of spanwise correlation in the unsteady forces which act on the cylinder, flow separation usually occurs along a generator of the cylinder. In the critical regime, additional three-dimensional effects can be associated with the formation of separation bubbles, in which case the angular position of separation may vary along the span, and from one side of the cylinder to the other. The details of the three-dimensional behaviour associated with the critical transition vary slightly from one set of published results to the next, which is not surprising given the well-known sensitivity of the flow in this Reynolds number range.

The "precritical" regime is associated with the gradual drop in C_d which can be

observed in Schewe's results (fig. 1.8) over the range $1\times10^5 < Re < 2.2\times10^5$. According to the results of Higuchi, Kim and Farell (1989), this drop is linked to the intermittent appearance of cell-like structures in the wake, of the order of 1–2 cylinder diameters in spanwise extent. These structures are caused by short separation bubbles, in which the initial separation, reattachment and subsequent separation are probably all laminar. In their experiment, initial separation took place about $\theta = 87°$ from the front of the cylinder, with intermittent reattachment indicated at about $\theta = 92°$. Formation takes place symmetrically on both sides of the cylinder. These short separation bubbles have a less profound effect on vortex shedding and the coefficient of drag than do the longer laminar-turbulent separation bubbles previously described. Measurements of pressure made at $\theta = 65°$ indicate that the formation of the short separation bubbles was associated with a decrease in fluctuations at the Strouhal frequency, and an increase in low-frequency energy. It does not hold that these changes are necessarily reflected in substantial changes in the spectra of overall lift force, and indeed Schewe's results indicate that the spectra of lift force remain sharply peaked near $St = 0.2$ right up to the onset of the critical transition, at $Re = 2.8 \times 10^5$ in his experiment.

Cell-like spanwise structures were also indicated in the results of Humphreys (1960). These cell-like structures, unlike those found by Higuchi, Kim and Farell, are associated with the asymmetric formation of laminar-turbulent separation bubbles and presumably are precursors to the bi-stable single bubble state observed by Schewe and Bearman. The spanwise structure of the cells was visualized using silk threads attached to the leading generator of the cylinder; observations were made over the Reynolds number range $1 \times 10^5 < Re < 3 \times 10^5$. Their spanwise extent was in the range 1.4 to 1.7 diameters. The presence of the threads stabilized the location of the structures and promoted their formation at lower Reynolds numbers.

Silk thread flow visualization was also used by Korotkin (1976), over the Reynolds number range $6.7\times10^4 < Re < 1\times10^6$. He observed cell-like structures in the separation zone over this whole range, in disagreement with the results both of Humphreys and Higuchi, Kim and Farell. The reason for the lack of agreement is unknown, however it is apparent from photographs that Korotkin used many more threads per unit length of cylinder than did Humphreys; these may have interfered with the boundary-layer flow.

1.3.3 Supercritical and Transcritical Regimes

As Reynolds numbers are increased, the supercritical and transcritical flow regimes are observed after the critical transition. For smooth high aspect ratio cylinders in smooth flow, the supercritical regime ($4 \times 10^5 < Re < 1 \times 10^6$) is associated with twin laminar-turbulent separation bubbles. The resulting narrow wake gives high frequency vortex shedding ($St \approx 0.48$) and the mean drag and fluctuating forces are comparatively low. The defining characteristic of the transcritical regime is the presence of turbulent boundary layers with turbulent separation on both sides of the cylinder, at about $\theta = 110°$ from the front of the cylinder (see fig. 1.7). In this regime ($Re > 4 \times 10^6$), the Strouhal number drops to around 0.28 (the figure varies between experiments), accompanied by a rise in mean drag and fluctuating forces, although the coefficients do not reach the levels found in subcritical flow. Comparatively few wind tunnel studies of the flow in these regimes have been carried out despite their significance in engineering

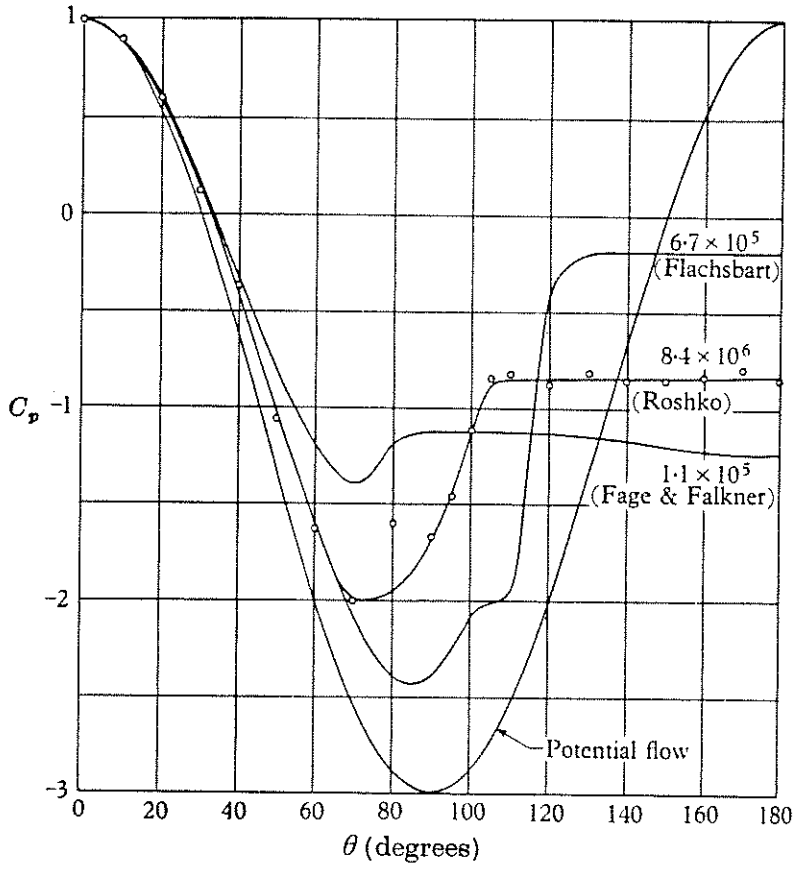

FIGURE 1.14: Mean pressure coefficient distributions in subcritical, critical, supercritical, and transcritical flows. (Roshko 1961.)

applications; the underlying reason is the high cost of such studies.

As discussed above, low turbulence supercritical flow about smooth, high aspect ratio cylinders produces twin laminar-turbulent separation bubbles with final turbulent separation. The mean pressure distribution recorded by Flachsbart (1929) shows the effect of the two separation bubbles, and has final separation taking place at about 130° from the front of the cylinder (see fig. 1.14). Vortex shedding takes place with a well defined frequency, to which the investigations of Delany and Sorensen (1953), Bearman (1969 a), Achenbach and Heinecke (1981) and Schewe (1983) assign a Strouhal number of about 0.48. The measurements of Schewe most clearly define the extent of the supercritical regime and the magnitude and frequency of the forces on the cylinder.

The range of Reynolds numbers between the super and transcritical regimes ($1 \times 10^6 < Re < 4 \times 10^6$) was called the upper critical transition by Roshko (1961) and Schewe (1983). In this range the coefficient of drag rises and the Strouhal number drops. At the end of the transition, the twin laminar separation bubbles no longer appear, and the boundary layer is turbulent at separation. In contrast to the sudden discontinuity in behaviour found at the critical transition, the upper critical transition extends over a larger range of Reynolds numbers and the flow seems to be fundamentally unsteady. Schewe's Strouhal number data (fig. 1.8(b)) show two sets of values here, and his drag coefficients show scatter. In addition, the spectrum of figure 1.10(c), taken at $Re = 1.9 \times 10^6$ shows a very broadly-peaked maximum at $St \approx 0.1$, with

significant low frequency energy. At $Re = 3.7 \times 10^6$, near the end of the upper transition, figure 1.10(d) shows a similar spectrum, but with a greater RMS coefficient of lift and a more distinct maximum near $St = 0.2$. The low-frequency fluctuations indicate that basically asymmetric states may exist over a few vortex shedding cycles, corresponding to intermittent destruction of the twin separation bubbles. This kind of behaviour, with short-time mean lift forces, can be seen in the time-traces presented by Schewe (his fig. 13 (c)) for this regime. In the earlier investigation of Roshko (1961), no vortex shedding maximum was observed in wake velocity spectra taken 7.3 D downstream from the cylinder centreline, over the range of Reynolds numbers 0.9×10^6 to 3.5×10^6. This could be taken to agree with the observations of Schewe (although the measurements are of two different things), when it is considered that the peak of figure 1.10 (c) is very broad, with values at zero frequency, and that Roshko's velocity spectra were recorded downstream of the cylinder. Roshko's coefficient of drag measurements in this range also have the upward trend with Reynolds number found by Schewe.

The highest Reynolds number regime yet found is the transcritical regime ($Re > 4 \times 10^6$). There is good reason to suppose that no further regimes exist, and that all dimensionless coefficients become independent of Reynolds number as it approaches infinity. This is because all the major transitions thus far described have been due to instability phenomena and transitions to turbulence in the wake, shear and boundary layers, and the defining characteristic of the transcritical regime is that the boundary layers undergo transition to turbulence while still attached to the cylinder, and are turbulent at separation. It is expected that when the transcritical regime is fully established, boundary layer transition occurs very close to the upstream stagnation point, so that no change will occur with further increase in Reynolds number.

Few laboratory observations of the transcritical regime in smooth flow with smooth cylinders are available. The ones in which nominally two-dimensional flows were used are those of Roshko (1961, $Re_{\max} = 8.4 \times 10^6$), Jones, Cincotta and Walker (1969, $Re_{\max} = 1.24 \times 10^7$), van Nunen (1974, $Re_{\max} = 7.6 \times 10^5$), James, Paris and Malcolm (1979, $Re_{\max} = 1.09 \times 10^7$), Schewe (1983, $Re_{\max} = 7.1 \times 10^5$). The general indication from these tests is that the flow becomes independent of Reynolds number in the transcritical regime, however different asymptotic values of coefficients were approached in each experiment. For example, the range of reported C_d values at $Re = 5 \times 10^6$ is 0.4 to 0.75. It is likely that the cylinder surface roughness makes an important contribution to this variation, since as boundary layers are turbulent in transcritical flow, increased surface roughness produces greater boundary layer momentum deficits and promotes earlier separation.

1.3.4 Summary

The transitions discussed above have recently been classified according to the mechanism involved by Zdravkovich (1990). These classifications are reproduced here in table 1.3.4 and figure 1.15. His nomenclature differs a little from that used in the discussion above, for example the regimes TrBL4, T1 and T2 together comprise what is referred to in this thesis as the transcritical regime.

As a part of his conception of the flow having a succession of regimes which are

TABLE 1.1: Classification of transition regimes due to Zdravkovich (1990).

Name	Description	Reynolds number range
L1	"creeping" flow—no separation	$0 < Re <$ 4–5
L2	steady separated region—closed near-wake	4–5 $< Re <$ 30–48
L3	periodic laminar wake	30–40 $< Re <$ 150–200
TrW1	transition to laminar vortices in the wake	150–200 $< Re <$ 200-250
TrW2	transition of vortices during formation	200–250 $< Re <$ 350–500
TrSL1	transition waves in free shear layers	350–500 $< Re <$ $1\text{–}2 \times 10^3$
TrSL2	transition vortices in shear layers	$1\text{–}2 \times 10^3 < Re <$ $2\text{–}4 \times 10^4$
TrSL3	fully turbulent shear layers	$2\text{–}4 \times 10^4 < Re <$ $1\text{–}2 \times 10^5$
TrS0	onset of transition on separation	$1\text{–}2 \times 10^5 < Re <$ $3.2\text{–}3.4 \times 10^5$
TrS1	single separation bubble regime	$3.2\text{–}3.4 \times 10^5 < Re <$ $3.8\text{–}4 \times 10^5$
TrS2	two-bubble regime	$3.8\text{–}4 \times 10^5 < Re <$ $5 \times 10^5\text{–}1 \times 10^6$
TrS3	supercritical regime	$5 \times 10^5\text{–}1 \times 10^6 < Re <$ $3.5\text{–}6 \times 10^6$
TrBL4	transcritical regime	$3.5\text{–}6 \times 10^6 < Re <$ $6\text{–}8 \times 10^6$
T1	postcritical regime	$Re > 8 \times 10^6$
T2	ultimate regime	$Re \to \infty$

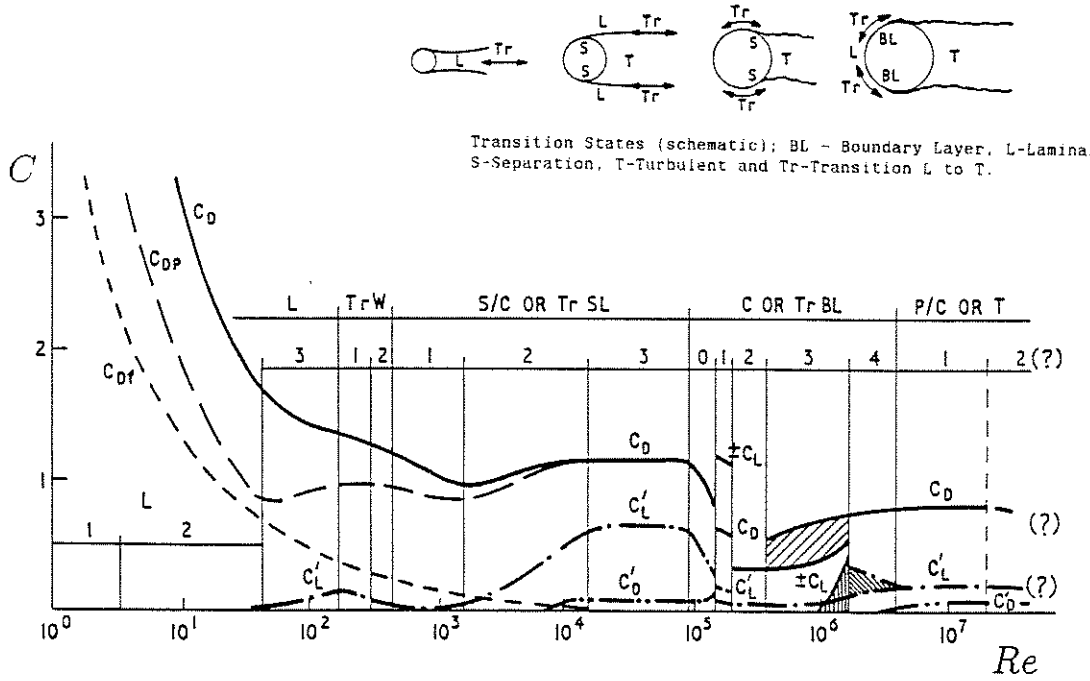

FIGURE 1.15: Force coefficients as functions of Reynolds number; C_D–mean drag, C_{Df}–friction drag, C_{Dp}–pressure drag, C'_D–fluctuating drag, C_L–mean lift, C'_L–fluctuating lift (After Zdravkovich 1990). The figure will appear in the forthcoming book *Flow Around Circular Cylinders*, and the copyright of the figure is retained by M.M. Zdravkovich.

sensitive to Reynolds number and disturbances, Zdravkovich maintains that the various transitions are initiated at a lower Re (or may be obliterated) by disturbances such as free stream turbulence and surface roughness. This is not taken to imply that an increased disturbance level is equivalent to an increase in Re, since the disturbances

themselves become the controlling parameters of the flow. The effect of these disturbances on the flow is discussed below in §§ 1.5.4 and 1.5.5.

1.4 Effect of Cylinder Motion on Vortex Shedding

As discussed in the preceding sections, flows of fluid past rigid circular cylinders typically produce well-developed vortex street wakes with characteristic dimensionless frequencies, now known as Strouhal numbers after the experiments of Strouhal (1878). Strouhal also found that if one of the natural frequencies of the wires used in his experiment fell near the vortex shedding frequency, that frequency could be altered by the vibration of the wire, and that the intensity of the sound produced increased. Rayleigh (1879) showed that in that case, the vibrations of the wires took place in a plane perpendicular to the flow. It is now known (see e.g. King 1977) that it is also possible for comparatively large oscillations ($\sim 0.5\,D$) to arise in a plane parallel to the flow, if the cylinder in question is very lightly damped. For most structures in flows of air, these along-flow (in-line) vibrations due to vortex-structure interaction are unlikely to occur, and so this phenomenon will only be addressed in passing.

While it would be expected that resonance, i.e. coincidence of a vortex shedding frequency with a structural natural frequency, could produce comparatively large vibration amplitudes, the amplitudes which actually arise for lightly damped structures are larger than expected from forced vibration theory. This fact, taken together with the observation that the vortex shedding frequency can be altered to match that of the structure, indicates that vortex-induced vibration is to some extent a non-linear, self-excited type. The degree to which the response changes in kind from forced vibration to self-excited oscillation is influenced by the reduced velocity and the mass-damping parameter K_s. For reduced velocities in the appropriate range ($5 < V_r < 6$), progressively lower values of mass-damping ($K_s < 4$, say) increase the extent to which the response has a self-excited nature.

In studies of the interaction of cylinder oscillation and vortex shedding, two kinds of experimental approach can be adopted: to force the cylinder to oscillate at various fixed amplitudes and frequencies, or to allow a flexibly-mounted cylinder to vibrate freely in the flow. Each method has its advantages and disadvantages: in the first, ease of control of experimental parameters is important, while the chief advantage of the second is that it can correctly simulate full-scale conditions. The linkage between the two has often been assumed (see e.g. Bearman 1984); experiments and computations conducted by Staubli (1983) have strengthened the connection.

In the sections which follow, the observed properties of the interaction of cylinder oscillation and vortex shedding are discussed first, after which the characteristics of the vortex-induced forces which act on oscillating cylinders are dealt with. Finally, since all the available measurements have been made in smooth flows, the possible influence of turbulence on so-called motion induced forces is considered.

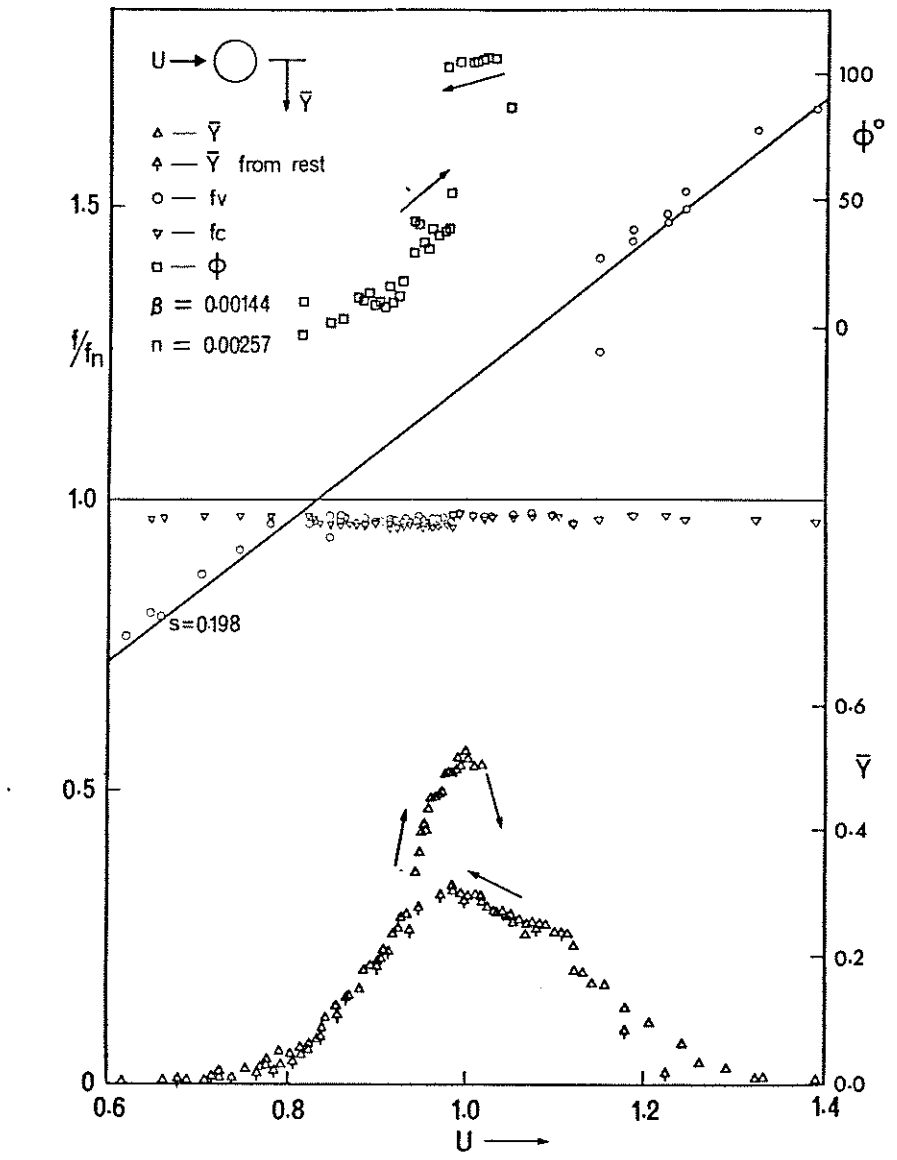

FIGURE 1.16: Results of free vibration experiments using a lightly-damped cylinder in a wind tunnel. Smooth flow, $1 \times 10^4 < Re < 5 \times 10^4$. $\mathrm{U} = U/2\pi f_n D$; f_n = cylinder oscillation frequency "*in vacuo*"; f_v = vortex shedding frequency; f_c = cylinder oscillation frequency; ϕ = phase angle by which pressure measured at cylinder shoulder leads displacement; $K_s = \beta/2n = 0.28$. From Parkinson, Feng & Ferguson (1968).

1.4.1 Frequency Entrainment or Lock-In

When fluid flows past a cylinder of low mass-damping parameter (typically $K_s < 1$ in smooth subcritical flows) and the frequencies of structural vibration and vortex shedding are sufficiently close, it is observed that the frequency of vortex shedding will jump to match the frequency of structural oscillation over some range of reduced velocity. Within this range, the amplitudes of cylinder oscillation can jump to reach some value near one diameter. The results presented by Parkinson, Feng and Ferguson (1968), shown here in figure 1.16, illustrate this general pattern.

The experiments were conducted using a lightly-damped aluminium cylinder in a wind tunnel; $K_s = 0.28$. On the abscissa $\mathsf{U} = U/2\pi f_n D = V_r/2\pi$, while the left-hand ordinate f/f_n shows frequencies normalized by the frequency of the test rig when the cylinder was replaced by a streamlined bar of the same mass and length. The right-hand ordinate shows the phase angle, ϕ, measured between cylinder displacement and suction at a pressure tapping located at the shoulder of the cylinder (90° from the front), and also the normalized motion amplitude $\overline{Y} = y_{\max}/D$. The cylinder frequency f_c is seen to remain relatively constant over the range of U at $f_c \approx 0.97$. The vortex shedding frequency (actually the frequency of pressure fluctuations), f_v, while varying roughly linearly with U over the ends of its range (as expected with a constant Strouhal number $St = 0.198$), is seen to coincide with the cylinder frequency over the range $0.8 < \mathsf{U} < 1.15$. Over this range of lock-in, the amplitude of the cylinder oscillation is seen to rise substantially. Another interesting feature is the evidence of hysteresis effects in both the oscillation amplitude and the phase lead of the surface pressure with respect to cylinder displacement. When the velocity of the flow was slowly increased between on reading and the next, higher oscillation amplitudes of motion were obtained than if the velocity was gradually decreased from above lock-in. One further point of note is that in this free-vibration experiment, lock-in occurred only at reduced velocities *above* that required for coincidence of frequencies (at $\mathsf{U} \approx 0.83$). This corresponds to the case of the cylinder oscillating more slowly than the Strouhal frequency for the stationary cylinder.

For freely vibrating cylinders with *very* low mass-damping parameters, such as for lightly damped cylinders in water, the situation at cross flow lock-in is a little different, in that the cylinder oscillation frequency tends to be "attracted" to the fixed cylinder Strouhal frequency. This can be seen in the results of Angrilli, Di Silvio and Zanardo (1972), shown here in figure 1.17. In their experiment, a light P.V.C. tube was mounted on a sprung yoke and subjected to flow in a water channel. Using an estimated *in vacuo* value for ζ of 0.01, and with the information they supplied concerning cylinder diameter, spring rates and frequencies, $K_s \approx 0.015$. In this situation, where the cylinder can be forced to vibrate at frequencies away from the *in vacuo* natural frequency, it can no longer be assumed that the response amplitude is a function of the mass-damping parameter. That is, the response amplitude may become a function of both ζ and $m/\rho D^2$ separately, rather than their product in K_s.

As mentioned at the start of this section, freely-vibrating cylinders of low K_s (e.g. King 1974, 1977) also exhibit the phenomenon of "in-line" lock-in, which occurs at reduced velocities which are rational submultiples of the reduced velocity for cross flow lock-in ($V_r \approx 2.5 = 5/2$ and $1\frac{2}{3} = 5/3$). These ratios are sometimes found to produce lock-in for forced *cross flow* oscillation, as discussed below, but are not known to be associated with cross flow vibration for freely-vibrating cylinders.

Experiments carried out with cylinders which are forced to oscillate show frequency entrainment behaviour which is slightly different to that which occurs for freely-vibrating cylinders. Only experiments in which the cylinder oscillation was forced in the cross flow direction will be discussed here, since that is most relevant for structures in flows of air (medium to high values of K_s).

Koopman (1967), in wind tunnel experiments conducted at low Reynolds numbers

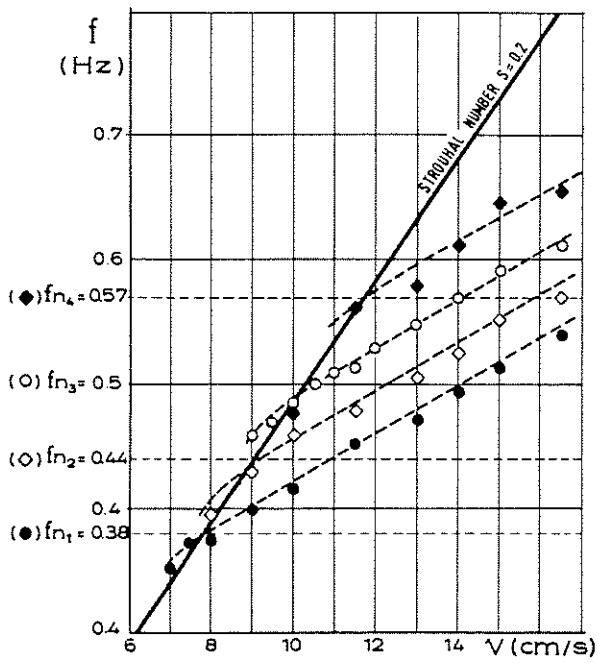

FIGURE 1.17: Results of tests of an elastically-mounted cylinder in a flow of water. Different springs were used to produce four different natural frequencies f_{n_1}–f_{n_4}. V is the flow speed and f the frequency of cylinder oscillation. $2.5 \times 10^3 < Re < 7 \times 10^3$, $K_s \approx 0.015$. From Angrilli, Di Silvio & Zanardo (1972).

($100 < Re < 300$), demonstrated a number of important features of forced oscillation lock-in. The first was that the wake frequency became the same as the cylinder oscillation frequency for frequencies both above and below[4] the fixed cylinder vortex shedding frequency. In addition, the range of frequencies over which lock-in occurred increased with the amplitude of oscillation. Both these features can be seen in figure 1.18, which also illustrates that Koopman found a threshold amplitude for lock-in.

These two features were also observed by Stansby (1976), at higher Reynolds numbers ($3600 < Re < 9200$). In his experiments, Stansby also noted secondary and tertiary lock-in, when the cylinder oscillated at twice and three times the fixed cylinder Strouhal frequency (the evidence for secondary lock-in was much weaker than for tertiary lock-in). His results are shown in diagrammatic form in figure 1.19, replotted to match the format used above in figures 1.16 and 1.17, with reduced velocity on the abscissa.

Stansby also observed the phase of wake velocity fluctuations with respect to cylinder motion, and found a sudden jump of about 180° in the phase relationship in the middle of the lock-in regime, as shown in figure 1.20. A sudden change of phase was observed at similar Reynolds numbers by Bishop and Hassan (1964 b), and is also evident in the free-vibration results of figure 1.16. The jump seems to be related to a change in wake topology, as will be discussed below. The lock-in boundaries observed by Stansby, together with the reduced velocity at which the sudden jump in phase was found, are shown in figure 1.21.

[4]For freely-vibrating cylinders, lock-in tends to occur only when the cylinder oscillation frequency is below that of the fixed-cylinder vortex shedding frequency.

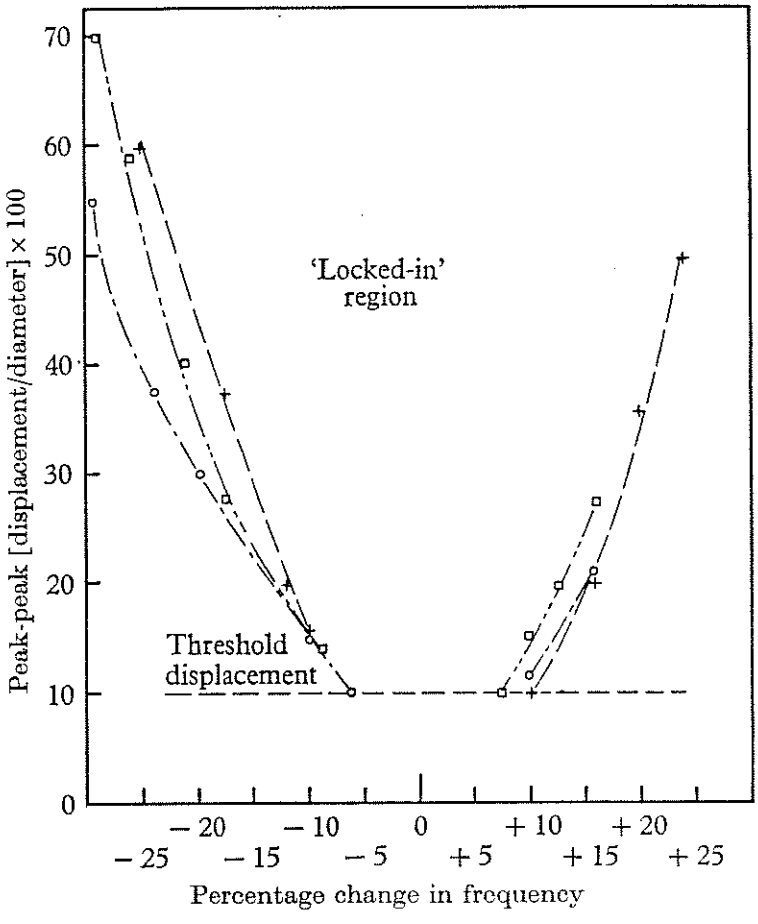

FIGURE 1.18: Lock-in boundaries found by Koopman (1967), $100 < Re < 300$.

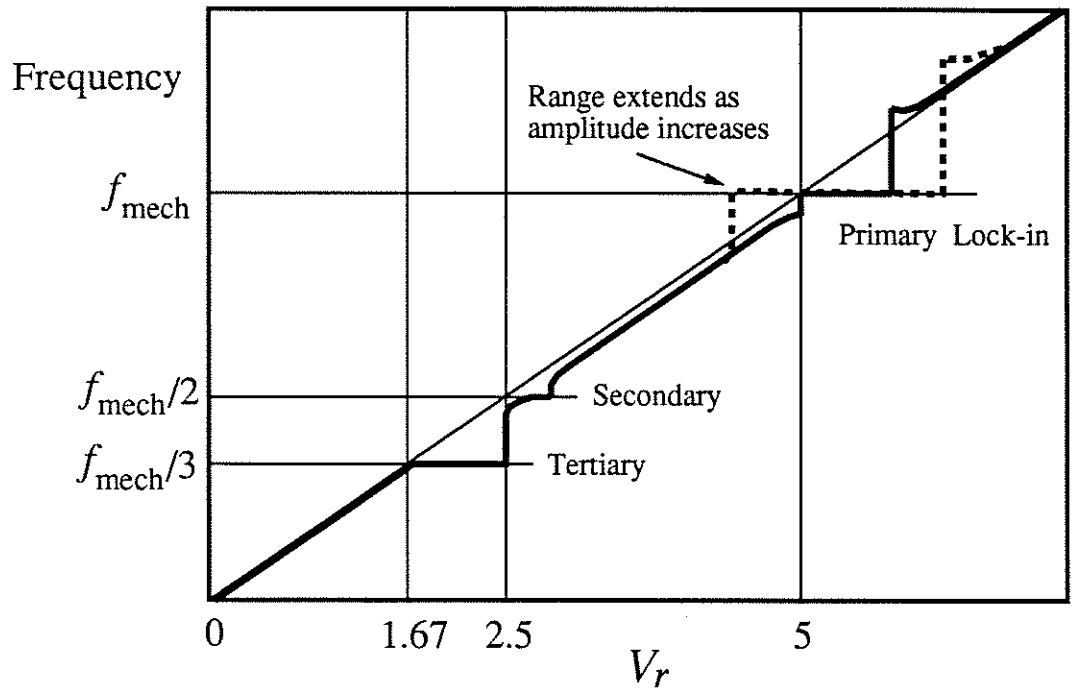

FIGURE 1.19: Diagram illustrating the primary, secondary and tertiary lock-in regimes observed by Stansby (1976).

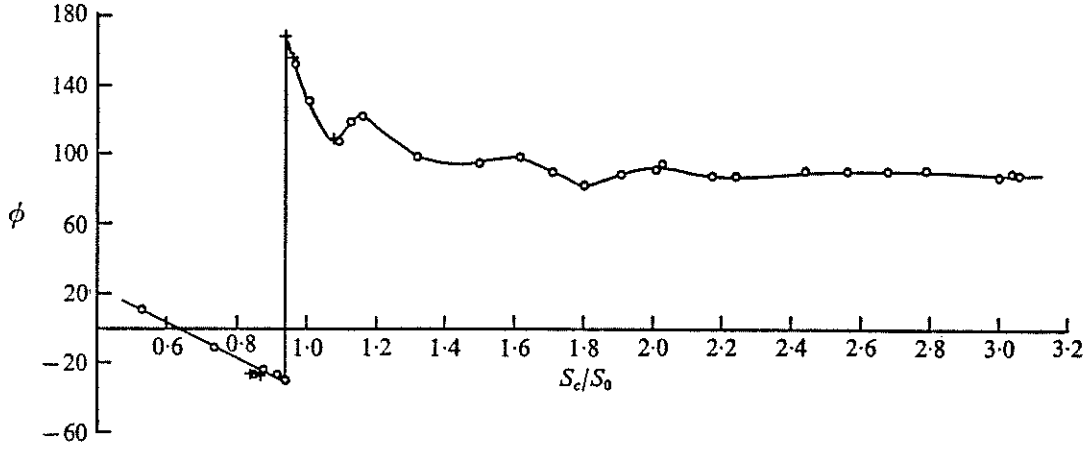

FIGURE 1.20: Variation of phase, ϕ, of hotwire signal with respect to cylinder motion as a function of the ratio of cylinder oscillation frequency to Strouhal frequency S_c/S_0. After Stansby (1976).

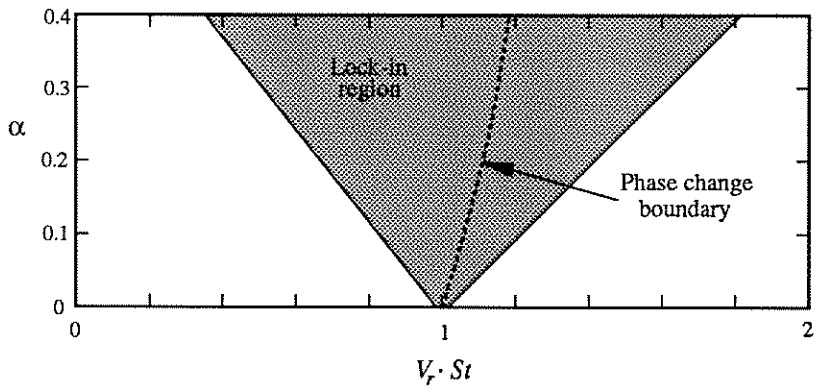

FIGURE 1.21: Lock-in boundaries at $Re = 3600$ together with values of V_r at which a sudden phase change was observed. After Stansby (1976).

Stansby found that the oscillation amplitude required for lock-in to be observed was not fixed, but varied with Reynolds number: for instance, lock-in was not observed at 3% amplitude for $Re = 9200$, but was found at 1% amplitude when $Re = 3600$. Since the range of V_r required for lock-in decreases with amplitude, lock-in becomes increasingly hard to detect at lower amplitudes in any case, due to the limited frequency resolution of most spectral analysis techniques.

Above and below the lock-in boundaries, Stansby's results indicated that the wake frequency was "forced away" from the fixed cylinder Strouhal frequency, in a direction opposite to that of the impending lock-in. This characteristic was also found by Bearman and Davies (1975) for forced oscillation of a D-section cylinder, and also by Woo, Cermak and Peterka (1983) for forced oscillation of a cylinder in a shear flow. The cause of this characteristic is unclear, although the discussion given by Bearman and Davies indicates that the effect may be due to some peculiarity of the spectral analysis. Stansby stated that near the boundaries of lock-in, an oscilloscope trace of a wake hotwire signal showed that the shedding changed intermittently from being locked-in to not being locked-in, while Woo, Cermak and Peterka's flow visualization showed the same behaviour. Wake spectra produced by Bearman and Davies for conditions outside lock-in show spectral peaks at the fixed-cylinder Strouhal frequencies and at the cylinder oscillation frequencies, reflecting the non-stationary nature of the flow.

A final point relevant to the discussion of this section is that experimental results have suggested that cylinder motion can influence the nature of vortex shedding which would otherwise be determined by Reynolds number. Wootton (1968, 1969) carried out a series of tests on freely-vibrating models of chimney stacks in the NPL compresssed-air tunnel (discussed below in relation to K_s–α envelopes). For models with roughened surfaces, he found that the Strouhal numbers remained relatively constant in the range 0.15 to 0.21 over the entire range of Reynolds numbers available in his experiment ($8 \times 10^4 < Re < 2.1 \times 10^6$). By contrast, no definite Strouhal numbers could be inferred in the supercritical range of Reynolds numbers ($4 \times 10^5 < Re < 1.5 \times 10^6$) for models with smooth surfaces, except in the few cases discussed below. Presumably, free end effects disturbed formation of the twin laminar-turbulent separation bubbles which

normally accompany high frequency vortex shedding for smooth circular cylinders of high aspect ratio in the supercritical range. For smooth models with low mass-damping, response peaks were noticed at reduced velocities near 5 in this supercritical range of Reynolds number ($Re \approx 8 \times 10^5$), implying that vortex shedding was re-established with a Strouhal number near 0.2. The response amplitudes which accompanied this return to "normal" vortex shedding were of the order 0.1 D.

1.4.2 Spanwise Correlation of Vortices

A feature of vortex shedding from stationary cylinders at most Reynolds numbers is that the vortices display a limited spanwise organization, with phases and strengths of the vortices varying from point to point along the span of the cylinder. During lock-in, vortices tend to be shed in phase along the span, a point well illustrated by Koopman's flow visualization[5].

Quantitative measures of the degree of spanwise organization are given by the correlation coefficients of the wake velocities or pressures on the cylinder surface measured at different spanwise locations. Typically the correlation between variables at different spanwise locations increases as the amplitude of oscillation increases, as shown for example by the results of Toebes (1969), figure 1.22, and those of Novak and Tanaka (1975), figure 1.23.

Whether these increases are brought about by events which are always present and for which the magnitude increases with oscillation amplitude, or are due to well-organized events for which the intermittency decreases with increased amplitude is unknown. Time-average measurements such as correlation coefficient cannot distinguish between the two.

1.4.3 Mode Jumping and Phase Change

The phase change referred to here is the change in phase of vortex shedding with respect to cylinder motion during lock-in. The fact that the frequencies of vortex shedding and cylinder motion coincide during lock-in implies that a definite phase relationship exists between the two. It is observed that the phase varies with reduced velocity. As pointed out above (see fig. 1.21), some experimenters have observed rapid changes in phase angle with changes in reduced velocity (e.g. Bishop & Hassan 1964 b, Stansby 1976, Parkinson, Feng & Ferguson 1968). Others (e.g. Protos, Goldschmidt & Toebes 1968) have observed a more gradual change. It now seems that one of the causes of rapid phase change is a change in wake topology (Williamson & Roshko 1988). This is what was referred to above as "mode jumping".

Before continuing, it will prove useful to briefly discuss the phase of wake forces with respect to cylinder motion before the topic is taken up in more detail below. The phase of force with respect to displacement can be shown using the familiar "rotating vector" format as in figure 1.24. The convention adopted is the usual one for mechanical

[5] For the fixed cylinder, Koopman's flow visualization showed slantwise vortex shedding, producing a linear variation of phase along the span. This reflects the very low Reynolds number, as at higher Reynolds number the phase variation along the span tends to be more random.

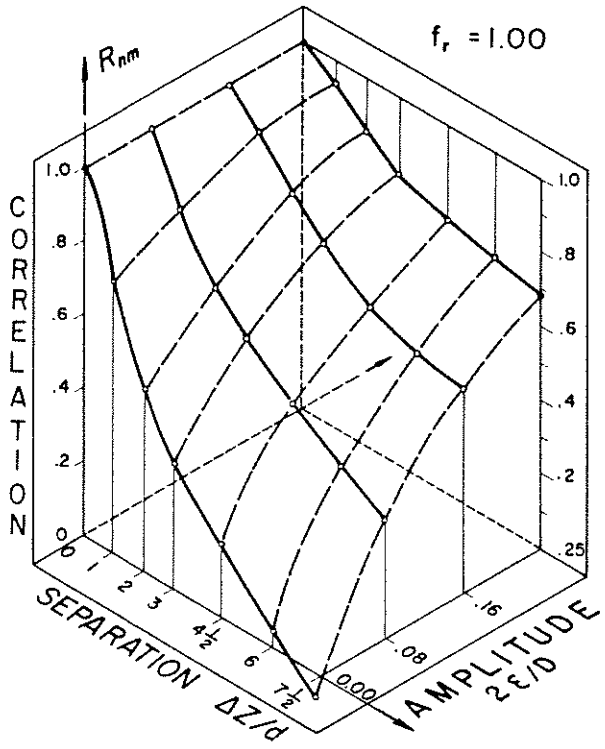

FIGURE 1.22: Variation of correlation coefficient R_{nm} between wake velocities at different points along the span as functions of oscillation amplitude. Here, f_r is the ratio of fixed cylinder Strouhal and forced cylinder oscillation frequencies (equal in this case). After Toebes (1969).

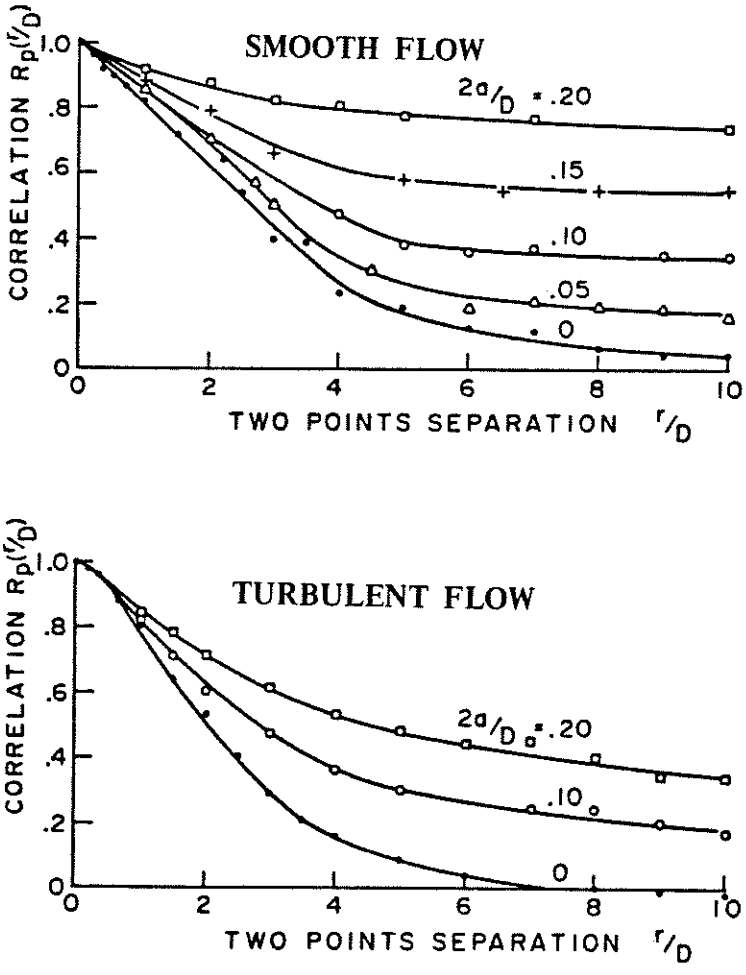

FIGURE 1.23: Spanwise distributions of correlation coefficient between pressures measured on a cylinder forced to oscillate cross flow as functions of amplitude. Smooth subcritical flow. After Novak & Tanaka (1975).

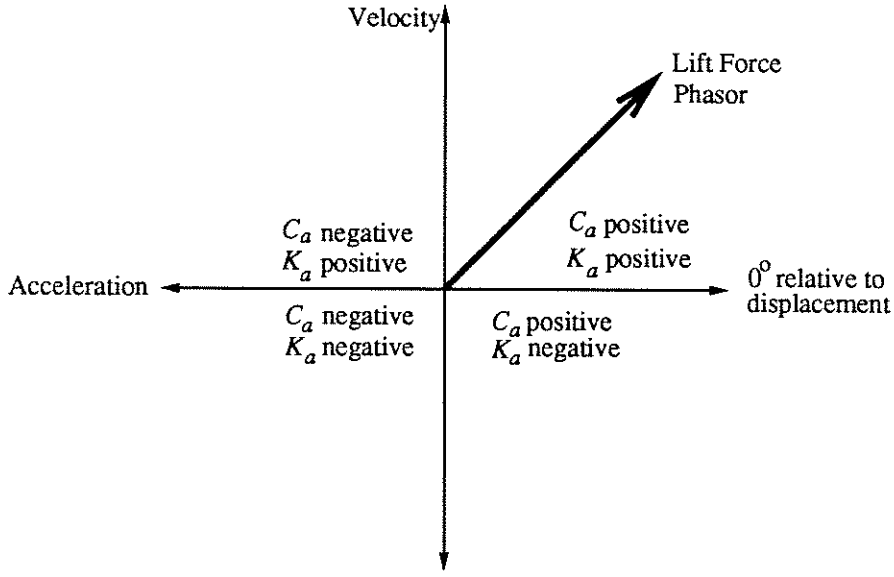

FIGURE 1.24: Phasor diagram showing phase of vortex shedding forces with respect to cylinder motion, with indication of signs of motion-correlated force coefficients C_a & K_a.

systems in harmonic motion; velocity leads displacement by 90°, acceleration by 180°. Shown in the four quadrants are the sign of coefficients of motion-correlated forces C_a and K_a (it can be deduced that C_a describes forces out of phase with acceleration, K_a forces in phase with velocity). It should be evident that for freely-vibrating cylinders, only forces with phases in the range 0° to 180° will be observed, since forces with phases in the range 0° to −180° will tend to damp out oscillation. Inspection of Feng's results (fig. 1.16), which show the phase of suction at a tapping 90° from the front of the cylinder bears this out. No such restriction applies to forces during forced oscillation.

Figure 1.16 illustrates that there was a step change in phase from less than 50° to more than 100° near $\mathsf{U} = 1.0$. This corresponds to a rapid change from some component of wake force being out of phase with cylinder acceleration to being in phase. Indeed there was a corresponding small increase in cylinder oscillation frequency at the same point, as would be expected (although it is a little peculiar that the frequency remained below f_n, the figure measured "*in vacuo*"). The forced oscillation results of Bishop and Hassan (1964) show a similar sharp jump in phase ($Re = 8900$, $\alpha = 0.2$). By contrast, the results of Protos, Goldschmidt and Toebes (1968) at $Re = 4.6 \times 10^4$, $\alpha < 0.14$, while they show variations in phase, do not exhibit a step change near $\phi = 90°$, as shown in figure 1.25.

Williamson and Roshko (1988) presented results from an interesting set of experiments conducted using a water tank and a computer controlled carriage with cylinder which projected into the water, together with a camera. Flow visualization was carried out using aluminium particles which were distributed on the surface of the water. Using this apparatus, they were able to observe the flows which occurred for $0 < \alpha < 5$, $0 < V_r < 15$ in the Reynolds number range $300 < Re < 1000$. A number of differ-

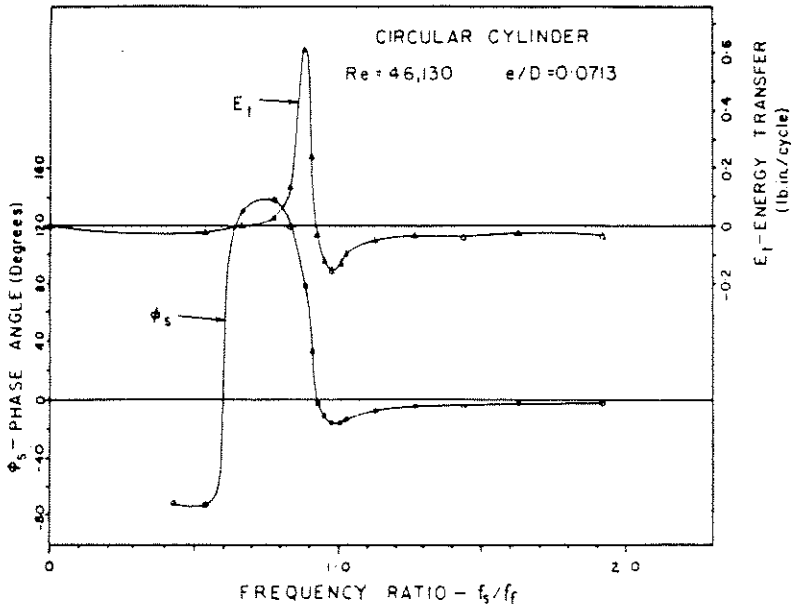

FIGURE 1.25: Phase of vortex shedding forces with respect to cylinder displacement (ϕ_s) as a function of the ratio of frequency of cylinder oscillation to frequency of vortex shedding for the fixed cylinder (f_s/f_f) at $Re = 4.6 \times 10^4$, $\alpha = 0.07$. After Protos, Goldschmidt & Toebes (1968).

ent modes of vortex shedding were observed in which 2, 3, 4 or more distinct vortices were formed per cycle of cylinder oscillation. A subset of their results is shown in diagrammatic form in figure 1.26.

From the point of view of vortex-induced vibration, only the values of amplitude $\alpha < 1.0$ are significant. It can be seen that the lower amplitude section of the 2S and 2P regions, taken together, form the primary lock-in region. Note the similarity in form to Stansby's results (fig. 1.21), including the line he found for a sudden change in phase of wake velocity with respect to cylinder motion. It seems that this sudden change in phase, also reflected in the results of Bishop and Hassan (1964 b) and Parkinson, Feng and Ferguson (1968), corresponds to a mode jump from two vortices shed per cycle of cylinder motion (2S mode) to four per cycle (2P mode). The sudden jump in phase is produced by a change in wake topology. The lack of such a jump in the results of Protos, Goldschmidt and Toebes (fig. 1.25), for example, might be explained by the fact that the amplitudes of vibration in their experiment were below those required for complete lock-in, and the values of phase that they found reflect average values as vortex shedding jumped in and out of synchronization with cylinder motion.

Another important finding contained in Williamson and Roshko's results is that, at the extremes of the primary lock-in region, four vortices are created per cycle of cylinder acceleration, two at each acceleration maximum, like a new set of starting or Föppl vortices. The 2S mode is a result of coalesence in the near wake region of vortices of like sign, which occurs at the low-V_r end of the lock-in range. The 2P mode is the result of vortex pairing, but non-coalesence, which occurs at the high-V_r end of the lock-in range. Whether the 2S or 2P mode occurs seems to depend on the relationship between the timescale of vortex convection in the wake and the period of cylinder

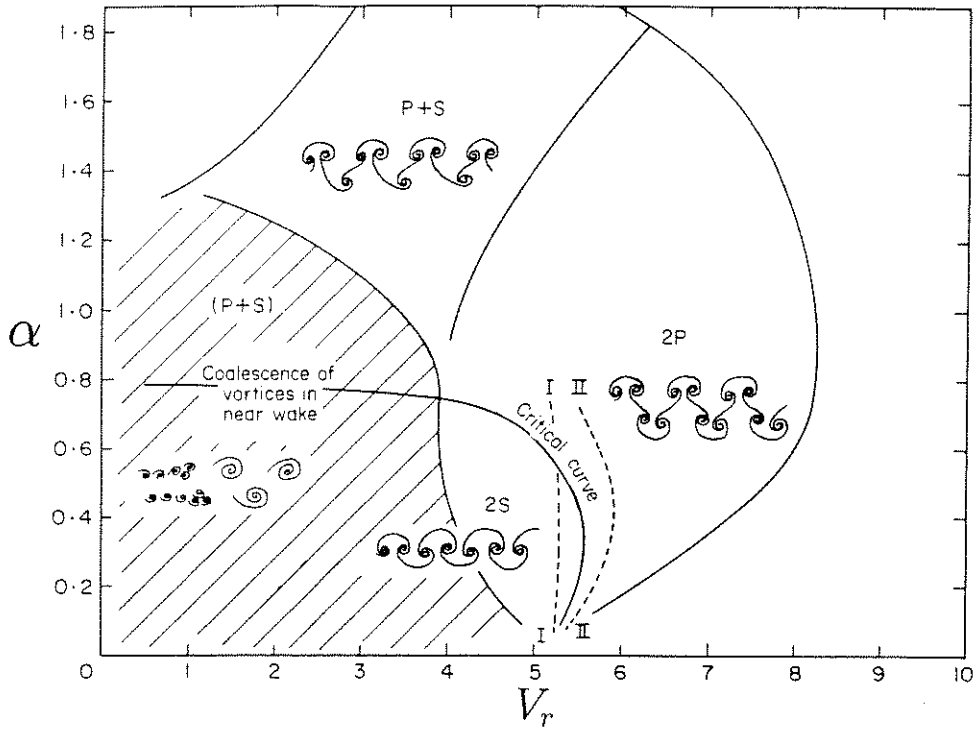

FIGURE 1.26: Vortex shedding modes for forced cylinder oscillations observed by Williamson & Roshko (1988).

motion. In between these two extremes, at the range of V_r around 5 where the maxima in vortex-induced forces are observed, only two vortices are formed per cycle of cylinder motion. This suggests that the increased spanwise correlation of vortices in the lock-in regime is a result of the fact that the vortices are formed as new sets of starting vortices, with a fixed phase relationship along the span.

There is another phase change in the wake, which may or may not be associated with change of wake topology. This is the change from positive to negative values of ϕ, which, as pointed out above, is only likely to be observed in forced oscillation experiments. This change in phase, reflected in the change of sign of energy transfer in figure 1.25, should be reflected in a switch of timing of vortex formation, or at least in the phasing of the dominant regions of low pressure in the near-wake. Just such a change can be seen in figure 1.27, which shows the results of flow visualization carried out by Ongoren and Rockwell (1988), performed at similar Reynolds numbers to those used by Williamson and Roshko, but using timeline rather than streakline flow visualization. Also apparent is the shortening of the vortex formation region as V_r (proportional to f_0^*/f_e) was decreased. Zdravkovich (1982) provides further discussion on this topic.

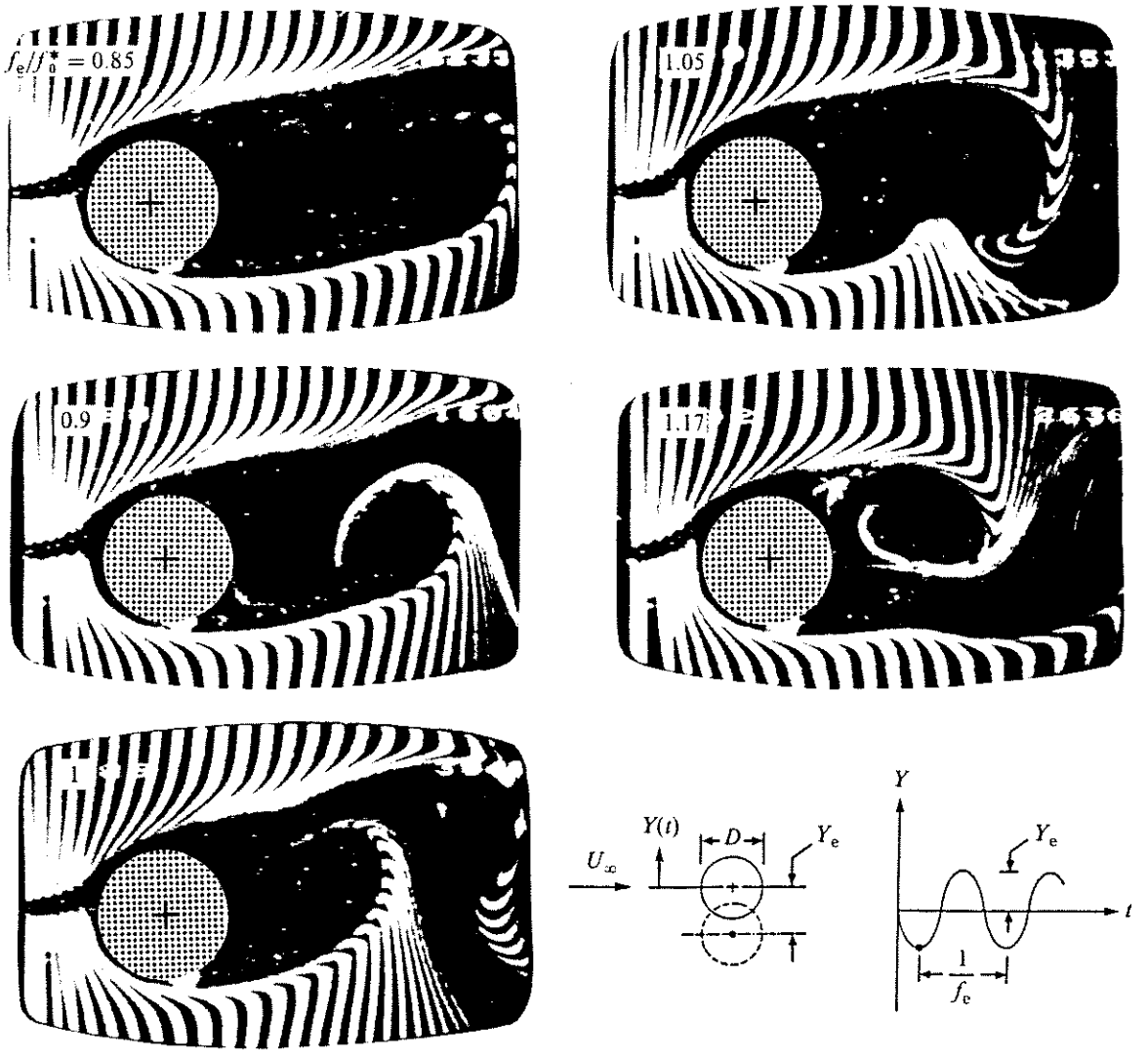

FIGURE 1.27: Flow visualization by Ongoren & Rockwell (1988) which shows the change of phase of vortex shedding with respect to cylinder motion. The ratio f_e/f_0^* shown with each photograph is the ratio frequency of forced cross-flow oscillation (f_e) to frequency of vortex shedding from the stationary cylinder (f_0^*). All photos taken at maximum negative displacement of cylinder. Oscillation amplitude $\alpha = 0.13$, $Re \approx 885$.

1.4.4 Response Amplitudes and Stability Boundaries

For structures with small mass-damping (but sufficient that they oscillate near their *in vacuo* natural frequency), the response amplitude at any Reynolds number is a function of V_r and K_s. One way of characterizing this is to draw contours of response amplitude on a graph with V_r and K_s as the axes; figure 1.28 (a) shows such a plot for $\alpha = 0.01$, taken from the results of Parkinson, Feng and Ferguson (1968). Two points which can be made here are that the range of V_r for significant response increases as K_s is reduced, and that it extends predominantly in the range of $V_r > 5$. To the left of the contour, the "unstable" region, it might be assumed that lock-in occurs, although it is likely that this in fact happens at amplitudes somewhat greater than $\alpha = 0.01$, on the basis of figure 1.21.

If one were to draw contours of greater amplitude, then a diagram such as that of figure 1.28 (b) would be obtained. A section through such a plot at some particular value of V_r would then show how amplitude varies with K_s, as for example in figure 1.29, taken from results measured on a linear mode-shape model stack by Wootton (1968, 1969). This shows that α increases rather slowly as K_s is reduced from high values, until near $K_s = 0.5$ the amplitude of oscillation increases rapidly with decreases in K_s. Finally, in the limit $K_s \to 0$, a maximum value of α is approached, $\alpha_{\mathrm{rms}_{\max}} \approx 0.16$ in this case.

At the smaller response amplitudes, when the amplitude increased slowly with decrease in K_s, Wootton's results showed that the RMS amplitude varied with $K_s^{-1/2}$. This is significant because it is similar to that of a lightly-damped linear system subject to (comparatively) wide-band random forcing (Newland 1984, ch. 14). In other words, at low response amplitudes the vibration is forced, rather than self-excited.

As the amplitude of response increases, the nature of the response as characterized by its probability density function changes, reflecting the increased wake organization produced by the structural oscillation. This effect is illustrated by the results obtained by Kwok (1977), presented in figure 1.30. This shows how the normalized upcrossing frequency of a lightly-damped circular tower model changed from that appropriate to a Gaussian-(normally)-distributed process towards that for a sinusoidal process and back again as the reduced velocity was traversed from below to above the lock-in range.

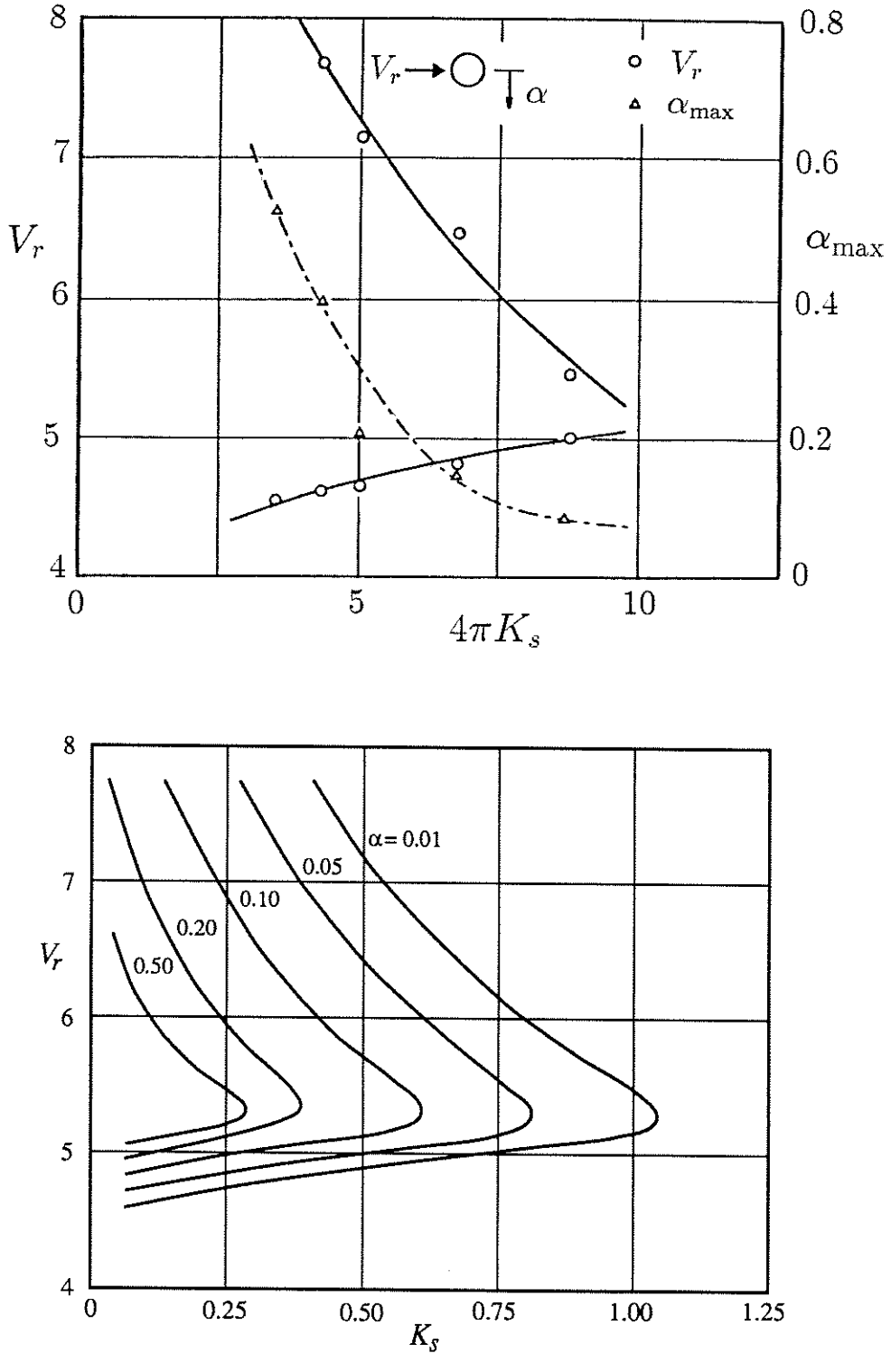

FIGURE 1.28: Contours of response amplitude as functions of V_r and K_s, (a); measurements presented by Parkinson, Feng & Ferguson (1968) with $\alpha = 1\%$, (b); conjectured contours for different values of α.

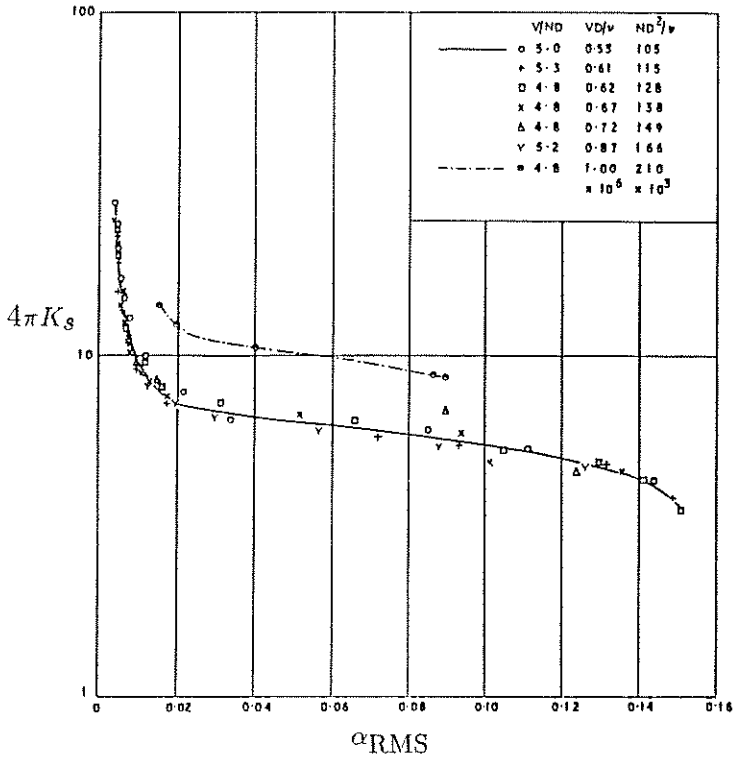

FIGURE 1.29: Response amplitude α_{rms} as a function of K_s for a linear mode shape model with 11.5:1 aspect ratio. After Wootton (1968, 1969). Here, N is frequency and V is the mean flow speed.

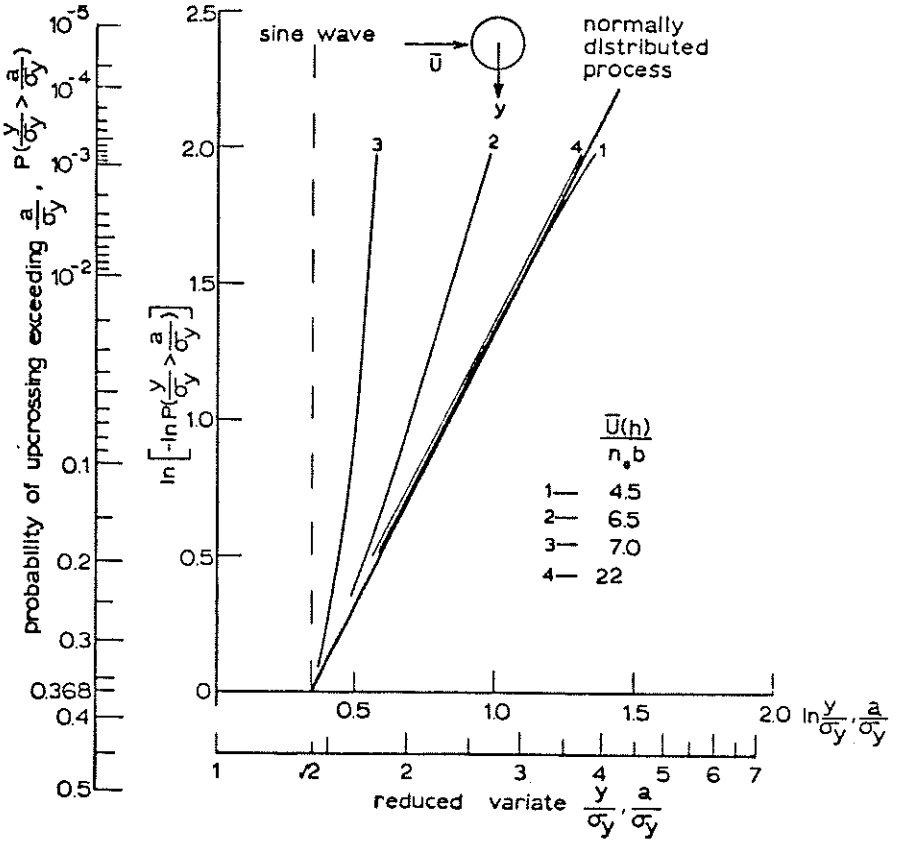

FIGURE 1.30: Variation of response PDF for a lightly-damped circular tower model, as reflected in changes to the curves of normalized upcrossing frequency. After Kwok (1977).

1.4.5 Effect of Turbulence on Interaction between Cylinder Motion and Vortex Shedding

Very little information is available concerning the effect of turbulence on the interaction between vortex shedding and cylinder motion. Indirect evidence, such as observations of the response of circular stacks, suggests that the presence of turbulence is able to disrupt the interaction, since large amplitude responses are almost invariably observed in flows of low turbulence intensity. However, experiments conducted by Novak and Tanaka (1975) in which spanwise correlations of pressures were measured in subcritical flows showed that the spanwise correlation increased with cylinder oscillation amplitude in both smooth and turbulent flows.

An attempt has been made to incorporate the effects of turbulence into the response prediction scheme produced by Vickery and Basu (1983 a, to be discussed in § 1.7.5). This was done by allowing for a quasi-steady variation in mean flow speed in the description of motion-correlated forces used in the model, leading to a reduction in motion-correlated forces near lock-in. So far, no direct experimental evidence has come to light which supports this hypothesis.

1.5 Lift Forces on Stationary Cylinders

Now that the general aspects of vortex shedding downstream of fixed and oscillating circular cylinders have been discussed, the emphasis changes to examination of experimental measurements of lift forces. This section deals with lift forces on stationary cylinders, while lift forces on oscillating cylinders will be dealt with in the next.

Cross flow (lift) forces form the centre of attention, with limited reference being made to along flow (drag) forces. The distinction between along and cross flow force is based on the assumption that separate mechanisms produce the forces in the two directions. This assumption is most valid in turbulent flows, and at small amplitudes of structural vibration. In this case it has been observed that the fluctuating drag forces are dominated by effects due to the streamwise components of turbulence. In smooth flows, and at high response amplitudes, the distinction does not hold, since the fluctuating forces in both directions are produced by the same mechanism (see Vandiver & Jong 1987).

Some preliminary aspects are discussed in §§ 1.5.1 and 1.5.2 below. The relationship between lift force per unit length of cylinder measured at a section of the cylinder and average lift force per unit length measured on a finite length of cylinder is addressed in § 1.5.1. The two quantities are not the same as a result of the lack of spanwise correlation of vortex shedding. The influence of wind tunnel walls and cylinder end conditions on measurements of lift force is examined in § 1.5.2.

1.5.1 Spanwise Correlation of Forces

When comparing coefficients of lift from one experiment to another, the means by which the lift forces were measured must be considered. Since it is observed that the

correlation of lift forces reduces with axial displacement of the measurement stations, localized lift forces are best measured on short lengths of cylinder, or by measurements of fluctuating pressures at one axial location. In many experiments, fluctuating forces have been measured on the entire length of the cylinder spanning the tunnel working section. If the local forces and their axial relationship are spanwise homogeneous, and if the distribution of spanwise correlation of lift forces is known, then it is possible to estimate local RMS lift forces given the RMS force per unit length acting on the whole cylinder, or *vice versa*. This provides a means of comparison of measurements made on short sections of cylinder with those made on a whole cylinder. A method by which this may be done is set out below.

Conversion of $\sigma_{C_{l_{\text{total}}}}$ to $\sigma_{C_{l_{\text{local}}}}$

With the provisos given above concerning spanwise homogeneity, it is possible to convert values of σ_{C_l} computed using measurements of forces acting on a whole or some finite length of cylinder ($\sigma_{C_{l_{\text{total}}}}$) to values for a section of cylinder ($\sigma_{C_{l_{\text{local}}}}$), if the form of the spanwise correlation function ρ_λ is known. The correlation function describes the spanwise distribution of the correlation coefficient, or normalized covariance. By definition, it has a value of unity when the spanwise separation between two measurement stations is zero. Often, the information contained in the correlation function is condensed into the *correlation length* Λ:

$$\Lambda = \int_0^\infty \rho_\lambda \, d\lambda \, , \tag{1.2}$$

where λ is a dimensionless spanwise displacement, $\lambda = z/D$. The correlation length gives an indication of the spanwise extent of forces which act on the cylinder at any instant.

The spectrum of total lift force

$$\begin{aligned} S_l(f) &= \int_0^L \int_0^L S_{ll}(z_1, z_2, f) \, dz_1 \, dz_2 \\ &= D^2 \int_0^{L/D} \int_0^{L/D} S_{ll}(\lambda_1, \lambda_2, f) \, d\lambda_1 \, d\lambda_2 \, , \end{aligned} \tag{1.3}$$

where L is the span of the cylinder. With the assumption of homogeneity,

$$S_l(f) = S_{l_{\text{local}}}(f) \, D^2 \int_0^{L/D} \int_0^{L/D} R_{ll}(\lambda_1, \lambda_2, f) \, d\lambda_1 \, d\lambda_2 \, , \tag{1.4}$$

where $R_{ll}(\lambda_1, \lambda_2, f)$ is a *narrow-band correlation function* (normalized cross-spectrum). If the narrow-band correlation is not a function of frequency, as is usually the case, it may be replaced by the correlation function $\rho_\lambda = \rho(|\lambda_1 - \lambda_2|)$, to give

$$\begin{aligned} S_l(f) &= S_{l_{\text{local}}}(f) \, D^2 \int_0^{L/D} \int_0^{L/D} \rho_\lambda \, d\lambda_1 \, d\lambda_2 \\ &= S_{l_{\text{local}}}(f) \, 2 \, D^2 \int_0^{L/D} \int_0^{\lambda_2} \rho_\lambda \, d\lambda_1 \, d\lambda_2 \, . \end{aligned} \tag{1.5}$$

To make further progress, the shape of the correlation function must be known. Here, a function used in chapter 5 for extrapolation of results is introduced;

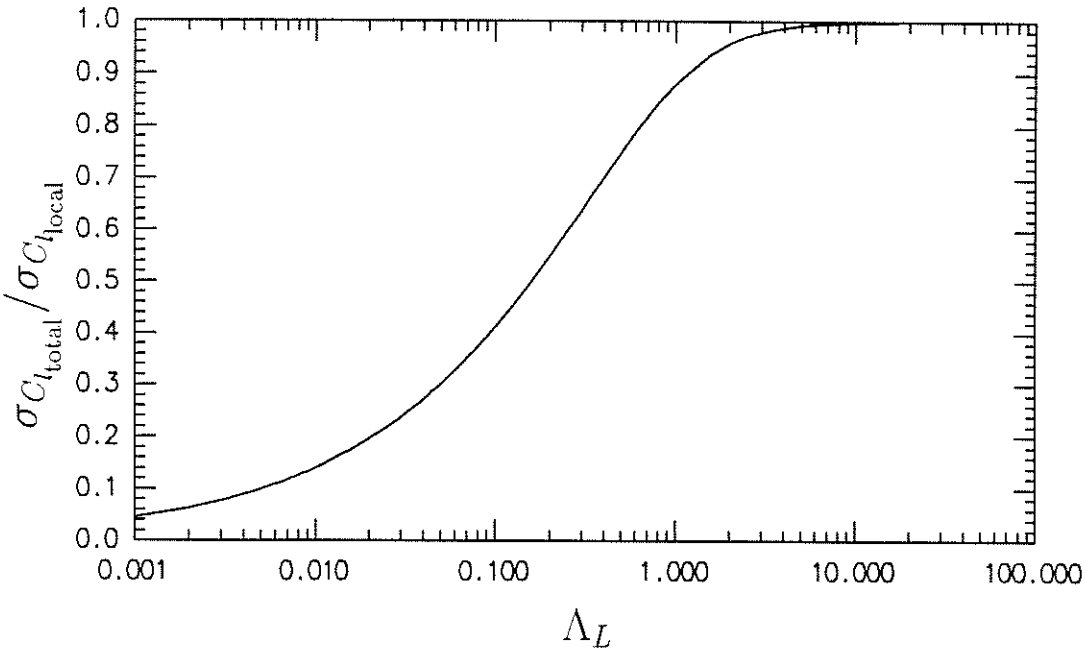

FIGURE 1.31: The ratio $\sigma_{C_{l_{\text{total}}}}/\sigma_{C_{l_{\text{local}}}}$ as a function of the ratio of correlation length to span Λ_L for a correlation function $\rho_\lambda = 1/\left(1+\left(\frac{\pi}{2\Lambda}\right)^2(\lambda_1-\lambda_2)^2\right)$.

$$\rho_\lambda = \frac{1}{1+\left(\frac{\pi}{2\Lambda}\right)^2(\lambda_1-\lambda_2)^2}\,. \tag{1.6}$$

With the use of this function, it can be verified that

$$S_l(f) = S_{l_{\text{local}}}(f)\,\frac{8D^2\Lambda^2}{\pi^2}\left\{\frac{\pi L}{2D\Lambda}\arctan\frac{\pi L}{2D\Lambda} - \frac{1}{2}\ln\left[1+\left(\frac{\pi L}{2D\Lambda}\right)^2\right]\right\}\,. \tag{1.7}$$

Introducing $\Lambda_L = D\Lambda/L$, which describes the correlation length as a proportion of span, rather than diameter, equation (1.7) can be written

$$S_l(f) = S_{l_{\text{local}}}(f)\frac{4L^2\Lambda_L}{\pi}\left\{\arctan\frac{\pi}{2\Lambda_L} - \frac{\Lambda_L}{\pi}\ln\left[1+\left(\frac{\pi}{2\Lambda_L}\right)^2\right]\right\}\,, \tag{1.8}$$

and since $S_{l_{\text{total}}}(f) = S_l(f)/L^2$, where $S_{l_{\text{total}}}(f)$ is the spectrum of lift force per unit length,

$$\frac{\sigma_{C_{l_{\text{total}}}}}{\sigma_{C_{l_{\text{local}}}}} = \left(\frac{4\Lambda_L}{\pi}\left\{\arctan\frac{\pi}{2\Lambda_L} - \frac{\Lambda_L}{\pi}\ln\left[1+\left(\frac{\pi}{2\Lambda_L}\right)^2\right]\right\}\right)^{1/2}\,. \tag{1.9}$$

This ratio is plotted in figure 1.31 as a function of Λ_L. The shape of the curve is not sensitive to the form of correlation function assumed: the relationship given by Howell and Novak (1979) for an exponential correlation function $\rho_\lambda = \exp(-|\lambda_1-\lambda_2|/\Lambda)$ gives similar results.

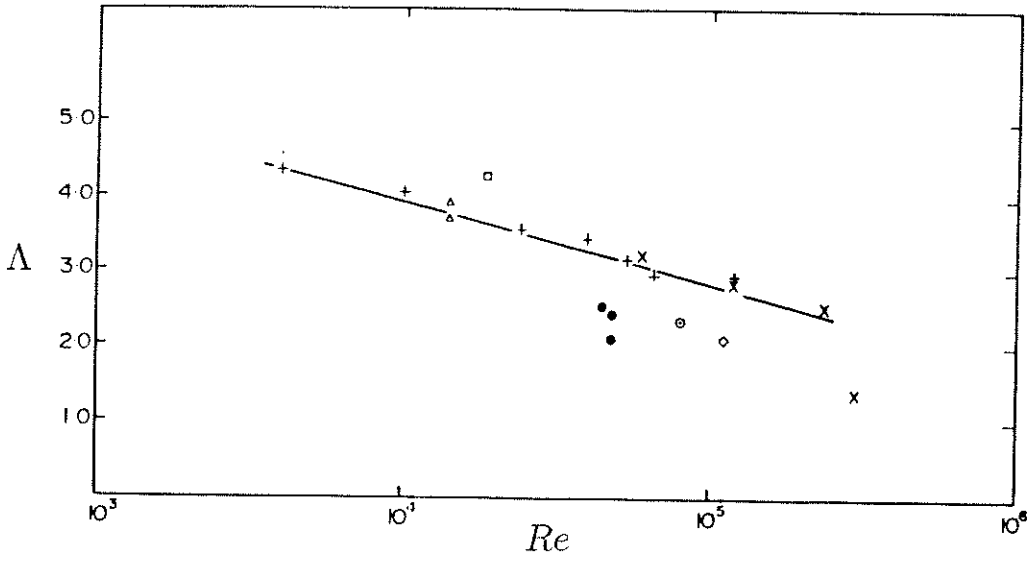

FIGURE 1.32: Compilation of correlation lengths for pressure fluctuations at 90° from the leading generator of the cylinder (after Bruun & Davies 1975). +, △, □, ◇, ×; $I_u < 0.5\%$, ⊙; $I_u = 4\%$, ●; $I_u = 10$–14%.

Correlation Lengths

A compilation of measurements of the spanwise correlation lengths of fluctuating pressures on circular cylinders at the $\theta = 90°$ position from the leading generator of the cylinder in subcritical smooth and turbulent flows was presented by Bruun and Davies (1975). This is reproduced here as figure 1.32. Note that no measurements of correlation lengths for transcritical flows past smooth cylinders have yet been published.

1.5.2 Wind Tunnel Measurements and Wall Effects

The relative advantages and disadvantages of wind tunnel measurements compared to measurements made in the field on full scale structures have been discussed by Vickery and Daly (1984). In brief, wind tunnel measurements have the advantages of ease of control and measurement of experimental parameters, and low cost. The main disadvantage of wind tunnel measurements, related to cost, is that measurements at high Reynolds numbers are difficult to make, particularly when combined with levels of turbulence intensity and scale appropriate to full scale structures. In field measurements, it may be difficult to measure the parameters such as turbulence properties, and it is rarely the case that the wind blows with the same mean speed and direction for a significant period of time. This makes it difficult to obtain repeated readings with the same set of parameters.

Experiments conducted for fixed cylinders in air generally suffer from a restriction in Mach number which means that large Reynolds numbers require large cylinder diameters and hence wind tunnels. If the cylinder is intended to oscillate, another restriction is imposed by limitations on the permissible fluctuating stresses in the materials from which the model is constructed. Dimensional analysis shows that an equipment design

which is operating on the limits of permissible stress at one Reynolds number can only be made to operate successfully at a higher Reynolds number by changing the scale of the model (diameter), rather than flow velocity, due to the constraint on frequency imposed by a fixed reduced velocity. Both these limitations are reflected in the fact that all wind tunnel tests which have so far been conducted on circular cylinders at Reynolds numbers greater than 1×10^6 (e.g. Roshko 1961; Jones, Cincotta & Walker 1969; Wootton 1969; van Nunen 1972; Szechenyi (1974, 1975); Schewe 1983) have all used compressed air or Freon as a fluid.

Wall Effects

In all wind tunnel measurements of aerodynamic coefficients, notice must be taken of the effects on the measured coefficients brought about by the presence of wind tunnel walls. Wall corrections for measurements made on streamlined bodies based on theoretical considerations have been proposed and are often used in wind tunnel measurements of forces on model aircraft and components (Pope & Harper 1966). In bluff body flows, the situation is more difficult since there is no convincing theory on which to base corrections. The effects can be placed into three main classes:

1. Tunnel Blockage
2. Aspect Ratio
3. End Effects

Unfortunately, there are insufficient experimental data to fully quantify the effects, particularly in turbulent transcritical flows. Most of the available experimental data relate to subcritical flows. To make things less clear, it has often not been recognized that these three classes may produce separate effects on the measured force coefficients. For instance, cylinder aspect ratio and tunnel blockage have been varied simultaneously in many experiments. West and Apelt (1982) studied the variation in base pressures and drag coefficients of cylinders caused by changes in aspect ratio and blockage for smooth subcritical flows. They showed that independently decreasing the aspect ratio or increasing tunnel blockage each had the effect of increasing the coefficient of drag (fig. 1.33).

Blockage Tunnel blockage is caused by the fact that wind tunnel walls constrain the flow past any object, so that streamlines of the flow are distorted from what they would be if the object were placed in an infinite uniform flow. The tunnel blockage is usually described by the *blockage ratio*, which is the ratio of the model projected area to the tunnel working section area. The effects of tunnel blockage on circular cylinders are complex, mainly as a result of the fact that the separation point is free to take up any position on the cylinder. Blockage can be thought of as having two interlinked effects. The first is that by constraining the wake, blockage influences the separation point by changing the pressure gradients on the body. The second is that the increase of local velocity on the boundary of the cylinder brought about by constraint has the effect of raising the Reynolds number, which also influences the type of separation that occurs.

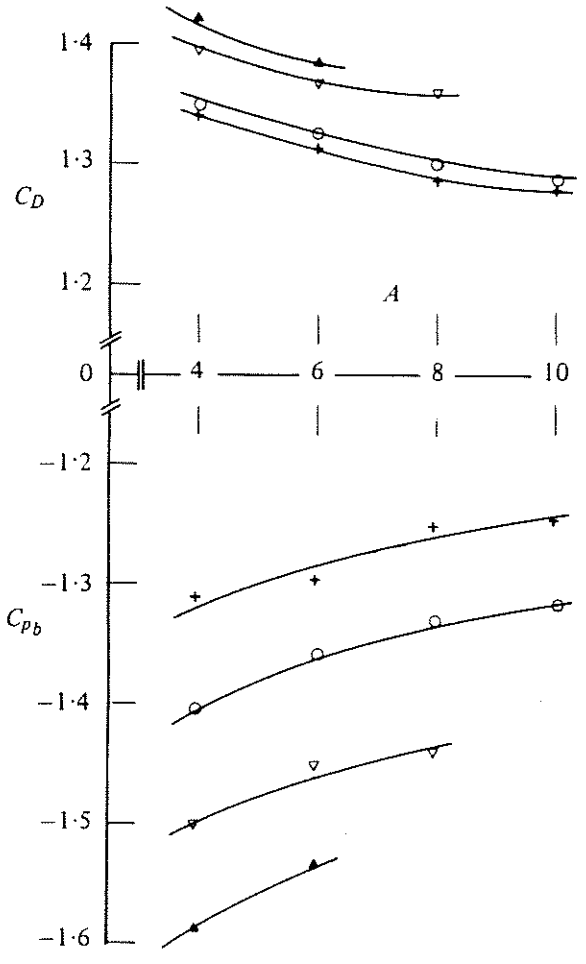

FIGURE 1.33: Variation of drag coefficient (C_D) and base pressure coefficient with aspect ratio at $Re = 6 \times 10^4$. Blockage ratio: $\triangle$; 16%, $\triangledown$; 12.5%, $\odot$; 9%, +; 6%. After West & Apelt (1982).

It is very difficult to account for these effects, particularly near the critical range of Reynolds number, where the flow regimes are sensitive to disturbances.

Semi-empirical corrections for wind tunnel blockage of bluff-body flows were proposed by Glauert (1933), Allen and Vincenti (1944) and Maskell (1965). All methods presume that the effects of blockage can be accounted for by an increase in free-stream dynamic pressure, with no change in the shape of the pressure distribution. Maskell argued that the pressure distribution around the bluff body is "invariant under constraint", i.e. that the shape of the pressure distribution does not change with blockage, and that effects can be accounted for by a change in the free stream velocity. The resulting corrections for coefficient of drag have been shown to produce reasonable results on sharp-edged bluff bodies, but in fact the assumption of invariance is not needed to arrive at that correction. Melbourne (1982) showed that for sharp edged circular plates held normal to the flow, Maskell's correction for drag coefficient was satisfactory, but that the pressure distribution was not invariant under constraint (most of the effect being confined to base pressure).

In the absence of satisfactory theoretical or semi-empirical methods of correcting pressure distributions or fluctuating lift on circular cylinders, the experimental evidence must be examined. The only systematic investigation of lift forces in which the end effects and aspect ratio were held constant while the blockage varied is that of Richter and Naudascher (1976). They measured forces on a $6.8\,D$ long section of an 8.6:1 aspect ratio cylinder in smooth flows in the Reynolds number range (based on upstream velocity) $2 \times 10^4 < Re < 4 \times 10^5$, with blockages of 1/6, 1/4, 1/3 and 1/2. They found substantial blockage effects, the most pronounced being on the RMS coefficient of lift, as shown here in figure 1.34. The results of Keefe (1962), shown in the figure, are not strictly comparable, since they were obtained on a $1\,D$ long section of a high aspect ratio cylinder (with a blockage of 2.3%), and so would be lower if corrected to a $6.8\,D$ long active section of cylinder, because of the lack of spanwise coherence of lift force. Similarly, the results presented by Richter and Naudascher cannot be manipulated to give sectional coefficients of lift, since no measurements of spanwise correlation are presented. It may well be that part of the observed increase in coefficients of lift with blockage ratio are due to increased spanwise coherence of vortex shedding. All the same, the implication is that increasing blockage from zero to 1/6 (16.7%) produces roughly double the lift force in subcritical flow. The effect in critical flow is less easy to discern from their results, which do not show what occurs at this lowest blockage.

Cheung (1983) carried out tests in the Reynolds number range 6×10^4 to 1×10^6, with substantial effort given to blockage correction of results. Unfortunately, both aspect ratio and tunnel blockage varied in his experiments. Despite this, his results are significant here, since he examined lower ranges of blockage than Richter and Naudascher, and provided results at higher Reynolds numbers *and in turbulent flows.* Specifically, two cylinders, one of aspect ratio 6.7:1 and a blockage of 8%, the other with aspect ratio 3.6:1 and blockage of 15%, were used for the examination of lift forces. Of the two uncorrected measurements of RMS coefficient of lift which he presented (his fig. 5.1), the one at 8% blockage may be compared with the measurements of Richter and Naudascher, since it is made in subcritical flow ($Re = 1 \times 10^5$), and at an aspect ratio of 6.7:1, which is similar to the 8.6:1 ratio used by Richter and Naudascher. The result is shown in figure 1.35, where the maximum RMS coefficient of lift in smooth subcritical

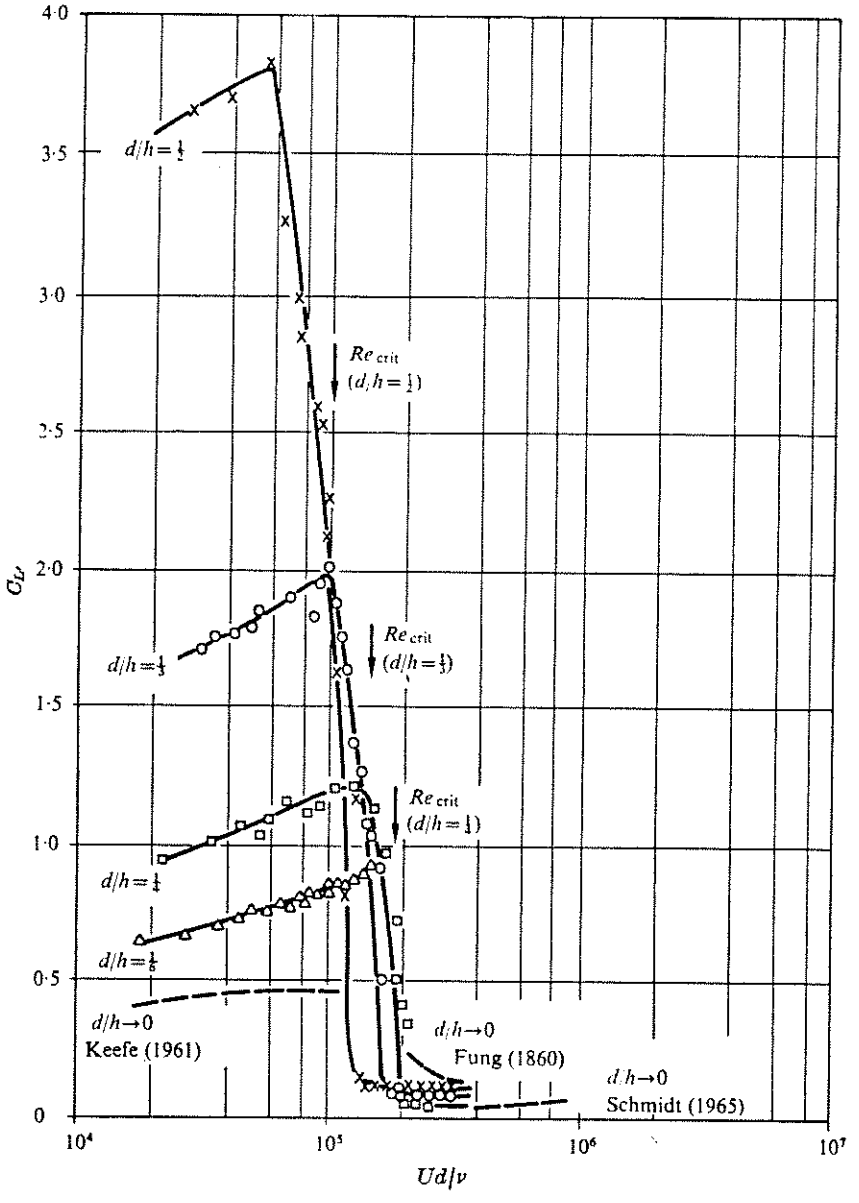

FIGURE 1.34: RMS lift coefficient $C_{L'}$ *vs.* Reynolds number Ud/ν for various blockage ratios on a 6.6 D section of an 8.6:1 aspect ratio cylinder in smooth flow (after Richter & Naudascher 1976).

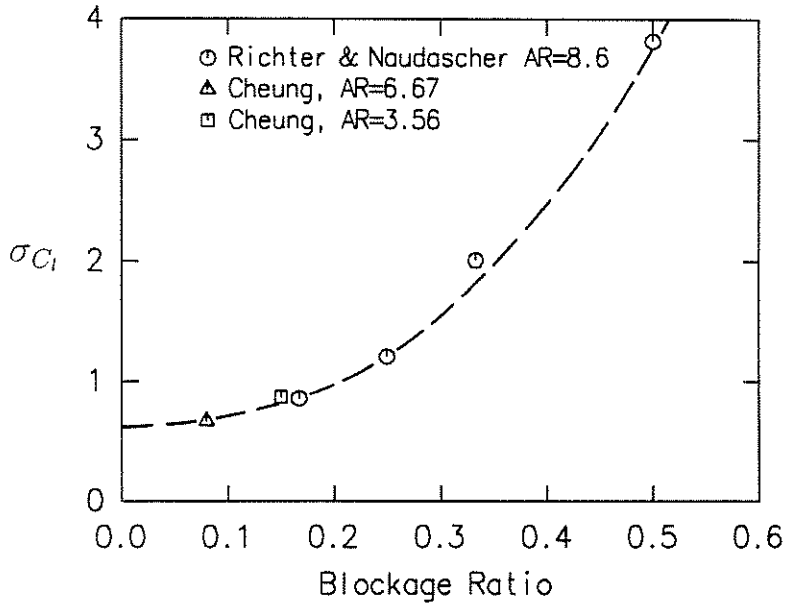

FIGURE 1.35: Maximum RMS coefficient of lift found in smooth subcritical flow as a function of tunnel blockage. Results of Richter & Naudascher (1976) and Cheung (1983).

flow is shown as a function of tunnel blockage. The inference from figure 1.35 is that the blockage correction to RMS lift coefficients in smooth subcritical flows is approximately a quadratic function of tunnel blockage.

For comparatively low blockage ratios (less than 0.15) in smooth subcritical flows ($Re < 1 \times 10^5$), Cheung suggested that a linear correction to fluctuating lift could be applied:

$$C_{l_c} = C_{l_m} - 2.7 \cdot (\text{blockage ratio}) , \tag{1.10}$$

where the subscripts c and m refer to corrected and measured quantities respectively.

Cheung found that in smooth flow, $1 \times 10^5 < Re < 2 \times 10^5$, the blockage correction was about ten times smaller than that suggested above. In turbulent flow ($I_u = 9.1\%$), and at Reynolds numbers larger than 1×10^5, he found no blockage correction was required. Presumably this was due to the wake being narrower than at subcritical Reynolds numbers.

In general, it can be concluded that while there is not enough experimental evidence available to enable blockage corrections to be reliably applied to fluctuating lift coefficients, the amount of correction which is needed drops with the width of the wake. In subcritical flows, with comparatively high coefficients of lift and large wake widths, the fluctuating lift force is sensitive to tunnel blockage. In supercritical flows, with small lift coefficients, the amount of correction required is probably small. The situation is less clear in transcritical flows, where the lift coefficients and wake widths become larger again (although still smaller than in subcritical flow).

Aspect Ratio There is some difficulty in considering the influence of aspect ratio and end effects separately, since a decrease in aspect ratio obviously brings the ends of

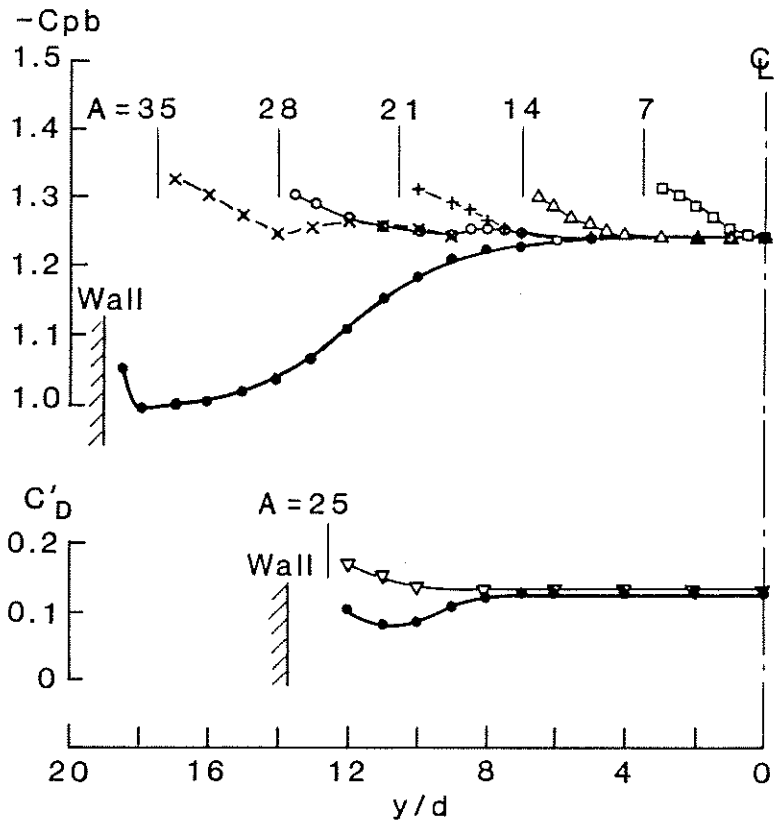

FIGURE 1.36: Distribution of base pressure on cylinders of varying aspect ratios measured at a Reynolds number of 4.4×10^5 and tunnel blockage of 4% by Fox & West (1990). A is aspect ratio, C'_D is RMS coefficient of drag and y/D is distance from tunnel centreline. The lower line in each part of the figure is for results obtained without end-plates.

the cylinder closer together.

It may be the case that the only effect of decreasing the aspect ratio is to increase the proportion of the cylinder over which end effects are felt. This is the implication of work reported by Fox and West (1990), who measured spanwise distributions of base pressure and RMS coefficient of lift at the centre section of a cylinder in smooth subcritical flow. In their experiment, the cylinder end plates (to Stansby's specifications, see § 1.5.2) could be moved in the spanwise direction, thus varying the aspect ratio of the cylinder while the tunnel blockage remained constant. Examining their results for base pressure coefficient (fig. 1.36), it can be seen that for all aspect ratios down to 7:1, there is a drop in base pressure (at most about 6%) near the end-plates which extends a length of about three cylinder diameters towards the centreline. The implication is that once aspect ratios fall below 7:1, the disturbance to the flow will extend over the whole length of the cylinder. Their measurements of coefficient of lift on the cylinder centreline (fig. 1.37) support this conclusion: the measured coefficients of lift at the centre of a 5:1 aspect ratio cylinder were about 7% higher than at the centre of 10:1, 15:1 and 25:1 aspect ratio cylinders.

By contrast, in earlier work by West & Apelt (1982), it was stated that the pressure was constant along the length of the cylinder, implying that end effects are felt over the entire length of cylinder. Their results (e.g. fig. 1.33) also show that the base pressure

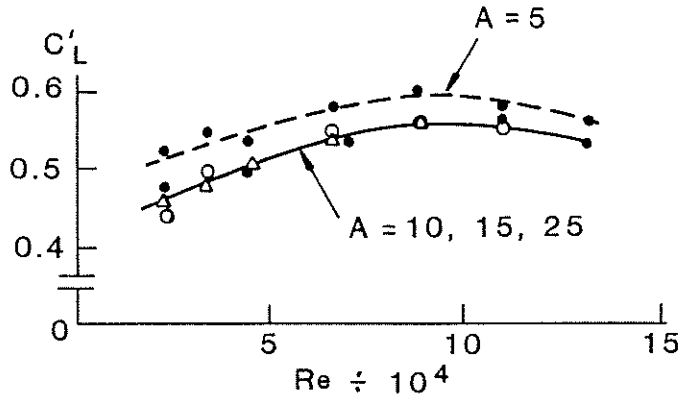

FIGURE 1.37: Measurements of RMS sectional coefficient of lift C'_L made at the centreline of cylinders of aspect ratios (A) 5:1, 10:1, 15:1 & 25:1 shown as functions of Reynolds number. Tunnel blockage 6%. After Fox & West (1990).

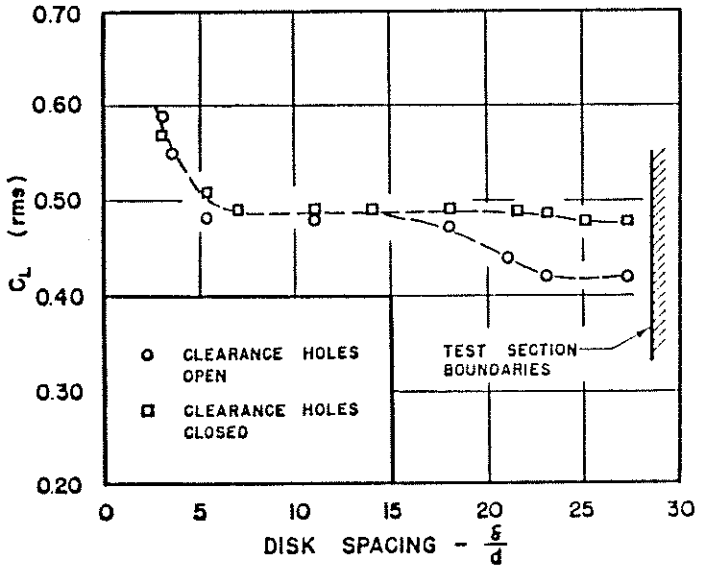

FIGURE 1.38: Variation in RMS coefficient of lift at the centreline of a cylinder brought about by varying cylinder aspect ratio in smooth subcritical flow (after Keefe 1962).

at the cylinder centreline was a function of aspect ratio, in contrast to the results of Fox & West (1990).

The influence of varying aspect ratio seen in the results of Keefe (1962) is similar to that found by Fox and West. Keefe measured fluctuating lift on a 1-diameter long central section of cylinder in smooth subcritical flow. Large circular end plates (4.9 D diameter) could be moved along the cylinder axis to give varying aspect ratios between the end plates, while maintaining the tunnel blockage at 2.3%. The variation in RMS coefficient of lift as a function of end-plate spacing is shown in figure 1.38. Again the conclusion which can be made is that the minimum aspect ratio for which there is no influence on lift at the centreline of the cylinder is about 7:1 in smooth subcritical flow. It was not clear from this experiment if the variation at low aspect ratios was due to the encroachment of end-effects, or spanwise-uniform changes.

As for the influence of aspect ratio in flows at higher Reynolds numbers, there is

very little experimental data. In part this reflects the fact that compromises must be made in the design of wind tunnel experiments: in the battle for high Reynolds numbers, large cylinder diameters tend to win out over high aspect and low blockage ratios. While some evidence of spanwise variation of pressures and forces has been reported at post-critical Reynolds numbers, no experiments to date directly examine the effect of varying aspect ratio.

The work of Higuchi, Kim and Farell (1989) was previously discussed (§ 1.3) in connection with low-frequency three-dimensional flow fluctuations in the precritical Reynolds number regime. They also presented plots of mean pressure distribution on their two cylinders (aspect ratios 8:1 and 5:1), which are reproduced here as figure 1.39. The blockage ratio was 11.8% for the AR = 5 cylinder and 13.9% for the AR = 8 cylinder. End plates to Stansby's specification (see below) were used in their experiments. While there is clear evidence of spanwise non-uniformity, it is not concentrated towards the ends of the cylinder.

Evidence of spanwise variation of base pressure coefficients in smooth critical flow was presented by Bearman (1969a, see fig. 1.40). Some caution should be applied in interpreting the results, since the cylinder spanned between the floor and ceiling of the working section without end-plates, and so the influence of wall boundary layers is unclear (see below). The experiments were carried out on a 12:1 aspect ratio cylinder with a tunnel blockage of 6.5%. In critical flow, the end effect on C_{pb} extends along the span for a distance of three to four diameters, with a section in the centre where the pressure is relatively uniform (in agreement with the results of Fox & West for subcritical flow).

End Effects There are substantial end effects associated with free ends of cylinders in a flow, due to the entrainment of fluid around the end of the cylinder into the low-pressure wake region. In order to diminish this effect, studies of flow around cylindrical shapes are usually conducted with the cylinder terminating at the tunnel wall or at large end plates. There is no geometric difference between the two, provided the size of the end plates are sufficiently large in relation to cylinder diameter. The reason why there is any difference between terminating the cylinder at end plates rather than at the tunnel wall has to do with the formation of "horseshoe" or "necklace" vortices at the junction of the cylinder and the wall (see e.g. Morton & Evans-Lopez 1986 and Lugt 1984).

For geometrically-similar boundary layer profiles, the size and characteristics of the horseshoe vortices can only be a function of the cylinder Reynolds number and the ratio of the cylinder diameter to boundary layer depth. In other words, the deeper the boundary layer, the bigger the horseshoe vortices as a proportion of cylinder diameter. The point of using end plates is to get rid of the wind tunnel wall boundary layer (by placing it between the end plate and the tunnel wall), while starting a new, thinner end plate boundary layer a short distance upstream of the cylinder. This will produce smaller horseshoe vortices. If the end plates extend too far upstream, their effectiveness will diminish. (Presumably end plates are not needed if the cylinder is placed not far downstream of a high area-ratio tunnel contraction.) On the other hand, unsteady effects in the wake of the cylinder were reported by Stansby (1974) when the upstream

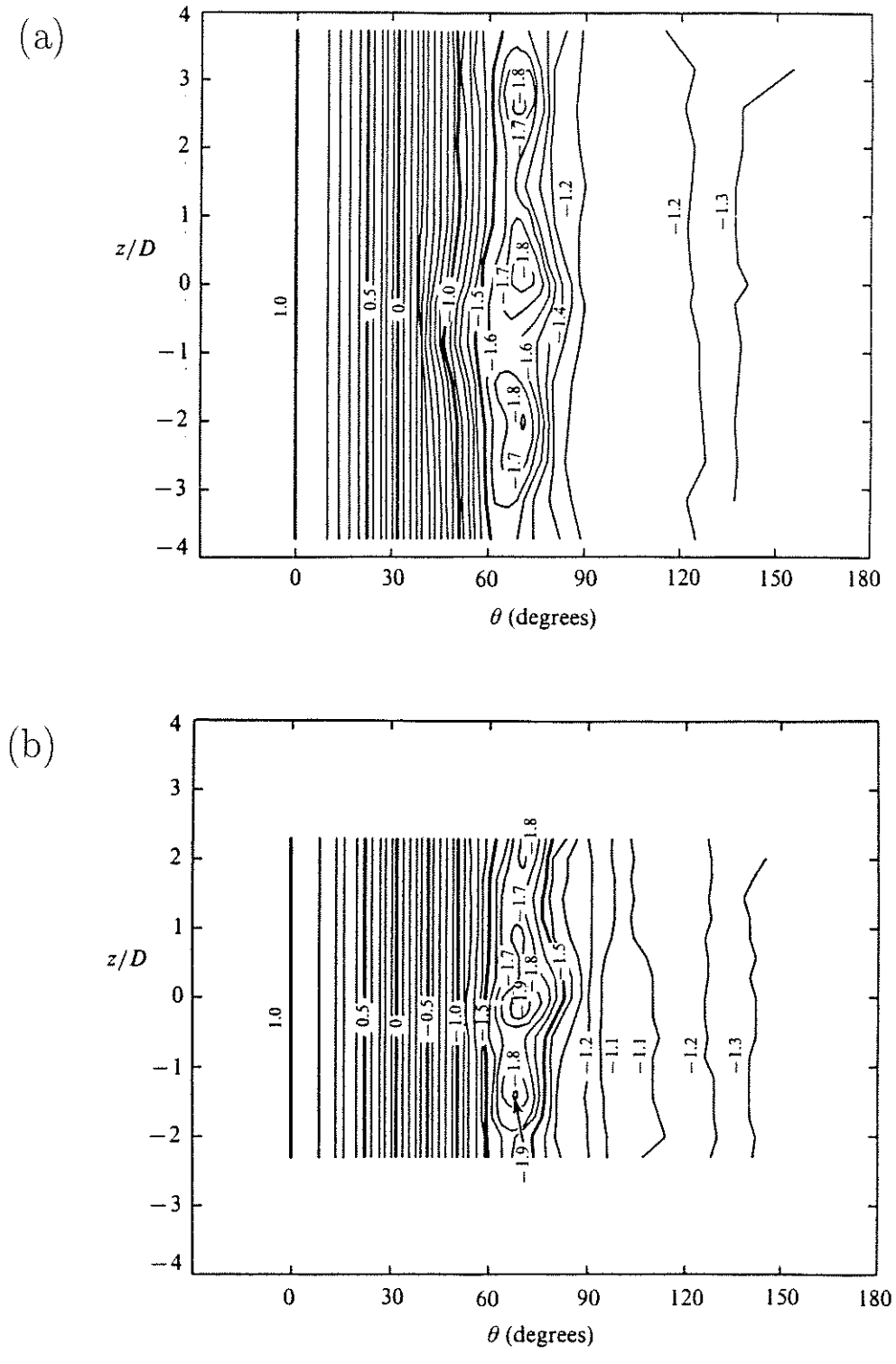

FIGURE 1.39: Constant pressure contours at (a) $Re = 1.95 \times 10^5$, AR = 8; (b) $Re = 1.9 \times 10^5$, AR = 5. z/D is distance in the spanwise direction. After Higuchi, Kim & Farell (1989).

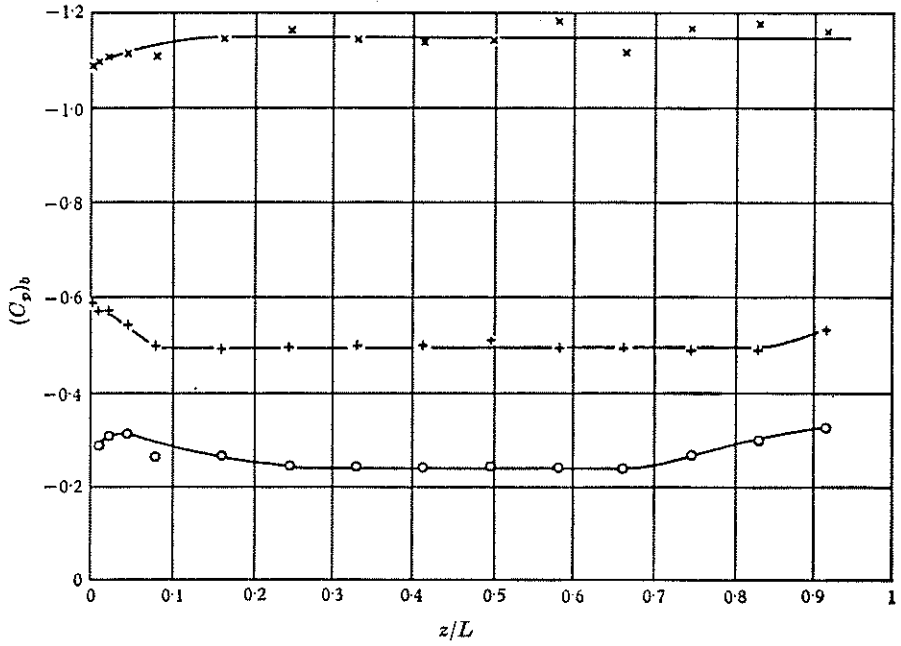

FIGURE 1.40: Variation of base pressure along span (z is distance from roof of tunnel and L is span) where: ×, $Re = 2 \times 10^5$; +, $Re = 3.68 \times 10^5$; ○, $Re = 4 \times 10^5$. After Bearman (1969).

projection of the plates from the cylinder centreline was reduced below $2.5\,D$.

If the end plates are too small in cross flow and downstream extent, they will not be able to prevent flow around the ends of the plates from interfering with the wake of the cylinder. This can be clearly seen in the flow visualizations presented by Kubo, Miyazaki and Kato (1989). Stansby's results also showed that plates of $7\,D$ cross flow dimension and projecting $4.5\,D$ downstream from the cylinder centreline reduced the end effects on the wakes of his cylinders (AR = 20:1 and AR = 10:1) in subcritical flow. End plates to Stansby's design ($2.5\,D$ upstream, $4.5\,D$ downstream and $7\,D$ cross flow) have by now almost become standard in tests on circular cylinders.

1.5.3 Measurements made in Smooth Flows

A selection of published measurements of σ_{C_l} for nominally smooth flows ($I_u < 0.6\%$) is presented in figure 1.41. The experimental details pertaining to the measurements are presented in table 1.2.

Subcritical Flow

The general characteristics of subcritical flow were discussed in § 1.3; the defining criterion is that the boundary layers are laminar at separation, leading to comparatively well-defined and strong vortices. As pointed out above, lift forces in nominally two-dimensional wind tunnel flows are sensitive to both cylinder aspect ratio and tunnel blockage, with low aspect ratio and high blockage both producing higher lift forces in subcritical flow.

TABLE 1.2: Experimental details for published measurements of lift made in nominally smooth flows.

Experiment		Measured	L_{active}/D	AR	Blockage%	I_u%
Keefe	1962	Force	1	18:1	2.3	0.3
Bishop & Hassan	1964 a	Force	3	6:1	8.4 ‡	?
Jones et al.	1969	Force	2.33	5.3:1	18.6 †	0.17
van Nunen	1972	Force	?	?	?	?
So & Savkar	1981	Force	3	8:1	16	0.5
Schewe	1983	Force	10	10:1	10 †	0.4
Cheung	1983	Force	6.7 (max)	3.6:1 (min) ¶	15 (max) ‡	0.4
Gerrard	1961	Pressure	—	6.7:1 (min) ¶	15 (max) ‡	0.3
Batham	1973	Pressure	—	6.7:1	5	0.5
Fox & West	1990	Pressure	—	10, 15, 25:1	5, 4	0.2

†Slotted tunnel walls ‡Blockage corrected ¶A number of different cylinders

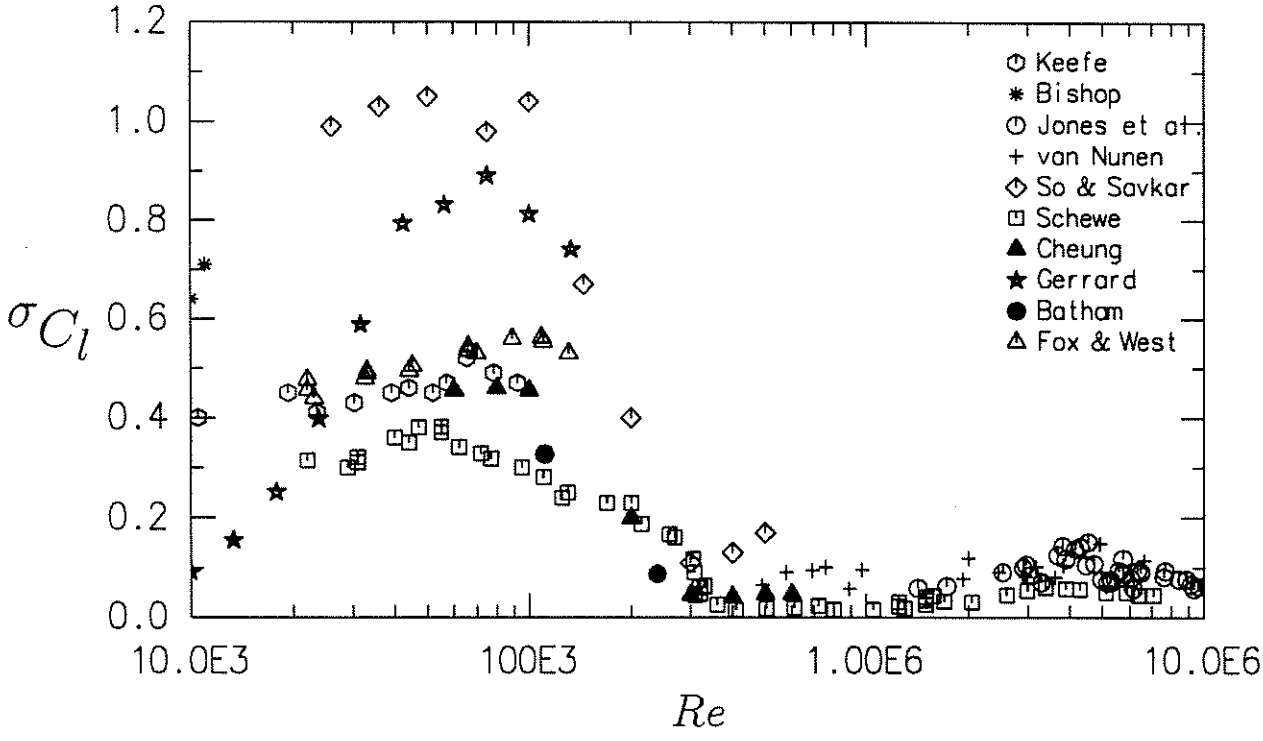

FIGURE 1.41: Published measurements of σ_{C_l} for nominally smooth flows.

The sets of results judged most reliable from the point of view of providing direct estimates of sectional σ_{C_l} appropriate to high aspect ratio cylinders in unconfined subcritical flows are those of Keefe (1962) and Fox and West (1990), both made on high aspect ratio cylinders with low tunnel blockage. Keefe's results, made using direct measurements of force on a 1 D long section of cylinder, are somewhat lower than those of Fox and West (1990), produced from pressure measurements, as would be expected.

The results of Gerrard (1961) were recorded using a number of cylinders of different blockage and aspect ratios, with the maximum blockages (15%) and lowest aspect ratios (6.7:1) coinciding with the highest Reynolds numbers. Gerrard estimated the value of σ_{C_l} using measurements of fluctuating pressures and the phase relationship of pressures around the cylinder (rather than the cross-correlation of pressures). The values of σ_{C_l} are seen to fall away very rapidly at low Reynolds number, faster than those of Keefe (1962) and Bishop and Hassan (1964 a). It may be that this is related to the lengthening of the vortex formation region (with consequently reduced lift forces), observed in the range of Reynolds numbers approximately $1 \times 10^3 < Re < 1 \times 10^4$ (see fig. 1.6). The limits on the range of Reynolds numbers over which this phenomenon occurs have not yet been precisely established, and it may be that Gerrard's values show influence of the effect, while those of Keefe and of Bishop and Hassan do not. Gerrard's maximum values of σ_{C_l} (0.85–0.9) are higher than the values of Keefe and of Fox and West (0.5–0.55 at $Re = 1 \times 10^5$). This is probably related to the high tunnel blockage of 15%. It is unclear from Gerrard's paper what, if any, blockage correction he used.

The results of Bishop and Hassan (1964 a) are at the low end of the Reynolds number range in figure 1.41 where it can be seen that their values of σ_{C_l} are rather high. Consideration of the flow configuration does not provide a explanation for this, since neither the tunnel blockage nor cylinder aspect ratio were extreme. Their results were corrected for blockage, using an empirical modification to the method of Allen and Vincenti (1944). This yielded a substantial correction, with an equivalent blockage ratio of 0.23 used to correct the dynamic pressure: the correction would have lowered the values of σ_{C_l} by a factor of ~1.3, placing their uncorrected results still higher. Bishop and Hassan reported a number of difficulties with their experimental apparatus.

Batham (1973) provided two measurements of $\sigma_{C_{l_{\text{local}}}}$ for a smooth cylinder in a low turbulence intensity flow. It can be seen that both are rather low when compared to the values of Keefe and of Fox and West in the subcritical regime and of Schewe in the precritical regime. This may indicate the early onset of the critical regime in his experiment; his "smooth" cylinder was in the "as machined" condition.

So and Savkar (1981) measured forces on sections of cylinders of various diameters which spanned a water tunnel of fixed diameter. The results for the lowest blockage ratio (16%) are presented here. Since the values presented are for a 3 D long section of cylinder, it is expected that values of $\sigma_{C_{l_{\text{local}}}}$ would be higher than those presented in figure 1.41. It is thought that their results are high due to large blockage and the circular working section of the water tunnel.

Cheung (1983, see also Cheung & Melbourne 1983) corrected his results for blockage, using an empirical method. On the basis that the results for subcritical flow ($Re < 1 \times 10^5$) were measured using the cylinder with the smaller diameter of the two cylinders

used for force measurements (8% blockage, 6.7:1 aspect ratio), the blockage correction applied amounts to $\sim 45\%$ of the measured values. This means that the uncorrected subcritical values of $\sigma_{C_{l_{\text{total}}}}$ would have been about 0.65. If the spanwise correlation length of vortex shedding were about $3.5\,D$ (as estimated from fig. 1.32), or about half the length of the cylinder, then the value read from figure 1.31 (0.75), provides an additional correction of factor, so that $\sigma_{C_{l_{\text{local}}}} \approx 0.65/0.75 = 0.87$.

The results produced by Schewe (1983) cover a wide range of Reynolds number and are thought to be of good quality, on the basis of his observations of the bi-stable single-bubble critical regime, and the very wide range of supercritical Reynolds numbers. His values of σ_{C_l} for the subcritical regime are lower than both those of Keefe and Fox and West, as expected from the fact that Schewe's measurements of lift force were made on the whole cylinder, $10\,D$ long. Using the compilation of spanwise correlation lengths published by Bruun and Davies (1975) (see fig. 1.32) and the correction factors of figure 1.31, Schewe's subcritical results become similar to those of Keefe and of Fox and West. It would be expected perhaps that his corrected results would be a little higher, since tunnel blockage would have raised the fluctuating forces, however the tunnel walls were slotted, which may have relieved the blockage to an extent.

Supercritical Flow

No details of the geometry of van Nunen's experiment are available, other than the cylinder diameter: 0.3 m. The measurements were obtained using the variable pressure NLR wind tunnel. In the range of Reynolds number under discussion, no periodicity was observed in the measurements of fluctuating force or surface pressures. Since no details of the equipment geometry are known, no comment can be made as to the relative correction between $\sigma_{C_{l_{\text{total}}}}$ and $\sigma_{C_{l_{\text{local}}}}$ which would be involved.

The values of $\sigma_{C_{l_{\text{total}}}}$ measured by So and Savkar would be larger if corrected to sectional values. In addition, the comparatively high blockage in their experiment, which was conducted using a circular working section, probably contributed to high values of RMS lift.

In this regime of Reynolds number, Cheung (1983) found that no blockage correction of results was required. This may have been due to the effectively lower blockage of the wake, since it is narrower in supercritical than in subcritical flows. The values of σ_{C_l} are lower than those presented here by a factor of about three, which is not easily accounted for by corrections based on figure 1.31. While Cheung presented values of Strouhal number for this regime in smooth and turbulent flows, the spectra from which the Strouhal numbers were obtained were normalized in the form $fS_{C_l}(f)/\sigma^2_{C_l}$ (Cheung 1990, private communication). This means that the Strouhal numbers may not have represented dominant spectral peaks if the spectra were normalized in the manner $S_{C_l}(f_r)/\sigma^2_{C_l}$.

Schewe's results for the supercritical regime have values of $\sigma_{C_{l_{\text{total}}}}$ lower than for the other sets of results presented. Also, Schewe's results indicate well-organized flow, with a very distinct spectral peak at $St = 0.48$ observed at Reynolds numbers of 4×10^5 and above.

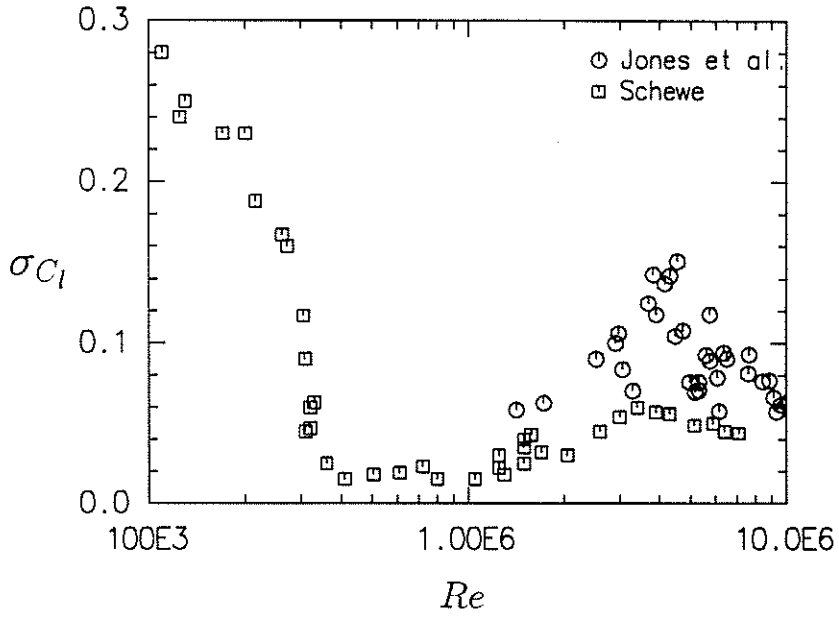

FIGURE 1.42: RMS coefficients of lift for the transcritical regime: results of Jones, Cincotta & Walker (1969) and Schewe (1983).

Transcritical Flow

Measurements of RMS coefficients of lift for smooth cylinders in the transcritical regime have been published by Jones, Cincotta and Walker (1969) and by Schewe (1983). Their results are presented for comparison in figure 1.42. In both experiments, forces were measured on finite lengths of cylinder, as described in table 1.41. Schewe measured force on a greater length of cylinder than did Jones, Cincotta and Walker, so his values of σ_{C_l} should be lower, other things equal. In the absence of measurements of correlation lengths in transcritical flow, reliable estimates of $\sigma_{C_{l_{\text{local}}}}$ cannot be derived from these results.

Probability Density of Lift Force

Probability distributions of lift force were presented by Schewe (1983) for both subcritical ($Re = 5.5 \times 10^4$) and transcritical ($Re = 7.1 \times 10^6$) flows. He also presented the third and fourth central moments of the probability distributions of lift force for all four flow regimes. In all cases, the values were similar to those for a Gaussian process, with slightly lower values of flatness (tending towards a distribution appropriate to e.g. a sinusoidal process) in the sub-, super- and transcritical regimes. Jones, Cincotta and Walker (1969) also presented results for the probability density of lift forces on a circular cylinder in the transcritical regime of Reynolds number. They found a greater deviation from a Gaussian distribution in the transcritical regime than did Schewe.

1.5.4 Influence of Surface Roughness

Cylinder surface roughness can have a profound effect on the flow past the cylinder. Since the scope of the present investigation does not extend to the effects of cylinder surface roughness, the discussion here will be brief. More detail is available in the review by Basu (1982), which provides references to the important experimental results in this area up to that date. Zdravkovich (1990) provides a discussion of the mechanisms by which surface roughness affects Reynolds number transitions.

It is observed that relative roughnesses ϵ/D greater than about 1×10^{-5} have the effect of triggering the critical transition at progressively lower Reynolds numbers, and of shortening the supercritical range. Sufficiently high relative roughnesses may be able to suppress the supercritical range entirely, with an immediate progression from subcritical flow (laminar boundary layer separation) to transcritical (turbulent). Roughness has this effect because it initiates boundary layer transition at lower cylinder Reynolds numbers.

At transcritical Reynolds numbers, for which the boundary layers are fully turbulent at separation, increasing the relative roughness tends to promote earlier separation and increase the coefficient of drag. The reason for this behaviour is not yet fully clear, but it is thought that increased surface roughnesses produce thicker boundary layers with larger momentum deficits, and that this means they are less able to remain attached to the cylinder in adverse pressure gradients (see Güven, Patel & Farell 1977 and Güven, Farell and Patel 1980). It is expected that fluctuating lift coefficients also increase with relative roughness in the transcritical range, again as the result of earlier separation. For example, the values of RMS lift coefficient measured at a section of roughened cylinders in transcritical flow by Szechenyi (1974, 1975) are approximately 0.27, which is much greater than the values for smooth cylinders shown in figure 1.42 (≈ 0.06), even accounting for the fact that spanwise correlation effects would have lowered the smooth cylinder values, since the measurements were conducted on finite lengths of cylinder.

Experimental results suggest that at each value of relative roughness, the flow past the cylinder becomes independent of Reynolds number at sufficiently high Re, as is the case for pipe flows. Szechenyi suggested that at sufficiently high values of relative roughness ($\epsilon/D > 1.5 \times 10^{-4}$), transcritical flow characteristics were dependent on the size of roughness and consequently on the roughness Reynolds number $U\epsilon/\nu$ alone, rather than the cylinder Reynolds number UD/ν in conjunction with the relative roughness ϵ/D. This hypothesis is not supported by later experimental results, for instance those of James, Paris and Malcolm (1980), Alemdaroğlu, Rebillat and Goethals (1980), and Buresti (1981).

The effect of relative roughness on correlation lengths in the sub-, super- and transcritical flow regimes on spanwise correlation is unclear, but it seems likely that surface roughness has the effect of increasing spanwise correlation lengths in the transcritical regime. As previously mentioned, measurements of spanwise correlation of flows in the supercritical and transcritical regimes are rare, partly as a consequence of generally low aspect ratios in wind tunnel studies for these regimes. Buresti (1981) measured correlation between signals from two hotwire anemometers located outside the wake flows past roughened cylinders and concluded that the spanwise correlation lengths varied from $3\,D$ in the subcritical regimes to $2\,D$ in the supercritical regimes through to $4\,D$ in the

transcritical regimes. No dependence on relative roughness was noted. The results of Szechenyi suggested that the spanwise correlation lengths in his experiment were more of the order of $9\,D$ for two independent (but unidentified) relative roughnesses.

1.5.5 Influence of Turbulence

Turbulence always originates from instabilities which exist in regions of sheared flow. Only the aspects which are most relevant to flows around bluff bodies and circular cylinders in particular are dealt with here.

From a wind engineering perspective, the flows in which real structures are usually situated are boundary layer flows, with significant shear which produces non-uniformity of mean and turbulent flow properties over the length of the structure. In boundary layer wind tunnels one of the primary modelling tasks is to correctly represent a scaled model of the full size flow, but in tests on nominally two-dimensional bluff bodies it is more convenient and usual to use grid-generated turbulence. Grid-generated turbulence can be nearly homogeneous and isotropic over the scale of the cross-section of the two-dimensional model under test. The extent to which bluff body flows in grid-generated turbulence approximate those in correctly scaled shear flows is not clear, partly because both are poorly understood. For slender structures, there is some justification for the use of homogeneous turbulence at least, on the basis that in full scale the turbulence properties do not vary rapidly on the scale of the typical vortex-shedding flow structures involved (of the order of a few diameters).

Turbulence Intensity and Scale

At high enough Reynolds numbers (based on the RMS magnitude of the velocity fluctuations and turbulence integral scale), the energy containing portion of grid-generated turbulence is assumed self-similar over a range of flow speeds (Tennekes & Lumley 1972, ch. 8). This means that the spectra of turbulent fluctuations, excluding the dissipation range, can be represented by a common dimensionless form for all Reynolds numbers. The theoretical form of the spectrum for grid-generated turbulence (or even homogeneous isotropic turbulence) is unknown, but a representation often used is that due to von Kármán (1948), which can be put into frequency-dependent form using Taylor's hypothesis (Simiu and Scanlan 1986)

$$\frac{f S_u(f)}{\sigma_u^2} = \frac{4\frac{f L_u^x}{U}}{\left[1 + 70.8\left(\frac{f L_u^x}{U}\right)^2\right]^{5/6}} . \tag{1.11}$$

It follows that grid-generated turbulence can be characterized by the length scale L_u^x and by its intensity $I_u = \sigma_u / U$.

There is not yet enough experimental or theoretical evidence to fully explain the effects of the two variables, L_u^x and I_u, on flows around bluff bodies. The complications are greater in the case of flows around circular cylinders than for sharp-edged shapes, because various instability phenomena result in many transitions in the flow as Reynolds number changes. Turbulence often affects these transition phenomena, bringing them

about at lower Reynolds numbers (although the addition of turbulence does not in general have the same effect as an increase in Reynolds number). Consequently it is often difficult to differentiate effects caused by the transition-promoting effects of turbulence from those which might be produced in otherwise Reynolds-independent flow regimes.

In an attempt to relate the transition point in flat plate boundary layers to the turbulence properties of the external flow Taylor (1936)[6] proposed that the transition point is some function of the parameter $Ta = I_u(L_u^x/D)^{-1/5}$. This parameter (the Taylor parameter) has become the model for various forms of turbulence parameters which try to characterize the effects of turbulence and scale in one variable, typically of the form $I_u(L_u^x/D)^n$. As Bearman and Morel (1983) point out, there is no theoretical basis for the use of the Taylor parameter in *separated* flows. While the use of the parameter has been extended to correlate the effects of turbulence on the critical transition in flows around spheres and circular cylinders (Taylor 1936, Bearman 1968 a Kiya et al. 1982—see equation (1.1)), Bearman and Morel conclude that the correlating effect is merely coincidental. They argue that the ability of the parameter to correlate the critical transition just reflects the fact that the negative exponent in the parameter emphasizes the importance of small scale turbulence in triggering the transition phenomenon. The critical transition on spheres and cylinders is brought about by turbulent reattachment of separated shear layers, in turn due to the increased entrainment rate of turbulent shear layers. Increasing the Reynolds number in smooth flow moves the turbulent transition point in the free shear layers closer and closer to the separation point; eventually the turbulent shear layers, unable to entrain sufficient fluid from the slow backflow region near separation, reattach to the cylinder before final turbulent separation. The addition of fine scale turbulence either brings about earlier transition in the free shear layers or increases their entrainment rate, thus promoting the critical transition at lower Reynolds numbers.

According to Bearman and Morel, there are three main ways in which turbulence interacts with the mean flow around bluff bodies. They are:

1. Transition effects, for example the earlier transition of laminar shear layers to turbulence produced by turbulent fluctuations in the upstream flow.

2. Mixing effects, for example enhanced entrainment into turbulent shear layers produced by the addition of turbulence to the upstream flow.

3. Distortion effects caused by the interaction of the mean flow around the body with turbulence, bringing about attenuation or amplification of different components depending on their scales.

The interaction with fluctuating flow is less easily categorized (partly because the fluctuating flow is less well understood than the mean), but an immediate addition to the list above is

4. Quasi-steady effects, where slowly fluctuating loads are produced by low frequency fluctuations in the flow which do not affect the short-time-average force coefficients.

[6] See also Goldstein 1965, pp. 327–329.

At a slightly more complicated level, another addition could be made:

5. Correlation effects, where (for instance) the correlation length of load is reduced by the influence of turbulence scales of a similar size.

The mixing effect of additional turbulence produces an increase in turbulent boundary layer local skin friction coefficients (Bearman & Morel 1983), due to an increase in turbulent momentum transfer. The effect on already turbulent boundary layers should be to thicken them, giving greater momentum deficits at any given Reynolds number. In this respect the addition of turbulence could be thought of as being similar to an increase in surface roughness, but the comparison is not straightforward. This is because rough surfaces on objects immersed in the fluid can become hydrodynamically smooth once the depth of the linear sublayer becomes greater than the roughness height (Schlichting 1979 p. 652); such an effect probably does not occur for additional turbulent momentum transfer caused by free stream turbulence. In addition, homogeneous isotropic turbulence is described by two parameters, integral length scale and intensity, while the effects of surface roughness are more nearly a function of one parameter, the relative size of the roughness elements ϵ/D.

The relationship between turbulence scale and vortex shedding frequencies can be illustrated by plotting turbulence spectra in terms of reduced frequency f_r, with the aid of equation 1.11. This enables a comparison of the frequency contents of turbulence and vortex shedding forces. Von Kármán's spectral function can be written in terms of the reduced frequency variable f_r

$$\frac{S_u(f_r)}{\sigma_u^2} = \frac{C_1}{\left[1 + 70.8\left(\frac{L_u^x}{D}\right)^2 f_r^2\right]^{5/6}} . \tag{1.12}$$

Spectra of this form are plotted in figure 1.43 for various values of the length scale ratio LSR $= L_u^x/D$. The plots are normalized such that the area under each curve is the same (corresponding to a constant turbulence intensity). For comparative purposes, a representative lift force spectrum is also plotted on the figure. This is of the form

$$S_l(f_r) = C_2 \exp\left[-\left(\frac{f_r - St}{B\,St}\right)^2\right] . \tag{1.13}$$

For this plot, representative values of the Bandwidth parameter $B = 0.07$ and the Strouhal number $St = 0.2$ were used, which correspond to subcritical narrow-band vortex shedding (Vickery & Clark 1972).

It is likely that only frequencies of the order of the vortex shedding frequency and higher by perhaps a few orders of magnitude have any significant direct effect on vortex shedding forces (in effect, this amounts to a judgement as to where the division between direct and quasi-steady effects lies). On the basis of the figure it might be expected that for length scale ratios of perhaps 20:1 or greater, turbulence will produce mainly quasi-steady loads on the structure, while the fine-scale turbulence at the high wavenumber end of the spectrum may still affect Reynolds number transitions.

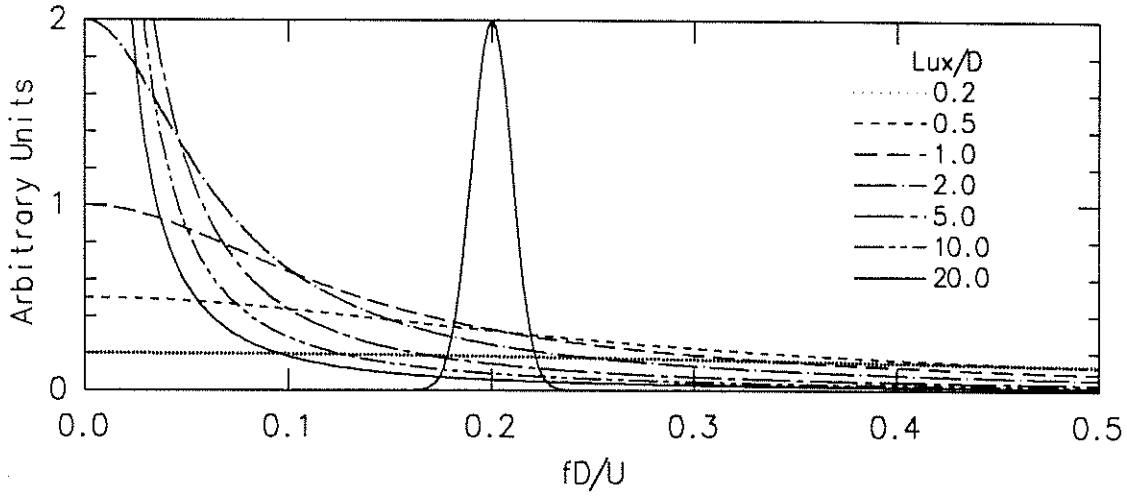

FIGURE 1.43: Spectra of turbulence and lift due to vortex shedding, plotted on a common frequency axis, showing the influence of turbulence integral scale. The vertical units of measure are arbitrary, but the turbulence spectra are normalized to the same variance.

Typical length scale ratios in full scale are of the order of 10:1 and greater, while those in wind tunnel experiments using grid-generated turbulence are typically of the order of 5:1 and less.

Effects of turbulence on flows past sharp-edged bodies Before moving on to discuss flows around circular cylinders in more detail, it will be interesting to examine some results for flows around sharp edged bodies, where the transition effect of turbulence should be less significant.

Bearman's (1971) finding that free-stream turbulence with intensities up to 10% had little or no effect on the base pressure or drag of two-dimensional thin flat plates suggests that turbulence does not substantially affect the mean processes in wakes, since the separation points in this case are fixed and there is no possibility of flow reattachment having influenced the results.

Vickery's (1966) results for a two-dimensional square section prism at different angles of attack suggest the same thing, since near an angle of attack $\alpha = 45°$ addition of flow turbulence ($I_u = 10\%$, LSR = 1.3) produced almost no change in base pressure coefficient (fig. 1.44). At the 45° angle of attack, there is little possibility of reattachment, hence the separation points again were known to be at the shoulders of the shape (at lower α the higher base pressures in turbulence are due to reattachment).

These results are supported by measurements of fluctuating sectional forces obtained by Vickery and by Lee (1975). Both results for normal force coefficients are shown in figure 1.45. Lee's measurements become effectively independent of turbulence intensity at $\alpha = 45°$, although the more turbulent flows have slightly greater fluctuating forces. The same effects are seen in Vickery's results. At the 45° angle of attack, slightly higher fluctuating forces are to be expected in more turbulent flows due to the body-coordinate measuring system used in each experiment, which has the effect that along flow (drag) buffeting contributes to the total fluctuating forces. (The differences in level between

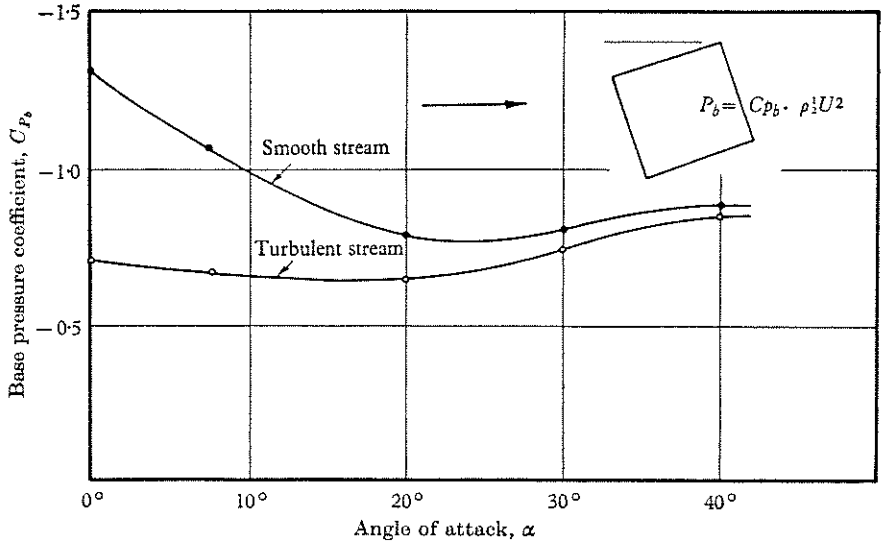

FIGURE 1.44: Base pressure coefficient C_{pb} as a function of angle of attack α for a square section prism (after Vickery 1966).

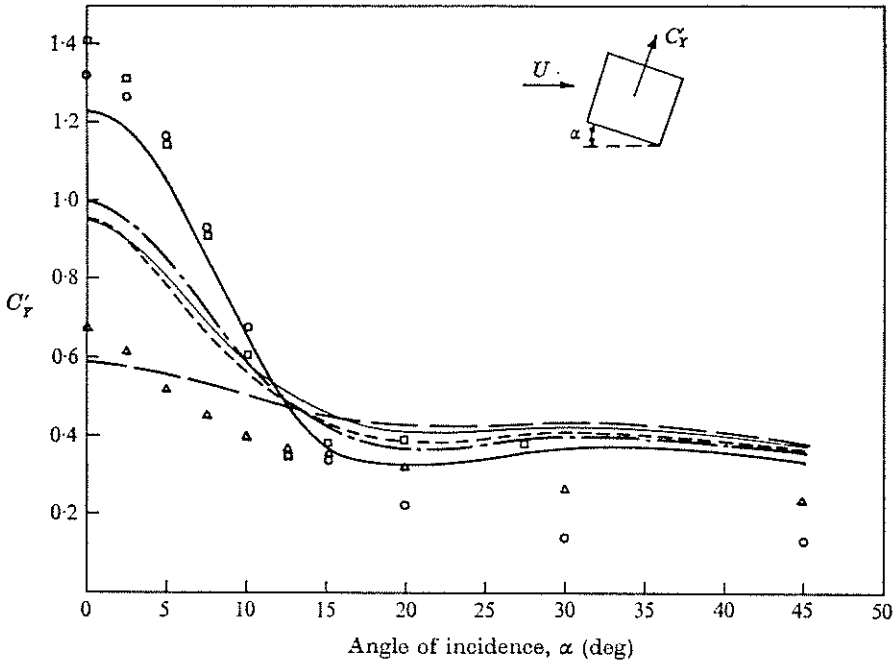

FIGURE 1.45: Coefficient of fluctuating normal force C'_Y with angle of incidence α (after Lee 1975).

Vickery's and Lee's experiments are unexplained, but may be due to the amount of tunnel blockage and blockage correction which differed between the two.)

Effects of Turbulence on Reynolds Number Transitions

Zdravkovich (1990), in his review of transition regimes in the flow past a circular cylinder, takes the view that it is mainly the turbulence intensity, rather than scale, which influences the transition states (table 1.3.4), with the different states being differently

affected.

The "precritical" state TrS0 is brought on at lower Reynolds number, but the mechanism is not clear. If the precritical state is indeed due to creation of laminar separation bubbles, as suggested by the work of Higuchi, Kim and Farell (1989), then it is possible that they are directly affected by interaction with turbulence structures of about the same scale. This may mean that turbulence of either very large or very small scales may not affect the phenomenon.

Turbulence has great effect on the various critical regimes TrS1–TrS3. These regimes, with their associated laminar-turbulent separation bubbles, are very sensitive to disturbances in smooth flow, partly on the evidence that a wide variety of flow parameters such as Strouhal number and coefficient of drag have been published for this regime. In some flows, for example those of Bearman (1969) and Schewe (1983), evidence of stable separation bubbles was found over a range of Reynolds numbers, with associated high frequency vortex shedding, however in many experimental results no clear Strouhal number is found in the supercritical regime. In most of the experiments with high intensity turbulence and with Reynolds numbers in the range $1 \times 10^5 < Re < 1 \times 10^6$, no evidence of coherent vortex shedding and an associated Strouhal number has been found. Only in the work of Cheung (1983) were Strouhal numbers presented, but no spectra of fluctuating pressures and forces were provided, as discussed in § 1.5.3. Spectra of lift forces in turbulent flow were presented by So and Savkar (1981); these show no evidence of spectral peaks.

Zdravkovich conjectures that at high levels of turbulence intensity, no regimes of flow for which separation bubbles exist will occur, and that transition will be made directly from subcritical flow (with laminar boundary layer separation) to transcritical flow (turbulent):

> At still higher I_u, the fragmented separation bubbles are also destroyed. It is expected that the extent of the supercritical regime will gradually shrink until it eventually disappears. The latter has not yet been corroborated by experiments. If this happens then vortex shedding does not cease at all and the precritical regime is succeeded by the transcritical regime TrBL4.

Quasi-steady Effects

For a cylinder in a flow with LSR, the turbulent fluctuations will appear to the cylinder like a slow variation in the speed and direction of the mean flow. This because, as pointed out above, there will be little turbulent energy at the frequencies comparable to the vortex shedding frequency. In this case the loads can be thought of as *quasi-steady*, meaning that the local force coefficients, averaged over a short time interval, are the same as in a steady smooth flow of the same Reynolds number. By "a short time" is meant some small number of vortex shedding periods.

Quasi-steady variations are thought to have two effects on the cross flow forces on stationary cylinders: (i) broadening of the spectra of sectional lift forces, due to fluctuations in the speed of the flow, and (ii) producing low-frequency buffeting (drag) loads in the average cross flow direction due to fluctuations in direction of the flow.

These effects have been discussed by Vickery and Clark (1972), Davenport (1979), and Basu 1982).

Spectral Bandwidth It has been found that the spectra of vortex shedding forces in subcritical flow can be represented reasonably well by the formula (Vickery & Clark 1972)

$$\frac{f\,S_{C_l}(f)}{\sigma_{C_l}^2} = \frac{f}{\sqrt{\pi}\,B\,f_s}\exp\left[-\left(\frac{1-f/f_s}{B}\right)^2\right] . \tag{1.14}$$

Here, f_s is the vortex shedding frequency and B is an empirical bandwidth parameter, of order 0.06 in smooth flow (Vickery & Clark 1972). An equivalent form is

$$\frac{S_{C_l}(f_r)}{\sigma_{C_l}^2} = \frac{1}{\sqrt{\pi}\,B\,St}\exp\left[-\left(\frac{f_r-St}{B\,St}\right)^2\right] . \tag{1.15}$$

If the lift were sinusoidal in smooth flow, and turbulence had only a quasi-steady effect, then $B = \sqrt{2}I_u$ in turbulence (Davenport 1979, Basu 1982). To account for this, while allowing a finite bandwidth B_0 in smooth flow, Basu suggested that $B^2 \approx B_0^2 + 2I_u^2$.

The action of the quasi-steady variation of flow speed is thus to broaden the spectra of vortex shedding forces while preserving their variance.

Buffeting Forces Buffeting forces are associated with the lateral component of turbulence. To the extent that they can be isolated by quasi-steady assumptions, they may be considered a separate component of cross flow force to that created by vortex shedding. In turbulent flows, the cross flow response of slender cylindrical structures may be dominated by response to buffeting forces, particularly at high reduced velocities, where the wind speeds exceed the critical speeds of the first few vibration modes.

Cross flow buffeting is due to the cross flow component of turbulent velocity fluctuations (v). The quasi-steady fluctuating force per unit length σ_l is given by (Davenport 1979)

$$\sigma_l = \frac{1}{2}\rho\sigma_v U\left(\frac{\partial C_l}{\partial\alpha} + C_d\right) D . \tag{1.16}$$

In general, for a circular cylinder $\partial C_l/\partial\alpha = 0$, so the induced lift coefficient C_{li} is

$$C_{li} = I_v C_d , \tag{1.17}$$

where I_v is the lateral turbulence intensity σ_v/U.

Cross flow buffeting will produce cross flow forces at frequencies (by quasi-steady assumption) well below the vortex shedding frequency. Their magnitude will increase with turbulence intensity, and with wind speed, to the point that cross-flow response may be dominated by buffeting once the critical wind speed has been exceeded. Under the assumptions that lift force may be decomposed into uncorrelated components due

to vortex shedding and cross-flow buffeting and that buffeting lift force spectral density is linearly related to the spectral density of cross-flow turbulent velocity fluctuations over the frequency range (as implied by equation (1.17)), one finds that

$$\sigma^2_{C_{l\text{turb}}} = \frac{S_{C_l}(f_r)_0}{4\ \text{LSR}}\ , \tag{1.18}$$

where $S_{C_l}(f_r)_0$ is the zero-frequency value of the spectral density of lift coefficient when the frequency scale f_r is dimensionless[7]. Evidence of cross flow buffeting may be seen in the full-scale results discussed at the end of this section.

1.5.6 Measurements made in Turbulent Flows

As pointed out above, the study of turbulence effects on the flow around circular cylinders is complicated by the fact that instability effects associated with Reynolds number changes are in general promoted by the addition of turbulence to the flow. This complication is evident in the following discussion of experimental results obtained in wind tunnels.

Wind Tunnel Results

Surry (1972) presented results for the influence of turbulence on the flow around a circular cylinder (AR = 39:1, Blockage 4%) at subcritical Reynolds numbers. Two turbulence LSRs (4.0 & 0.36) and two turbulence intensities ($I_u \approx 10\%$ & 14.5%) were used, besides a nominally smooth ($I_u = 2.5\%$) flow.

Surry states that ordering the effect of turbulence on the mean flow in terms of the Taylor parameter seemed logical in the sense that higher Ta flows had later separation. However, none of the flows can be judged post-critical, because well-defined vortex shedding with $St \approx 0.2$ was always present. The highest intensity, smallest scale flow is critical, according to equation (1.1).

Fluctuating lift and drag values were presented only for the largest intensity large scale flow but information about fluctuating pressures was given for all the flows. The main effect of the larger scale flows on the spectra of pressure fluctuations at $\theta = 150°$ was to slightly broaden and lower the spectral peak at the Strouhal frequency, while low frequency energy increased. In the smaller scale (highest Ta) flow, the sharpness of the spectral peak was little affected, but the magnitude was lowered and the frequency shifted to a larger value; these facts reflect the delayed separation in that case.

The azimuthal distribution of RMS pressures showed that near the stagnation region, the magnitude of the fluctuations directly reflected I_u, with little effect of scale. The delayed separation for the small scale case was reflected in the fluctuating pressure

[7]This result stems from the fact that

$$\int_0^\infty \left[1 + 70.8\left(\frac{L^x_u}{D}\right)^2 f_r^2\right]^{-5/6} df_r = \frac{1}{4L^x_u/D}\ .$$

distributions. Fluctuating pressures in the wake region showed reasonable similarity to the nominally smooth flow case, reflecting the overall similarity in the mean distributions, while the fluctuations upstream of separation became increasingly dominated by turbulent fluctuations as I_u increased.

Surry's RMS lift and drag forces were presented for the largest scale and intensity combination, and compared with the smooth flow results of Keefe (1962). The fluctuating lift coefficient was much the same as Keefe's, while the fluctuating drag was higher (although as Farell 1981 noted, Keefe's σ_{C_d} value was too low by a factor of about three—which still leaves Surry's result about twice as large as the corrected result of Keefe). The second harmonic of the Strouhal frequency was not discernible in Surry's cross-spectra of drag force, indicating that the fluctuating drag loads were dominated by turbulent buffeting. Cross-spectra of lift force displayed most of their energy at the Strouhal frequency, with substantial axial correlation of lift.

Surry's results for narrow-band correlations of pressure fluctuations near the Strouhal frequency showed that the addition of turbulence of LSR=4.0 produced a greater drop in correlation length ($\Lambda \sim 6 \rightarrow\sim 4.5$) than did the smaller scale ($\Lambda \sim 6 \rightarrow\sim 5$), which possibly indicates that the smaller scale turbulence was less disruptive of the spanwise coherence of vortex shedding.

Bruun and Davies (1975) carried out experiments on a smooth circular cylinder in the subcritical–supercritical range of Reynolds numbers ($8 \times 10^4 < Re < 4.8 \times 10^5$) with the aim of studying the relationship between the parameters of turbulence in the approaching air and the fluctuating pressures on the cylinder. No measurements of fluctuating lift and drag were presented.

For three of the four of their turbulent flow cases, turbulence of $I_u \approx 11\%$ was used, at two length scale ratios LSR = 0.55 and 0.19. The other turbulent flow case had smaller intensity ($I_u = 3.8\%$), LSR = 0.35, and with $Re = 8 \times 10^4$, was just subcritical on the basis of the correlation of Kiya et al. (equation 1.1).

Bruun and Davies found that the addition of turbulence in supercritical flows produced pressure fluctuations over the front (0°–30°) part of the cylinder which were nearly linearly related to the turbulence intensity, while fluctuating pressures in the wake region were little affected by turbulence.

The spectra of pressure fluctuations at different angular positions around the cylinder were presented only for sub- and supercritical smooth flows. In the subcritical flow, energy at the Strouhal frequency dominated the spectra from the front part of the cylinder, while second and third harmonics started to appear at the 90° position. In supercritical flow, low frequency energy dominated the spectra, with a small spike at $St = 0.33$ over the rear of the cylinder. No spectral peaks were observed in turbulent supercritical flow.

Spanwise correlation in the supercritical turbulent flows was found to vary with the scale of turbulence over the front part of the cylinder, but over the rear of the cylinder the length scales were little influenced by the turbulence, indicating that the scales of the wake flow structures were more or less independent of the turbulence.

Norberg (1986) investigated the fluctuating pressure field of a smooth circular cylinder for turbulent flows with low intensities ($I_u < 4.1\%$) and small scales ($L_u^x/D < 0.3$).

The Reynolds numbers $Re < 6 \times 10^4$, were subcritical on the basis of equation (1.1). An interesting and seemingly anomalous feature was that although the mean and fluctuating pressure fields showed evidence of separation bubbles, the Strouhal number remained near 0.2, and the coefficients of lift and drag were little affected, compared with the smooth flow case. Presumably this behaviour is evidence of the precritical transition regime, where laminar separation bubbles have were observed by Higuchi, Kim and Farell (1989), as discussed in § 1.3.

Batham (1973) conducted experiments with cylinders that had smooth ("as machined") and rough ($\epsilon/D = 2.2 \times 10^{-3}$) surfaces at two Reynolds numbers ($Re_1 = 1.11 \times 10^5$ & $Re_2 = 2.37 \times 10^5$) and for two turbulence conditions ($I_u = 0.5\%$ & $I_u = 12.9\%$, LSR = 0.5). The results are significant for the study of the effects of turbulence on high Reynolds number flows because for the rough cylinder, boundary layer separation was turbulent, as it is for transcritical flows on smooth cylinders. Measurements presented were of mean and fluctuating pressures, and of fluctuating lift and drag at a section of the cylinder.

In smooth flow, the smooth cylinder exhibited vortex shedding at both Reynolds numbers, on the evidence of the spectra obtained from pressure transducer signals. When turbulence was added to the flow, vortex shedding was suppressed for the smooth cylinder, with separation occurring at about 120° from the front of the cylinder. The fluctuating pressures on the front of the cylinders appear to have been dominated by the incident turbulence, since the level of fluctuating pressures were very similar at the front generator of the cylinder for both the smooth and the rough cylinder. Also, the axial correlation lengths of the pressure fluctuations along the front of the cylinder were similar to that of the turbulence in the turbulent, but not the smooth flows. For the smooth cylinder, the axial correlation lengths were relatively constant at about $0.5\,D$ (the same as the LSR) for all angular positions in the turbulent flows.

The rough cylinder exhibited vortex shedding in smooth flow at both Reynolds numbers, but with more strength at Re_2. Strouhal numbers were 0.18 and 0.23. Axial length scales of pressure fluctuations (taken as averages over the range $\theta = 60°$–$150°$) were also higher at Re_2, $\sim 3.2\,D$ as opposed to $\sim 1.5\,D$ at Re_1.

At Re_2, addition of turbulence to the flow past the rough cylinder did not appear to broaden the spectral peak of pressure fluctuations at the $\theta = 120°$ position. The magnitude of pressure fluctuations at the peak increased with the addition of turbulence, and the sectional coefficient of lift rose too, from 0.15 to 0.27. Axial length scales of pressure fluctuations (over the angular range above) dropped a little at Re_2 with the addition of turbulence, from $\sim 3.2\,D$ to $\sim 2.3\,D$. At Re_1 vortex shedding was not as well established as at Re_2, as indicated by the smaller coefficient of lift and the smaller axial correlation of the pressure fluctuations.

The addition of turbulence to the flow about the rough cylinder at Re_2 moved the separation point forward from about 92° to 86°. This gives an indication that the addition of turbulence with integral scales of the order of the cylinder diameter to a transcritical flow (with turbulent boundary layer separation) may promote earlier separation, however some caution is required since Reynolds number independence was not reached in smooth flow.

So and Savkar (1981) conducted measurements of fluctuating lift in turbulent flow,

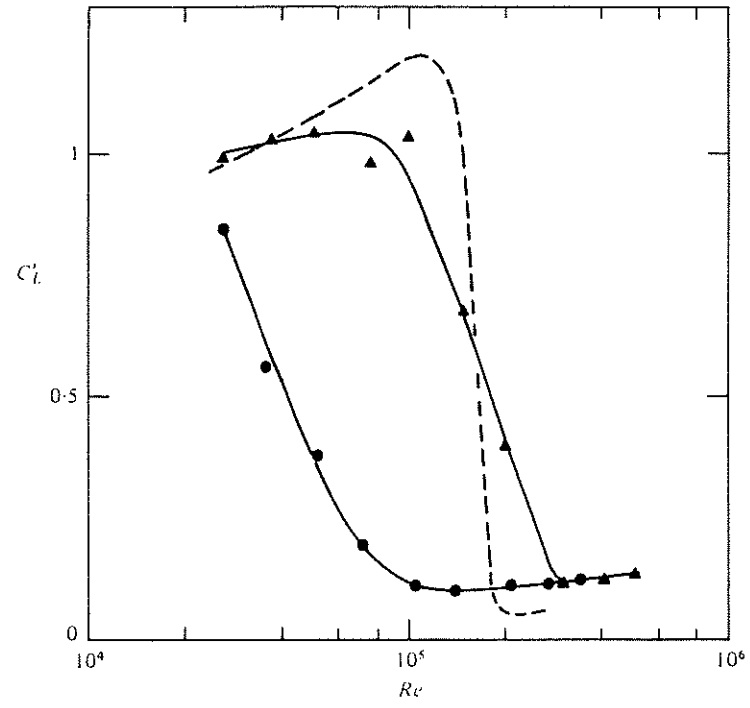

FIGURE 1.46: Measurements of RMS lift made by So & Savkar (1981) in turbulent flow with $I_u = 9.5\%$, LSR = 0.8.

in addition to measurements in smooth flow discussed in § 1.5.3. The results presented here (fig. 1.46) are for the same cylinder configuration detailed in table 1.41. The grid-generated turbulence had intensity $I_u = 9.5\%$ and integral scale LSR ≈ 0.8. So and Savkar found no evidence of a distinct spectral peak at Reynolds numbers greater than 1.4×10^5 (their spectra were normalized in the form $S_l(f_r)/\sigma_l^2$).

Turbulent flow measurements of $\sigma_{C_{l_{\text{total}}}}$ for a range of turbulence intensities were published by Cheung (1983, Cheung & Melbourne 1983); again, the main experimental parameters are presented in table 1.41. The measurements of fluctuating lift (fig. 1.47) were corrected for the effects of tunnel blockage, giving reductions in values of σ_{C_l}, with greater reductions in low turbulence, low Reynolds number flows. No correction was applied to the highest turbulence intensity flow ($I_u = 9.1\%$) for Reynolds numbers greater than 2×10^5. The LSR for all turbulence intensities greater than 0.4% was about 0.5. While Cheung's results cover a greater range of turbulence intensities and Reynolds numbers than previous work, no spectra of lift forces were presented. Strouhal numbers were given, but the manner in which the lift force spectra were normalized leaves some doubt as to whether these values represent true spectral peaks, as discussed in § 1.5.3.

Because of the uncertainty associated with conversion of $\sigma_{C_{l_{\text{total}}}}$ to values of $\sigma_{C_{l_{\text{local}}}}$ in the supercritical regime and in turbulent flow, no attempt will be made to provide estimates of $\sigma_{C_{l_{\text{local}}}}$ from the results of So and Savkar and Cheung. However, it can be assumed that the numerical values of their results would be higher if converted to values of $\sigma_{C_{l_{\text{local}}}}$.

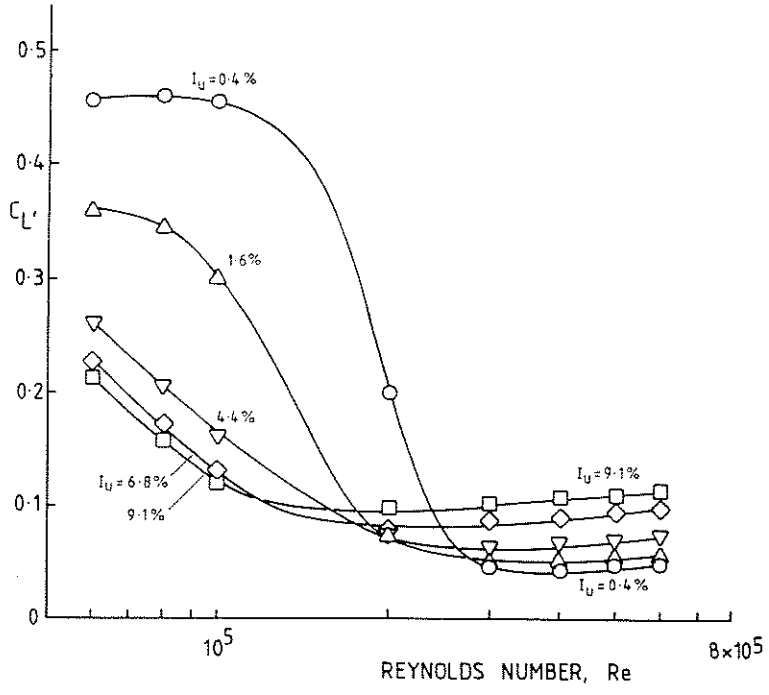

FIGURE 1.47: Measurements of RMS lift obtained by Cheung (1983) in turbulent flows (with blockage correction).

Full Scale Results

Full scale measurements of fluctuating lift in high Reynolds number ($Re > 10^6$) flows are naturally of prime importance to the designer. All wind tunnel tests to date in this Reynolds number range have been made in smooth flow, while the full scale data have all been obtained in turbulent flow. The ratios of turbulence scale to cylinder diameter, although often not measured, are at least of the order of magnitude appropriate to other similar structures. The effects of the three-dimensionality of the flow (due to wind shear, taper, free ends of the structures and irregularities of shape) are usually unknown and hard to assess. This is of some importance for the direct incorporation of such measurements into design methods, since the starting point of the methods are measurements made in nominally two-dimensional conditions, with correction subsequently made for such effects. Finally, the surface roughness of the particular structure involved must be bourne in mind, since this has an effect on the characteristics of the flow in the transcritical regime.

Measurements made on full scale structures for which spectra of lift were obtained are the focus of attention here. Three published sets of results are those of Ruscheweyh and Hirsch (1975), Hansen (1980) and Sanada and Nakamura (1983), all carried out on concrete structures which are shown here in figure 1.48.

Ruscheweyh and Hirsch's measurements were carried out on the lower shaft of the Hamburg television tower, which was surrounded by city terrain with an average building height of 20 m. At the level of the measurements, this would provide a typical integral scale of turbulence of about 100 m, giving $L_u^x/D \sim 10$. The turbulence intensity was 15.1%. The surface roughness of the structure was $\epsilon/D = 3.7 \times 10^{-4}$; the

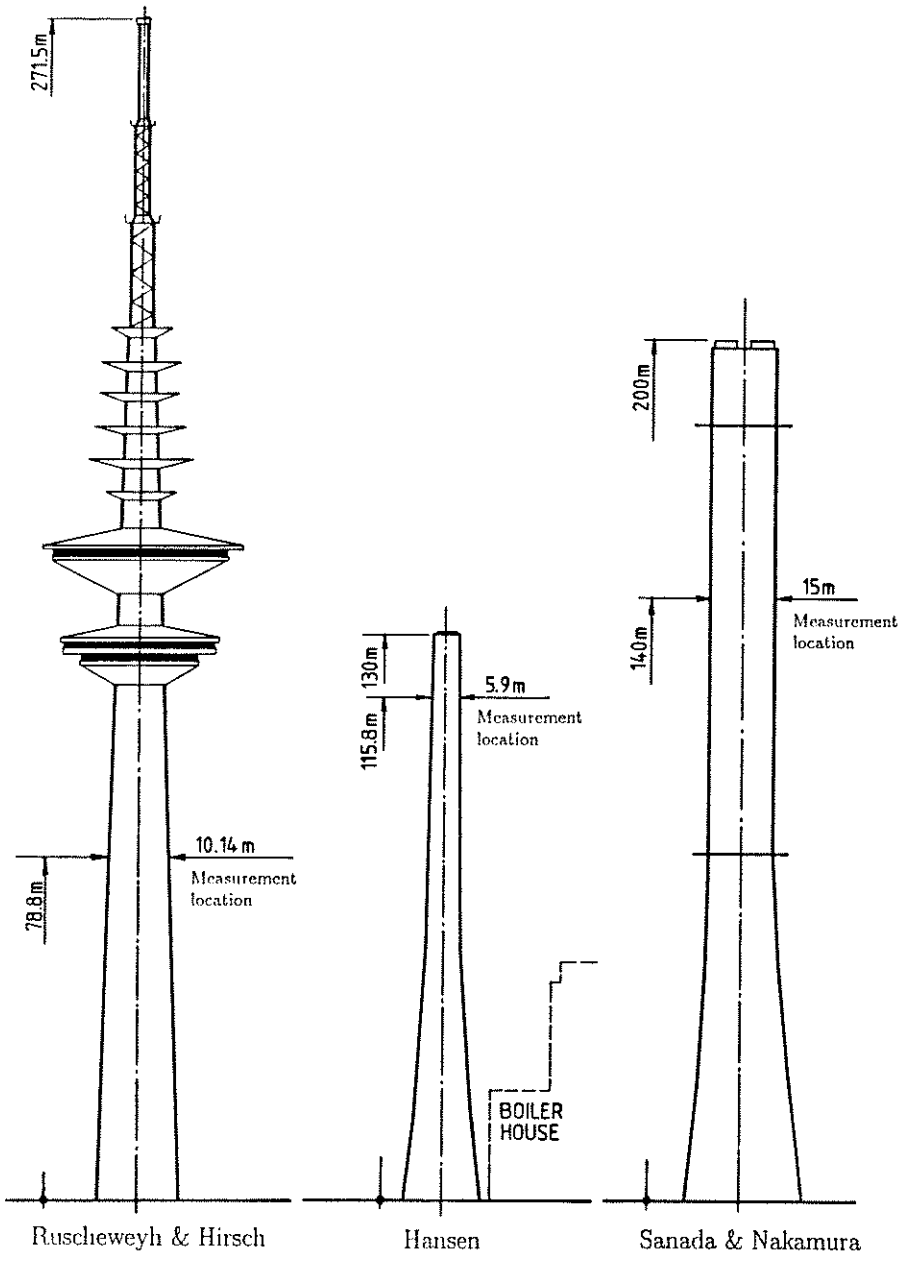

FIGURE 1.48: Concrete tower & chimney stacks used for full-scale measurements.

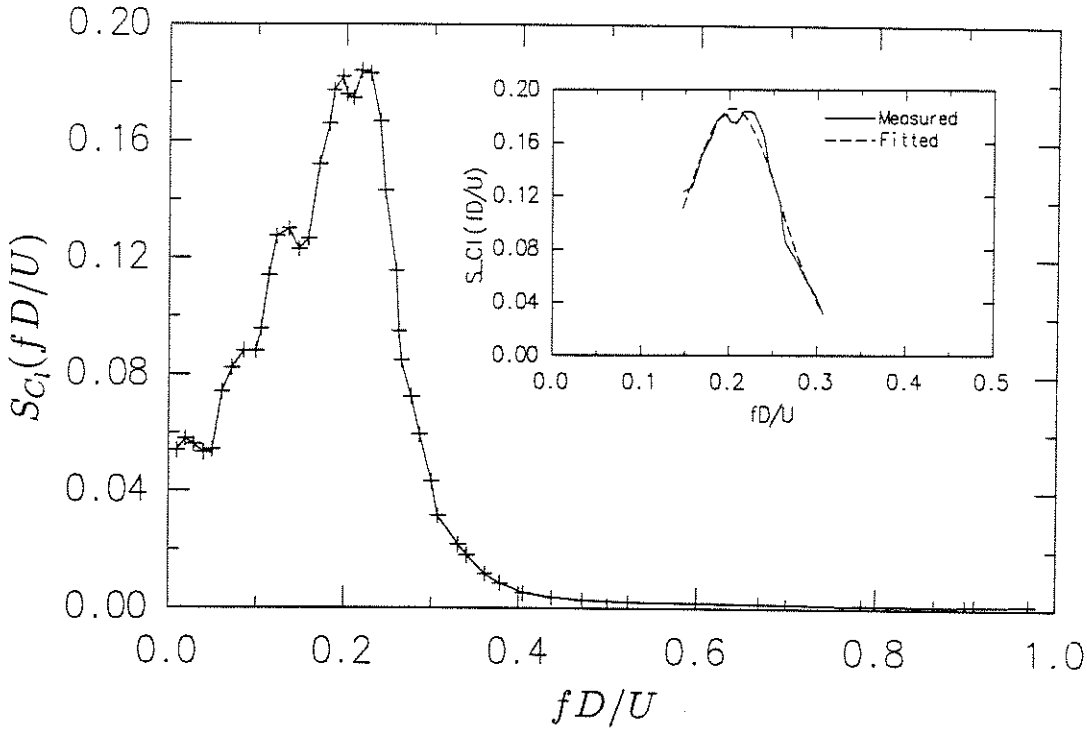

FIGURE 1.49: Spectrum of lift force, replotted from data of Ruscheweyh & Hirsch (1975). The inset shows a curve fitted to the spectral peak ($B = 0.38$).

range of Reynolds numbers obtained was $6 \times 10^6 < Re < 1.44 \times 10^7$. The Reynolds number for the results discussed below was 6.7×10^5. The distribution of mean pressure around the structure showed that boundary layer separation took place at $\theta \approx 105°$, in agreement with figure 1.7. The mean drag coefficient was 0.49 and the value of sectional RMS coefficient of lift was 0.18. The structure was tapered, which generally leads to a reduction in fluctuating cross flow loads, due to disruption of coherent vortex shedding, while the television and restaurant sections at 150 m and 127 m would probably act to reduce the influence of effects normally associated with free ends.

A spectrum of lift force was obtained; this is presented here in figure 1.49. The spectrum is normalized such that $\int_0^\infty S_{C_l}(f_r)\, df_r = \sigma_{C_l}^2$. The spectrum of lift force is broad, with substantial low frequency energy. A curve of the form (1.15) has been fitted to the spectral peak from Ruscheweyh and Hirsch's data, as shown in the inset of figure 1.49. This gives a Strouhal number of 0.20, a Bandwidth parameter $B = 0.38$, and $C_l = 0.16$. Basu's suggestion for quasi-steady broadening of the spectral peak gives $B = (B_0^2 + 2I_u^2)^{1/2} = 0.22$, substantially lower. The energy at low frequency, reaching a finite value at zero frequency, is indicative of cross flow buffeting by turbulence, since the vortex shedding peak is quite distinct.

Hansen (1980) published results taken from the Stigsnaes 130 m chimney stack, which included coefficients of lift and a lift force spectrum. The concrete chimney is situated next to a boiler house of 57 m height; in the other direction, the sea is 100 m away. Reynolds numbers in the range $6 \times 10^6 < Re < 1 \times 10^7$ were recorded. The pressure measurement station from which coefficients of lift and lift force spectra were produced was 14 m ($2.4\,D$) from the top of the chimney, with the result that free end

effects will have influenced the results. The presented spectrum of lift force is similar to that of Ruscheweyh and Hirsch, with an Strouhal number of 0.2 and Bandwidth parameter B ranging between 0.15 and 0.37. Coefficient of lift varied between 0.033 and 0.125; the wide range may reflect the influence of the free end on the results.

The final set of full scale data to be discussed here is that published by Sanada and Nakamura (1983) (also reviewed by Vickery & Basu 1984, Vickery & Daly 1984). The results are interesting partly because they give an indication of the separate effects of buffeting and vortex shedding cross flow forces. The Reynolds number range for the data is $1 \times 10^7 < Re < 4 \times 10^7$. The structure on which the pressures were measured was a concrete chimney stack, 200 m high and with a uniform diameter of 15 m over most of its height (fig. 1.48). The measurement station was 140 m from the ground, or $4\,D$ below the tip of the stack. Values of Strouhal number, lift and drag as functions of Reynolds number, together with velocity, drag and lift spectra are presented in figure 1.50, reproduced from Vickery and Basu (1984).

The values of fluctuating lift and drag coefficients in figure 1.50 seem to display a strong dependence on Reynolds number. However, on the basis that the turbulence and drag force spectra were very similar in shape, Vickery and Basu (1984) argued using quasi-steady assumption that $\frac{1}{2}\sigma_{C_d}/C_d = I_u$, and that the apparent variation of σ_{C_l} and σ_{C_d} is in fact a dependence on turbulence intensity. As a result, they were able to re-plot fluctuating lift and drag coefficients as functions of turbulence intensity, as shown in figure 1.51. Also shown in the figure are values of C_{li} due to turbulence, computed using equation (1.17). Vickery and Daly (1984), suggesting that part of the increase in fluctuating coefficients of lift was due to the influence of fine-scale turbulence on vortex shedding forces, produced an alternative parameter for the effect of turbulence on vortex-induced, rather than quasi-steady, components of fluctuating lift. This parameter, $I_u \cdot \mathrm{LSR}^{-1/3}$, is shown as an alternative scale at the top of figure 1.51.

The spectral information of figure 1.50, presented in two sets, C1–C3 and C4–C6, is very interesting. C1–C3 were recorded for wind coming from the land, with $U(140\,\mathrm{m}) = 17\,\mathrm{m/s}$ ($Re = 1.7 \times 10^7$), $I_u \approx 14\%$, for which $\sigma_{C_l} \approx 0.19$ and $\sigma_{C_d} \approx 0.18$. C4–C6 were recorded for wind coming from the sea, with $U(140\,\mathrm{m}) = 37\,\mathrm{m/s}$ ($Re = 3.7 \times 10^7$), $I_u \approx 7\%$, for which $\sigma_{C_l} \approx 0.07$ and $\sigma_{C_d} \approx 0.07$. The turbulence integral scale would probably have been a little larger with the wind coming from the sea. Firstly, the spectra of fluctuating drag are similar in shape to those of the turbulence, with no distinct spectral spike at the second harmonic of the Strouhal frequency. This implies that buffeting due to the alongwind component of turbulence dominated the fluctuating drag loads. Secondly, the lift force spectra both indicate vortex shedding with a Strouhal numbers 0.20–0.23, combined with buffeting caused by the lateral component of turbulence which produced the low frequency energy. As mentioned, the coefficient of lift for C3 is $\sigma_{C_l} \approx 0.19$ ($I_u = 14\%$), while for C6 $\sigma_{C_l} \approx 0.07$ ($I_u = 7\%$). In Vickery and Basu's paper, the lift force spectra were "partitioned" into background and vortex shedding components, as indicated in figure 1.50, giving Bandwidth parameters $B = 0.36$ for C3 and $B = 0.24$ for C6. They assessed that in both cases, about one-half of the RMS lift was due to vortex shedding forces, the remainder produced by buffeting. This would give an sectional value of σ_{C_l} due to vortex shedding of about 0.10.

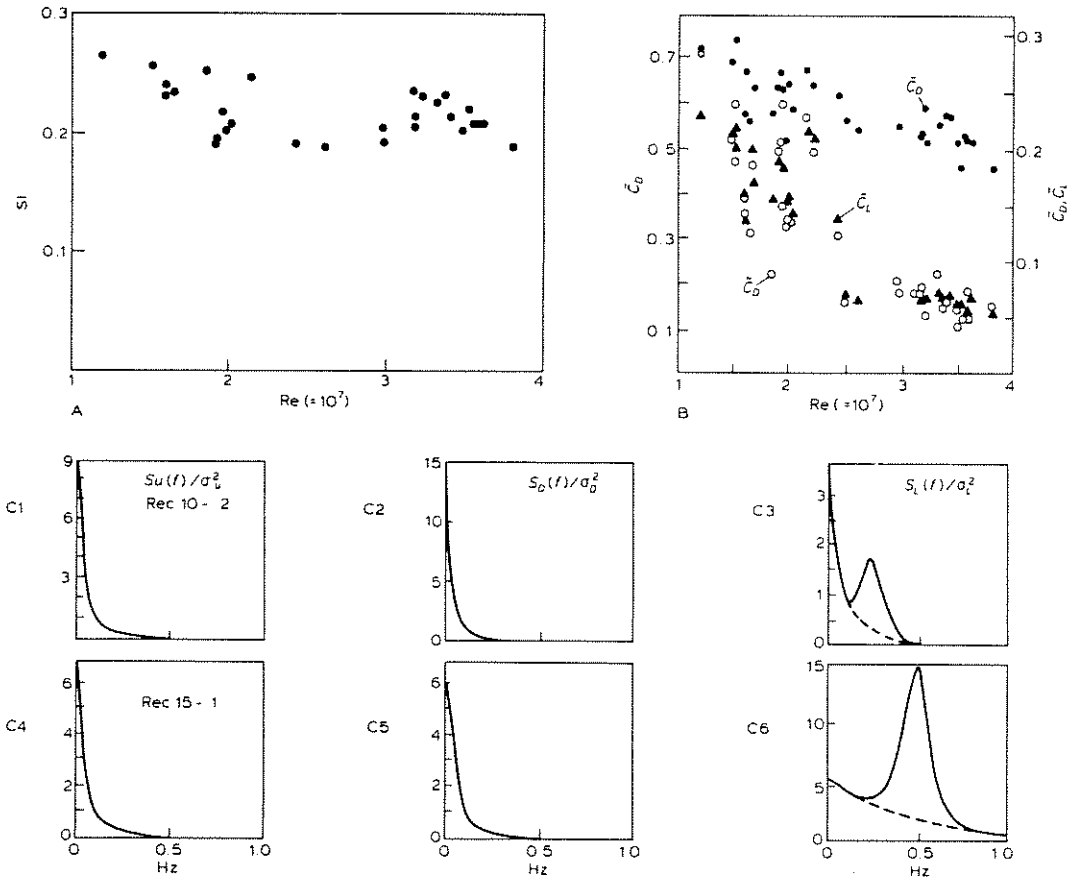

Figure 13 Observations by Sanada and Nakamura at level 140 m on a 200 m high, 15 m diameter, RC chimney:

(a) Strouhal number as a function of R_e where $R_e \approx \bar{u}(140) \times 10^6$
(b) Mean drag coefficient ($\bar{C}_D$), and r.m.s. drag ($\tilde{C}_D$) and r.m.s. lift ($\tilde{C}_L$) coefficients
(c) Spectra of longitudinal turbulence [$S_u(f)$], drag force [$S_D(f)$] and lift force [$S_L(f)$]

C1, C2, C3 Wind off land, $\bar{u}$ (140 m) ≃ 17 m/s, $\sigma_u/\bar{u} \simeq 14\%$, $\tilde{C}_L \simeq 0.19$ and $\tilde{C}_D \simeq 0.18$

C4, C5, C6 Wind off water, $\bar{u}$ (140 m) ≃ 37 m/s, $\sigma_u/\bar{u} \simeq 7\%$, $\tilde{C}_L \simeq 0.07$ and $\tilde{C}_D \simeq 0.07$.

The spectral peaks in C3 and C6 can be represented by:

$$\frac{fS_L(f)}{\sigma_L^2} = \frac{k^2}{2B\sqrt{\pi}} \frac{f}{f_s} \exp\left\{-\left(\frac{(f-f_s)}{Bf_s}\right)^2\right\}$$

where for C3, $k = 0.72$ and $B = 0.36$ and for C6, $k = 0.79$ and $B = 0.24$, and

$$k = \frac{\tilde{C}_L \text{ (vortex)}}{\tilde{C}_L \text{ (total)}}$$

Note that the spectra shown are such that $\int_{-\alpha}^{+\alpha} S(f)\, df = \sigma^2$.

FIGURE 1.50: Data measured by Sanada & Nakamura (1983), reproduced from Vickery & Basu (1984).

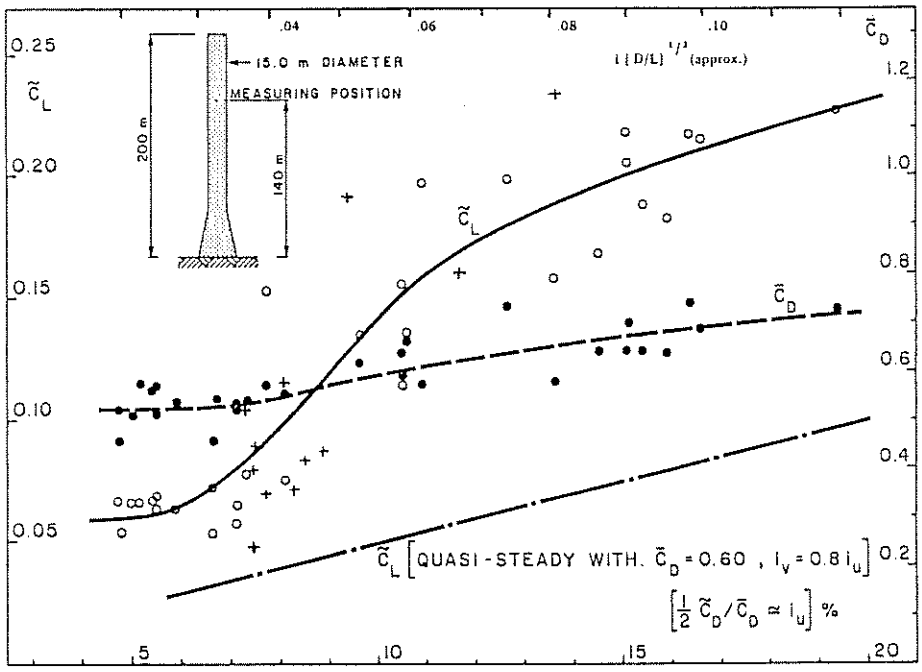

FIGURE 1.51: Coefficients of fluctuating lift and drag as functions of turbulence intensity; data from Sanada & Nakamura (1983), as re-plotted by Vickery & Daly (1984). Nomenclature as shown on fig. 1.50.

1.6 Lift Forces on Oscillating Cylinders

This section is concerned with measurements of lift force made on oscillating cylinders. In the experimental results to be discussed below, emphasis has usually been placed on measuring that portion of lift force which is correlated with motion of the cylinder. This does not, of course, imply that *only* forces correlated with motion acted on the cylinders in the various experiments; the influence of motion on the portions of lift uncorrelated with cylinder motion has rarely been addressed. Note that the partitioning of lift into portions correlated and uncorrelated with motion does not imply that this decomposition is an adequate representation of lift force for the purpose of cross flow response prediction.

1.6.1 Means of Measurement

The fluid forces which act on oscillating cylinders may be measured or estimated in various ways. The two which are perhaps the most obvious are also used for fixed cylinders: measurement of force acting on some length of cylinder, or simultaneous measurement of pressures at a large number of pressure tappings distributed around a diameter. The first of these two methods (by far the most popular of the various approaches) usually entails some correction of the results to account for the force required to accelerate the mass of the measurement section. The second may require a similar correction to allow for pressure fluctuations caused by acceleration of fluid in pressure-tapping lines.

Historically, it has almost always been the case that forces were measured directly on cylinders which were forced to oscillate, although there is no fundamental reason why this should be so. Recently, Reid and Hinwood (1987) described an experimental rig which enabled the measurement of cross and along-flow force on a freely-vibrating cylinder. The relationship between forces which act on freely-vibrating cylinders and cylinders forced to oscillate cross-flow is unclear. As mentioned in § 1.4, experiments and computations by Staubli (1983) have increased confidence that the two sets of forces are closely related.

An indirect means of measurement of motion-correlated forces is to measure the frequency and logarithmic decrement (or increment) of a spring-supported cylinder given an initial displacement, from which aerodynamic forces related to cylinder motion may be inferred.

1.6.2 Estimation of Forces Correlated with Motion

There are a number of ways of estimating forces correlated[8] with motion, which are all essentially equivalent. Different experimenters used the methods which best suited the equipment at their disposal. If the cylinder motion is close to being simple harmonic, the motion-correlated forces can be described by forces correlated with velocity and acceleration, with velocity and displacement, or equivalently by a magnitude and phase with respect to one of the three motion variables.

[8]The implication is that the correlation is performed over many cycles of cylinder motion, or until the statistically steady values are reached.

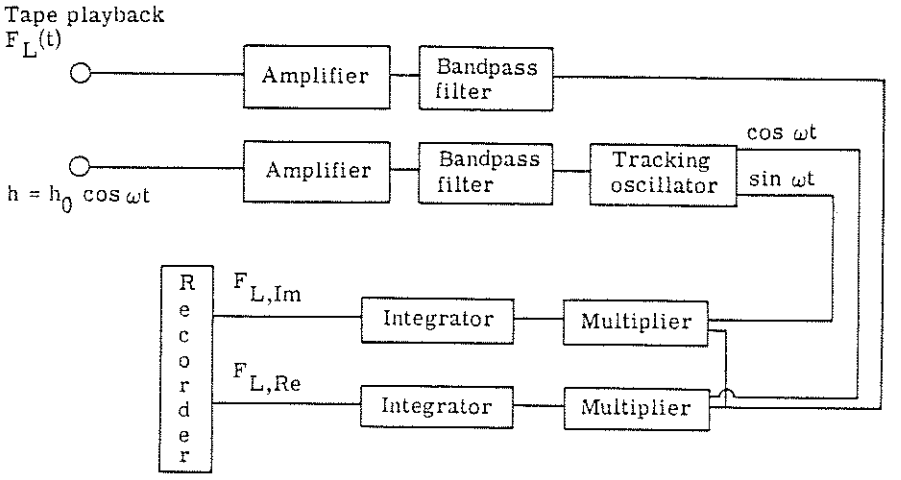

FIGURE 1.52: Block-diagram showing analogue signal processing required to compute $F_a(f)$ and $F_v(f)$. After Jones, Cincotta & Walker (1969).

Given a signal proportional to cylinder acceleration, say $\cos 2\pi ft$, and velocity, $\sin 2\pi ft$, the formulæ for estimating forces related to acceleration and velocity from a record of force $F(t)$ over some averaging period T are

$$\begin{aligned} F_a(f) &= \tfrac{2}{T}\int_0^T F(t)\cos 2\pi ft\,dt &&= \frac{\int_0^T F(t)\cos 2\pi ft\,dt}{\int_0^T \cos^2 2\pi ft\,dt} \\ F_v(f) &= \tfrac{2}{T}\int_0^T F(t)\sin 2\pi ft\,dt &&= \frac{\int_0^T F(t)\sin 2\pi ft\,dt}{\int_0^T \sin^2 2\pi ft\,dt}\,, \end{aligned} \tag{1.19}$$

where $F_a(f)$ and $F_v(f)$ are respectively the acceleration- and velocity correlated force coefficients at the frequency f. A block diagram for the analogue signal processing required to compute F_a and F_v is shown in figure 1.52. Jones, Cincotta and Walker (1969) used this method to compute the magnitude of forces related to cylinder displacement and velocity.

The equivalent discrete method, given the timeseries $F(k)$, $\ddot{y}(k)$ and $\dot{y}(k)$ of force, acceleration and velocity, N records long, is to compute

$$F_a = \frac{\sum_{i=1}^N \ddot{y}(i)\cdot F(i)}{\sum_{i=1}^N \ddot{y}^2(i)} \tag{1.20}$$

$$F_v = \frac{\sum_{i=1}^N \dot{y}(i)\cdot F(i)}{\sum_{i=1}^N \dot{y}^2(i)}\,. \tag{1.21}$$

This corresponds to least-squares fitting a linear relationship between force and acceleration on the one hand, and force and velocity on the other.

An alternative procedure is to use cross-spectral estimates. If $S_{af}(f)$ is the (one-sided) cross-spectrum between force and acceleration and $S_a(f)$ the autospectrum of acceleration,

$$F_a(f) = \frac{\int_0^\infty \Re\left[S_{af}(f)\right] df}{\int_0^\infty S_a(f)\,df} \tag{1.22}$$

$$F_v(f) = \frac{\int_0^\infty \Im\left[S_{af}(f)\right] df}{\int_0^\infty S_a(f)\,df}\,, \tag{1.23}$$

where $\Re$ and $\Im$ denote real (in-phase) and imaginary (out-of-phase) components.

Since the acceleration and velocity are orthogonal functions for simple harmonic motion, the forces $F_a(f)$ and $F_v(f)$ are uncorrelated. Likewise, the residual force F_r

$$F_r = F(t) - F_a \cos 2\pi ft - F_v \sin 2\pi ft \ , \tag{1.24}$$

is uncorrelated with both $F_a(f)$ and with $F_v(f)$. Accordingly,

$$\sigma_F^2 = \sigma_{F_a}^2 + \sigma_{F_v}^2 + \sigma_{F_r}^2 \ . \tag{1.25}$$

1.6.3 Spectral Characteristics of Cross Flow Force

Lock-in is characterized by frequency capture of vortex shedding, so that it matches the cylinder oscillation frequency. When this occurs, cross flow forces exist at the cylinder frequency and to a lesser extent at its harmonics.

Outside the boundaries of lock-in, wake velocity spectra of cylinders forced to oscillate (e.g. Bearman & Davies 1975 for a D-section cylinder) show peaks at or near the fixed-cylinder Strouhal frequency and at the cylinder frequency. A few studies have shown evidence of forces acting on the cylinder at the two frequencies, as illustrated by figure 1.53, taken from the results of Szechenyi and Loiseau (1975) for flow around a roughened cylinder.

No evidence has yet been published which shows this twin-frequency behaviour for cylinders which are free to vibrate, but there is no reason why it should not occur; the lack is perhaps due to the paucity of measurements.

1.6.4 Degree of Correlation with Motion

Forces which act on stationary cylinders usually exhibit narrow-band random characteristics, with near-Gaussian PDFs. Likewise the response traces of vibrating cylinders at low amplitudes of motion are typically narrow-band random with Gaussian PDFs. On the other hand, lightly-damped cylinders at high response amplitudes (order 1 cylinder diameter) exhibit response PDFs which tend to be nearer in form to those of a sinusoidal process (see fig. 1.30); the response has the appearance of a sinewave with small amplitude modulation superimposed, as shown in Wootton (1969). By inference the forces in that case are likely to be of a similar nature, and well-correlated with cylinder motion.

At intermediate amplitudes some proportion of cross flow force is correlated with motion, and some is not. This was shown in the results of Toebes and Ramamurthy (1967), where energy uncorrelated with cylinder motion was shown to exist along with forces correlated with motion. At values of reduced velocity outside the lock-in regime, when motion-correlated forces are still observed, this might be accounted for by the vortex shedding jumping between a locked-in state and a random state similar to that observed for a stationary cylinder. Inside the locked-in range, at large amplitudes of motion, it has not yet been established whether motion-correlated forces account for all the cross flow force, but it is likely that they account for the bulk of it.

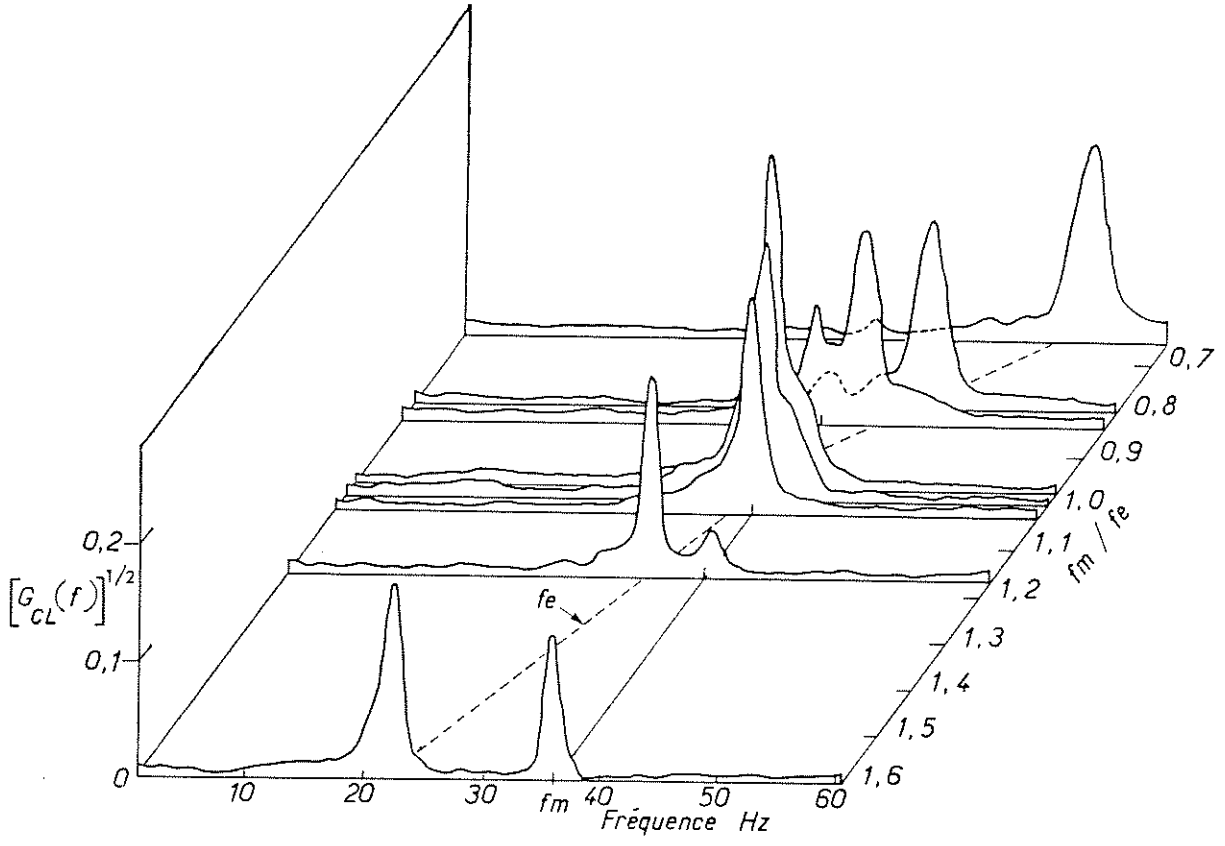

FIGURE 1.53: Frequency characteristics of cross flow force as reduced velocity traverses lock-in range, after Szechenyi & Loiseau (1975). G_{CL} is spectral density of lift force, f_e is vortex shedding frequency for fixed cylinder, f_m is cylinder oscillation frequency.

As to the nature of motion-correlated forces for intermediate amplitudes of cylinder motion, it is not yet clear if they are due to forces which act in deterministic fashion, at every cycle of cylinder motion, in addition to random forces, or if they are due to occasional deterministic events (duration of the order of one motion cycle) set in a background of random vortex shedding. The very nature of correlation itself, which is concerned with integrals of products of variables over long periods, does not allow these two possibilities to be distinguished. On a physical basis, it seems more likely that the second scenario is correct, since the forces are caused by discrete events—the formation and shedding of vortices.

1.6.5 Alternative Descriptions of Motion-Correlated Forces

Various ways of describing motion-correlated forces have been used in the literature, but they all describe the same phenomena, so relationships between the different coefficients can be derived.

Presuming that the motion is simple harmonic, with amplitude αD, at frequency f, the cylinder acceleration, velocity and displacement may be represented by

$$\ddot{y}(t) = (2\pi f)^2 \alpha D \cos 2\pi f t \tag{1.26}$$

$$\dot{y}(t) = (2\pi f) \alpha D \sin 2\pi f t \tag{1.27}$$

$$y(t) = -\alpha D \cos 2\pi f t \, . \tag{1.28}$$

If lift forces per unit length are decomposed into components correlated with cylinder acceleration and velocity, as per equation 1.24

$$l(t) = l_a \cos 2\pi f t + l_v \sin 2\pi f t + l_r(t) \, , \tag{1.29}$$

where l_r describes the residual lift force, uncorrelated with cylinder motion. Coefficients of lift are produced by dividing these forces per unit length by $\rho U^2 D/2$ to give

$$C_l(t) = C_{la} \cos 2\pi f t + C_{lv} \sin 2\pi f t + C_{lr}(t) \, . \tag{1.30}$$

In this thesis, the approach taken is to describe the acceleration-correlated lift force per unit length in terms of the acceleration of an equivalent mass of fluid

$$\begin{aligned} l_a(t) &= -C_a \cdot \rho \frac{\pi D^2}{4} \cdot \ddot{y}(t) \\ l_a &= -C_a \cdot \rho \frac{\pi D^2}{4} \cdot (2\pi f)^2 \cdot \alpha D \, . \end{aligned} \tag{1.31}$$

C_a can be interpreted as a coefficient of added mass (Sarpkaya & Isaacson 1981).

The velocity-correlated force per unit length is described in terms of an aerodynamic damping parameter

$$\begin{aligned} l_v(t) &= K_a \cdot 4\pi \rho D^2 f \cdot \dot{y}(t) \\ l_v &= K_a \cdot 16 f \cdot \rho \frac{\pi D^2}{4} \cdot 2\pi f \cdot \alpha D \, . \end{aligned} \tag{1.32}$$

This is convenient because it may be directly compared with the structural mass-damping parameter K_s, or an equivalent aerodynamic damping ratio can be computed; for a uniform cylinder moving as a rigid body

$$\zeta_{\text{aero}} = -K_a \frac{\rho D^2}{m} \,. \tag{1.33}$$

This shows that a positive value of K_a corresponds to negative damping, that is, the structure extracts power from the flow. The correspondence between K_a and K_s arises because velocity-correlated aerodynamic forces per unit length are made dimensionless in K_a in the same way that structural damping forces per unit length are in K_s.

The relationships between the motion-correlated coefficients of lift and the coefficients C_a and K_a are

$$C_a = -\frac{C_{la} V_r^2}{2\pi^3 \alpha} \tag{1.34}$$

$$K_a = \frac{C_{lv} V_r^2}{16\pi^2 \alpha} \,. \tag{1.35}$$

Relationships between the coefficients C_a and K_a and those used by other workers may be derived with the aid of the definitions given by equations 1.31 and 1.32.

1.6.6 Asymptotic Values of Coefficients

The coefficients C_a and K_a have some asymptotic values which can be derived from theoretical fluid mechanics and quasi-steady experimental values.

Low V_r limit In the low V_r limit ($f \to \infty$, or $U \to 0$), the situation becomes equivalent to a cylinder oscillating in a still fluid. If the motion amplitude is low (say $\alpha < 10\%$) and the flow does not separate from the body, potential flow theory gives a value for C_a, while boundary-layer theory gives a value for K_a.

The appropriate theory for the computation of the coefficient of added (or virtual) mass is derived for a circular cylinder in Milne-Thompson (1960, § 9.221) and in Sarpkaya and Iscaacson (1981, § 2.8). The added mass was given a physical interpretation by Darwin (1953), who showed that it was the mass of fluid displaced from its initial position by the passage of a solid body in potential flow. For an infinite circular cylinder, the coefficient of added mass has a particularly simple form:

$$C_a = 1 \,,$$

which shows that the volume of fluid displaced from its rest position is equal to the volume of the cylinder. Experimental results (e.g. Lundgren et al. 1979, Sarpkaya 1978) confirm that the experimental value of C_a in the low V_r limit is unity.

The fact that $C_a = 1$ in still fluid has some consequences for experimental measurements of acceleration-correlated forces. If the experimental method used relies on measuring force acting on some length of oscillating cylinder, it is usually the case that

the transducers measure both the fluid-dynamic force which acts on the cylinder and the force required to accelerate the mass of the cylinder segment. The inertial component must be cancelled out of the total signal so that the component due to fluid loading can be considered separately. Usually the calibration for this cancellation is performed by making adjustments so that the residual transducer output is zeroed when the cylinder oscillates. Ideally such an adjustment is made with the cylinder oscillating *in vacuo* or with the cylinder shielded from the surrounding fluid. However, if this calibration is carried out with the cylinder oscillating in the fluid used in the experiment, the forces required to accelerate the added mass of fluid will be cancelled out as well.

In addition to the added mass forces, which act out-of-phase with cylinder acceleration, damping forces caused by boundary layer shear stresses also act on a cylinder oscillating in a still fluid. These are usually a few orders of magnitude smaller than the forces required to accelerate the added mass. For theoretical values to be established, it is again required that the amplitude of oscillation be small so that flow separation does not occur. In that case, theories developed for the description of oscillatory boundary layers can be applied to estimate the damping forces which act on the cylinder. Batchelor (1967, § 5.13) gives, for a circular cylinder

$$l_v = -\frac{1}{2}\rho\,(2\pi f \alpha D)^2\, D\, 2\pi\, \sqrt{2}\sqrt{\frac{\nu}{2\pi f \alpha^2 D^2}}\,, \tag{1.36}$$

from which it may be established that

$$K_a = -\frac{1}{\sqrt{4\pi}}\sqrt{\frac{\nu}{f D^2}} \quad \propto \quad \sqrt{\frac{1}{Re}}\,, \tag{1.37}$$

where the Reynolds number is based on the maximum cylinder velocity and its diameter.

High V_r limit In the limit as $V_r \to \infty$, a value of K_a may be computed using quasi-steady assumptions (the asymptotic quasi-steady value of C_a being zero).

The quasi-steady lift force per unit length on a (slowly oscillating) cylinder is (Simiu & Scanlan 1986, § 6.2)

$$l = -\frac{1}{2}\rho U D \left(\frac{\partial C_l}{\partial \alpha} + C_d\right)\dot{y}\,, \tag{1.38}$$

(here, α is the angle of attack). For a circular cylinder, $\partial C_l/\partial\alpha = 0$ and the following value for K_a may be derived

$$K_a = -\frac{C_d V_r}{8\pi}\,. \tag{1.39}$$

Experimental Results

In this section, a number of experimentally-derived values of the parameters C_a and K_a are examined. The values come from experiments conducted in smooth flows with

TABLE 1.3: Summary of experiments conducted to determine motion-correlated forces in smooth flows.

Experiment		$K_{a_{max}}$	$Re\|_{K_{a_{max}}}$	AR	Blockage
Protos, Goldschmidt & Toebes	1968	5.4	4.6×10^4	11:1	9.7%
Försching	1968	3.0	1.3×10^5	10:1	Open jet
Jones, Cincotta & Walker	1969	0.84	6.2×10^6	5.3:1	18.8% †
Nakamura, Kaku & Mizota	1971	1.1	1×10^4	8.8:1	5% ‡
Yano & Takahara	1971	1.8	7×10^4	6.7:1	11.5%
Tanida, Okajima & Watanabe	1973	0.79	4×10^3	10.7:1	4.3%
Sarpkaya	1978	0.28	1.5×10^4	$\sim 10:1$	$\sim 5\%$ ¶
Middlin & Simmons	1983	0.83	4×10^3	11.8:1	3.7%

†Slotted tunnel walls ‡Free oscillation, log decrement ¶A number of different cylinders

smooth cylinders; no measurements have yet been made in turbulent flows, and measurements made on roughened cylinders (e.g. Szechenyi & Loiseau 1975) have been excluded. In some cases, only the values of K_a have been presented, since values for C_a are less easy to measure accurately, and interest has tended to focus on K_a, since it has a primary role in determining aerodynamic instability. The survey is not exhaustive; some results (e.g. Bishop & Hassan 1964 b) have been left out because of doubts about the accuracy of the measurements (see Bearman & Currie 1979).

The survey is arranged in chronological order, and the main parameters of each experiment are shown in table 1.3. As can be seen from the table, there is a wide variation in the magnitude of the aerodynamic damping parameter K_a from experiment to experiment. It will be shown below that the variation of K_a with V_r is similar from experiment to experiment, as noted by Vickery (1978). A graphical summary of the values of $K_{a_{max}}$ with their Reynolds numbers is given in figure 1.54, using the chart of Zdravkovich (1990) as a backdrop. This shows that there is a good deal of scatter in the values of K_a, but that there is some sign of variation in K_a with Re similar to that observed for the coefficient of fluctuating lift.

Protos, Goldschmidt and Toebes (1968) carried out a series of experiments in a water tunnel, using circular and triangular section cylinders. Their information concerning forces in phase with cylinder velocity was presented in the form of average work done by the fluid on the cylinder per cycle of motion, E (see fig. 1.25).

$$E = \int_0^T F(t)\dot{y}(t)\,dt\,. \tag{1.40}$$

Using

$$\dot{y}(t) = 2\pi f \cdot \alpha D \cdot \sin 2\pi f t$$

and

$$F(t) = L \cdot 4\pi\rho D^2 f \cdot K_a \cdot \dot{y}(t)\,,$$

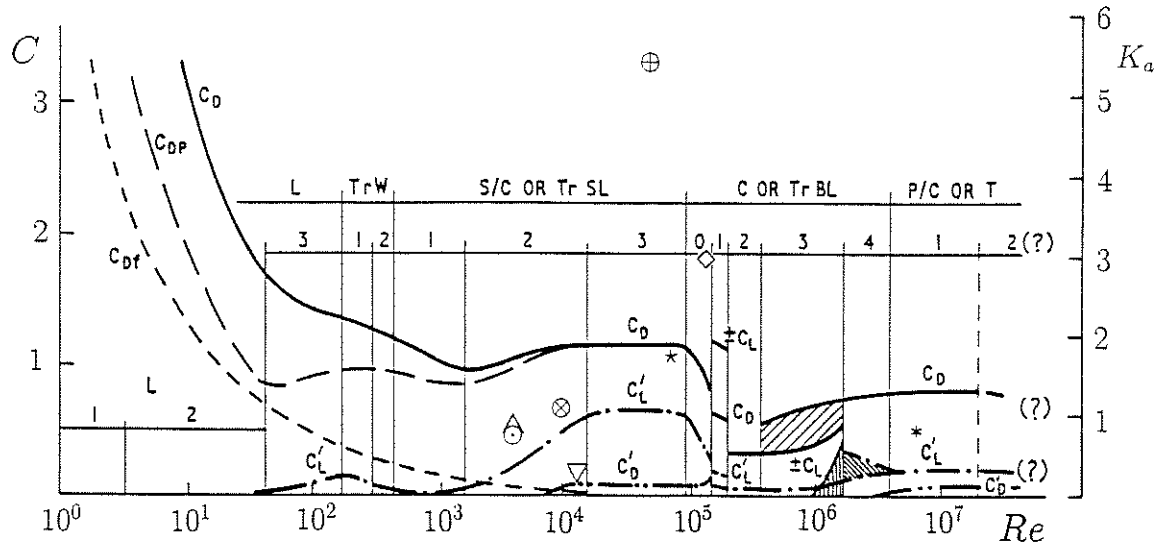

FIGURE 1.54: Variation of $K_{a_{max}}$ with Re, shown with the chart produced by Zdravkovich (1990) as a backdrop. $\oplus$; Protos, Goldschmidt & Toebes (1968). $\diamond$; Försching (1968). $*$; Jones, Cincotta & Walker (1969). $\otimes$; Nakamura, Kaku & Mizota (1971). $\star$; Yano & Takahara (1971). $\odot$; Tanida, Okajima & Watanabe (1973). $\triangledown$; Sarpkaya (1978). $\triangle$; Middlin & Simmons (1983).

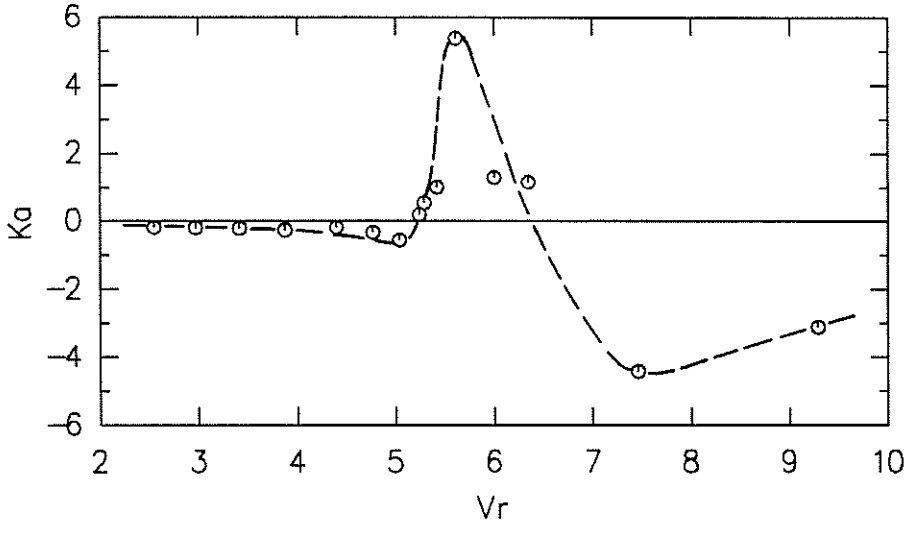

FIGURE 1.55: Values of K_a derived from the results of Protos, Goldschmidt & Toebes (1968). Amplitude $\alpha = 4.24\%$.

where L is the cylinder length

$$K_a = \frac{E}{8\pi^3 \rho L f^2 D^4 \alpha^2} \,. \tag{1.41}$$

Values of K_a for the lowest amplitude of cylinder motion, $\alpha = 4.24\%$, are presented in figure 1.55. The values for the other amplitudes they used ($\alpha_{\max} = 14.3\%$) are similar, but smaller.

Figure 1.55 sets the pattern found in all the results examined for the variation of

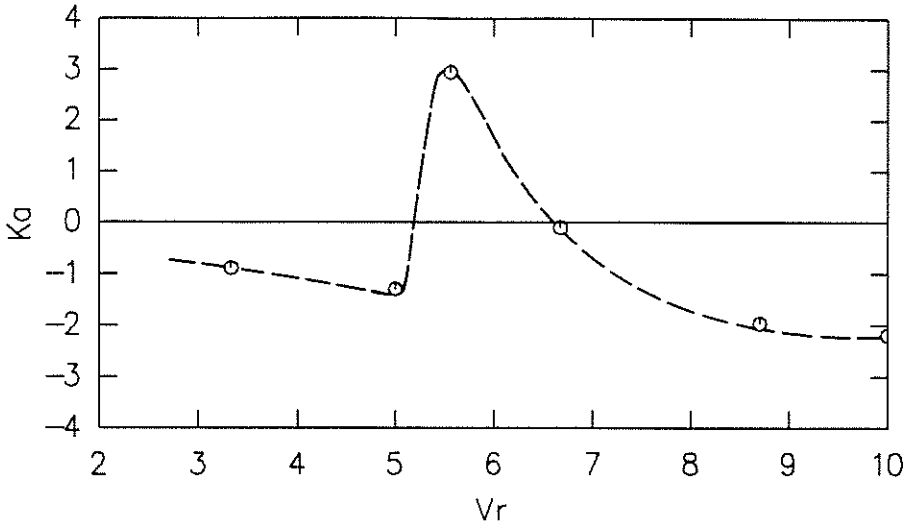

FIGURE 1.56: Variation of K_a with V_r observed by Försching (1968). $\alpha = 1.7\%$, $Re \sim 1.3 \times 10^5$.

K_a with V_r. K_a is negative for most values of V_r (energy extracted from the cylinder), except for a small range of V_r above the value at which the frequencies of cylinder oscillation and fixed cylinder Strouhal frequencies match ($V_r \approx 5$). This corresponds to the instability region found in free-vibration tests. Values of C_a may be derived from their data, using the phase angle information in figure 1.25, but as this is likely to be inaccurate it has not been done.

Försching's tests (1968) were carried out using the open jet of the Göttingen low-speed wind tunnel. A variety of cylinder cross sections were investigated, including one which matched the original Tacoma Narrows bridge. The coefficient K_a'' of velocity-correlated force which was used by Försching is related to K_a by

$$K_a = \frac{K_a'' V_r^2}{8\pi} . \tag{1.42}$$

A sample of the results, for $\alpha = 1.7\%$ and $Re \sim 1.3 \times 10^5$ are plotted in figure 1.56. It can be seen that the general trend of the results matches that of Protos, Goldschmidt and Toebes, although the peak value of K_a is lower.

The results of Jones, Cincotta and Walker (1969) are particularly significant for the design of large structures because of the high Reynolds numbers ($6 \times 10^5 < Re < 1.8 \times 10^7$). The results show some evidence of the influence of Mach number ($0.13 < Ma < 0.4$), and the effects of blockage (18.8%, but with slotted working section) may have been significant. Only results for which the Mach number was less than 0.3 are presented here. The maximum oscillation amplitude employed was $\alpha = 2.78\%$, and the results show that at these amplitudes the majority of lift force was uncorrelated with motion. It seems that the system of inertial force signal cancellation they employed was calibrated in still fluid, and for this reason an offset of 1.0 has been added to their results for coefficient of added mass. The set of results presented in figure 1.57 was recorded at an amplitude of motion $\alpha = 1.39\%$.

The set of data presented in figure 1.57, at $\alpha = 1.39\%$, is the most complete of

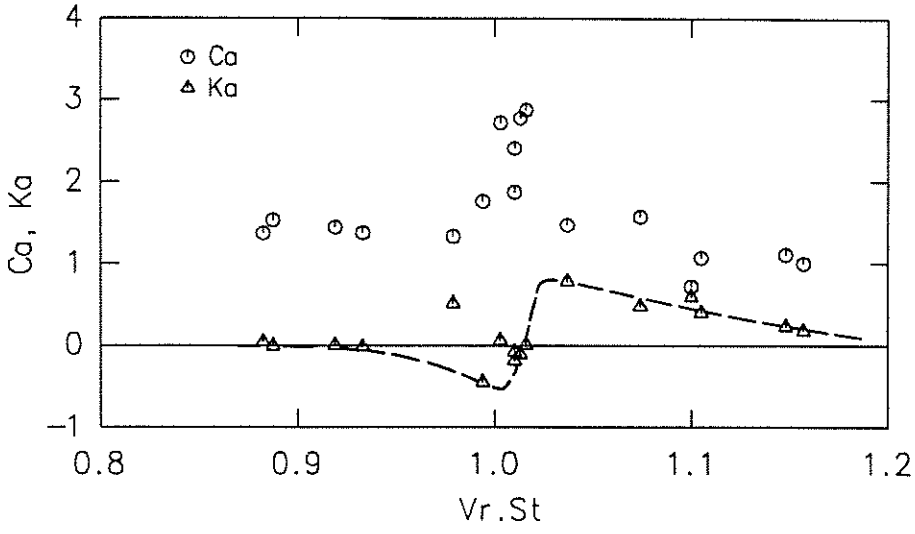

FIGURE 1.57: Values of C_a and K_a calculated from the results of Jones, Cincotta & Walker (1969). $\alpha = 1.39\%$.

those supplied at amplitude levels $\alpha = 0.35\%$, 0.69%, 1.39% and 2.78%. Values at other amplitudes show similar trends with $V_r \cdot St$, while the magnitude of the values dropped slightly with increased amplitude.

Nakamura, Kaku and Mizota (1971) conducted experiments to measure acceleration- and velocity-correlated forces using a free vibration technique. To check the effect of mass ratio $m/\rho D^2$, tests were conducted using cylinders immersed in water or air; the results presented here relate to the experiments conducted in air. The technique employed was to release the cylinder from an initial amplitude $\alpha = 0.1$, and to measure the oscillation frequency, and logarithmic decrement (or increment). By comparing these to still-air values, estimates of the acceleration- and velocity-correlated forces could be made. Again, an offset value of $C_a = 1$ has been added to the results. The Strouhal number in their experiment was 0.215, giving a reduced velocity for frequency matching of $V_r = 4.65$. The results presented in figure 1.58 are for a mass ratio $m/\rho D^2$ of 23.3; the results for mass ratios of 15, 23.3, 58.4 and 108 were very similar. They show the same trends of K_a with V_r seen in the other results in the survey. The values of C_a change from positive to negative near $V_r = 5$, and reach a peak near frequency matching at $V_r = 4.65$, where K_a changes sign rapidly with small change in V_r.

Yano and Takahara (1971) carried out tests with forced oscillation of a cylinder in a wind tunnel. Values of K_a derived from their data for $\alpha = 3.3\%$, figure 1.59, show a similar trend with V_r as those of other workers. In their results, the values of V_r for lock-in were also recorded; the range for $\alpha = 3.3\%$ are shown on figure 1.59. Inside the range, the frequency of lift forces matched that of cylinder oscillation and one peak was observed in the force spectra, while outside the range two peaks were observed in the spectra. The results show clearly that lock-in is not a pre-requisite for motion-correlated forces to exist.

By contrast, the same trend of K_a with V_r is observed even when lock-in occurs over the range, as shown in figure 1.60, from the results of Tanida, Okajima and Watanabe (1973). These measurements were conducted at $\alpha = 14\%$, $Re = 4 \times 10^3$; similar

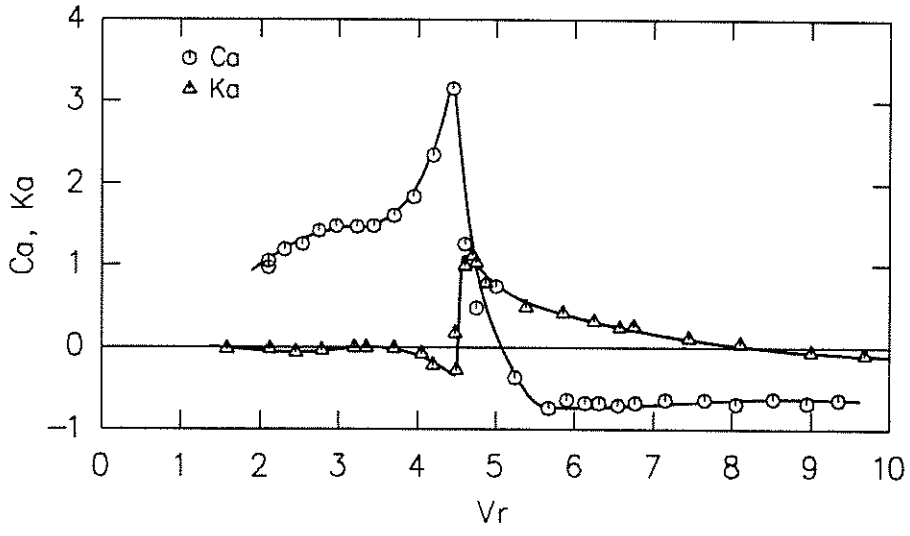

FIGURE 1.58: Values of C_a and K_a calculated from the results of Nakamura, Kaku & Mizota (1971). $\alpha = 10\%$.

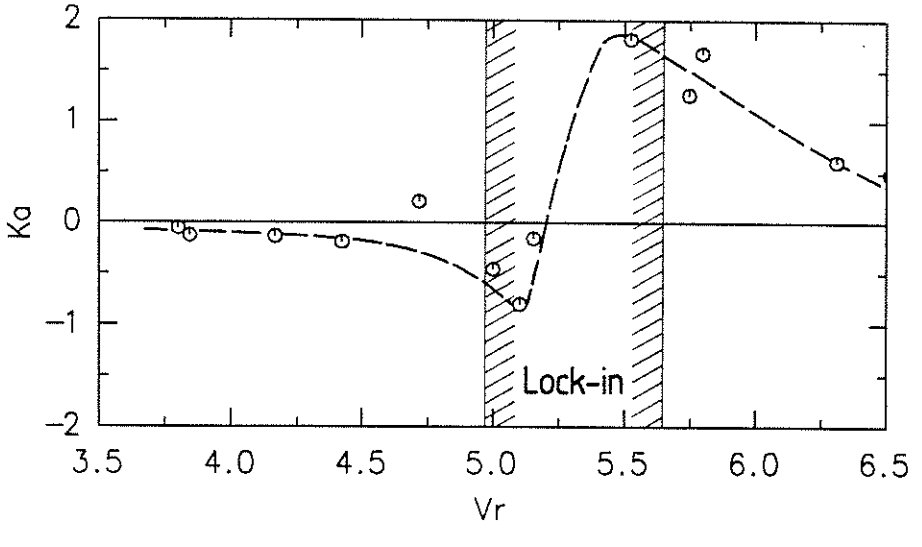

FIGURE 1.59: Values of K_a calculated from the results of Yano & Takahara (1971), showing also the range of V_r for lock-in at $\alpha = 3.3\%$.

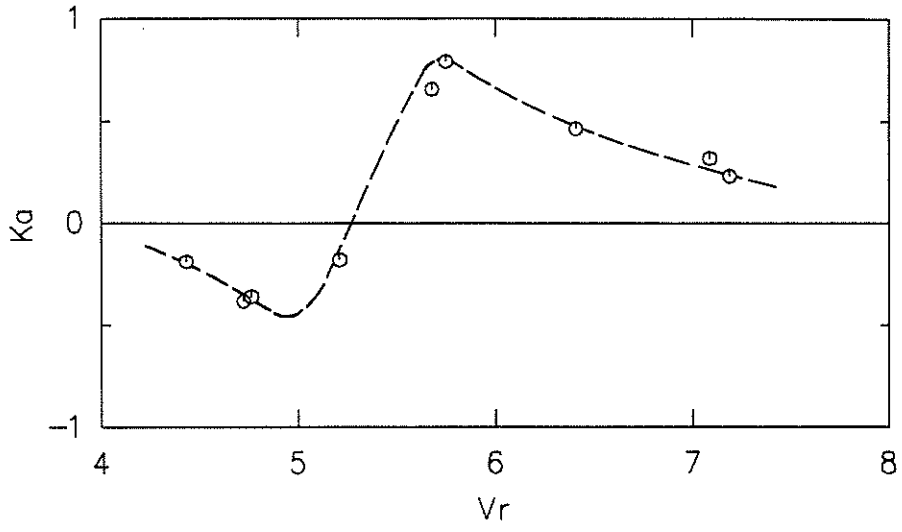

FIGURE 1.60: Values of K_a calculated from the results of Tanida, Okajima & Watanabe (1973). Lock-in was reported for all the indicated values of V_r.

results obtained at $Re = 80$.

Sarpkaya (1978) conducted an extensive series of tests using forced oscillations of cylinders in a water tunnel. The amplitude was varied in the range $\alpha = 0.13$ to $\alpha = 1.03$, and Reynolds numbers were in the range $5 \times 10^3 < Re < 2.5 \times 10^4$. To achieve this variation, a number of cylinders of different diameters, aspect ratios and blockages were used. The values of C_a which Sarpkaya measured are shown in figure 1.61, while figure 1.62 shows the values of K_a.

An interesting aspect of his measurements was that the range of amplitudes employed was great enough to arrive at values of K_a which were negative over the complete range of V_r. The values of K_a measured at $V_r = 5.0$ are shown as a function of amplitude in figure 1.63. This graph indicates that the maximum amplitude for free vibration, reached in the limit $K_s \to 0$, would be $\alpha \sim 0.9$. Another feature of the results is that they give the lowest values of $K_{a_{max}}$, lower than those at the nearest comparable Reynolds number (Nakamura, Kaku & Mizota) by a factor of about four, as shown in figure 1.54. Sarpkaya's results have been used as the basis of schemes for prediction of response amplitudes by Patrikalakis and Chryssostomides (1985, 1986).

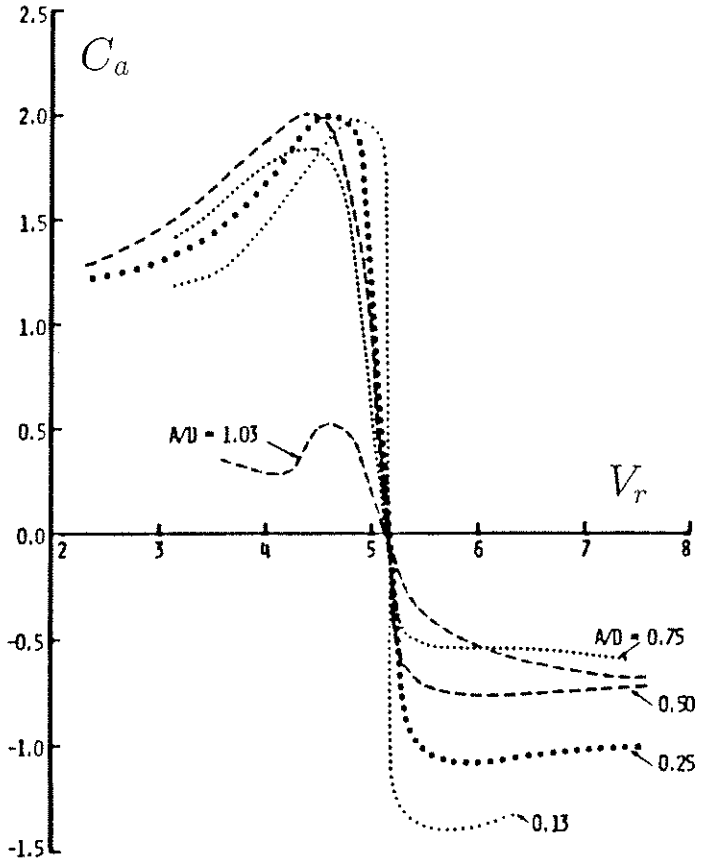

FIGURE 1.61: Values of C_a presented by Sarpkaya (1978).

The last set of results to be examined here are those of Middlin and Simmons (1983). Their measurements of velocity-correlated forces were presented in the form of a power transfer coefficient

$$Z_p = \frac{P}{\rho f^3 D^4} ,$$

where P is the time-averaged power transfer per unit length. From this,

$$K_a = \frac{Z_p}{8\pi^3 \alpha^2} . \tag{1.43}$$

The results for smooth flow are presented in figure 1.64. Results conducted in turbulent flow (grid turbulence with $I_u = 4.5\%$ and $L_u^x/D \sim 1$) were also given; little change was produced by the addition of turbulence, probably because the flow was subcritical and the turbulence intensity fairly low.

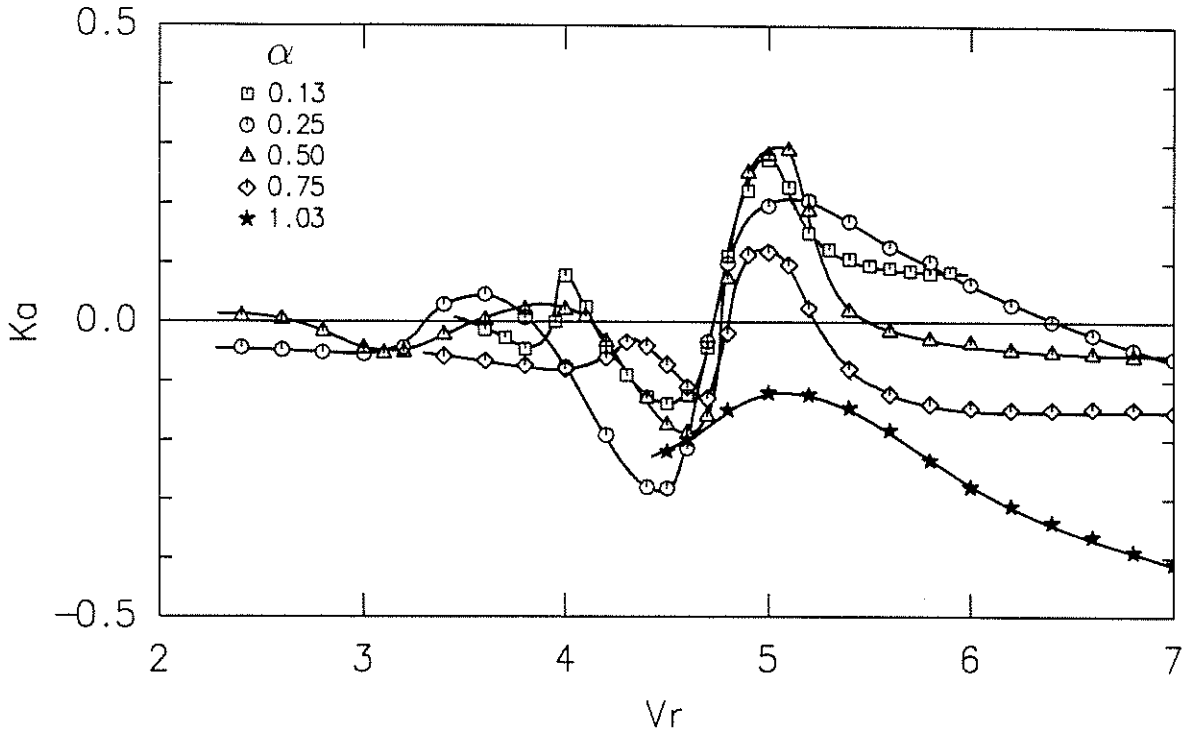

FIGURE 1.62: Values of K_a calculated from the results presented by Sarpkaya (1978).

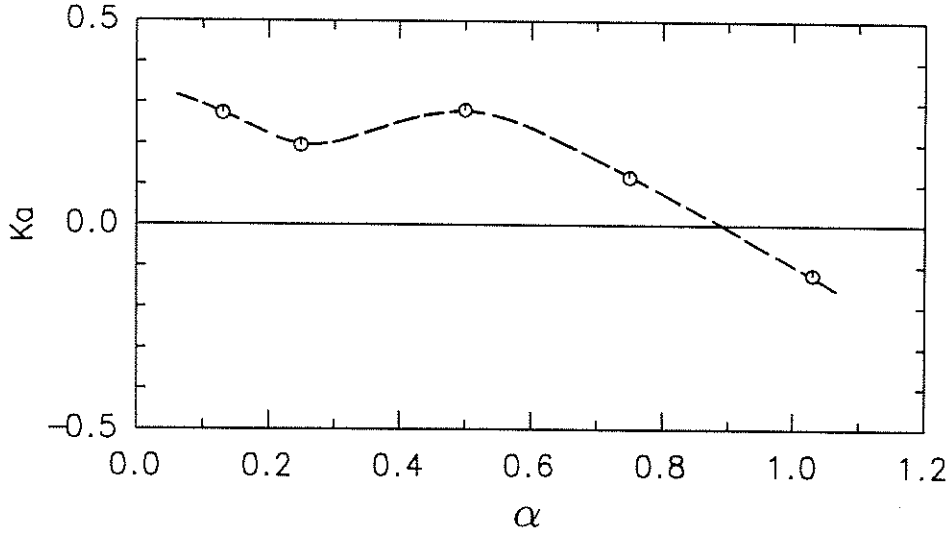

FIGURE 1.63: The values of K_a at $V_r = 5$ as a function of amplitude α. From the results of Sarpkaya (1978).

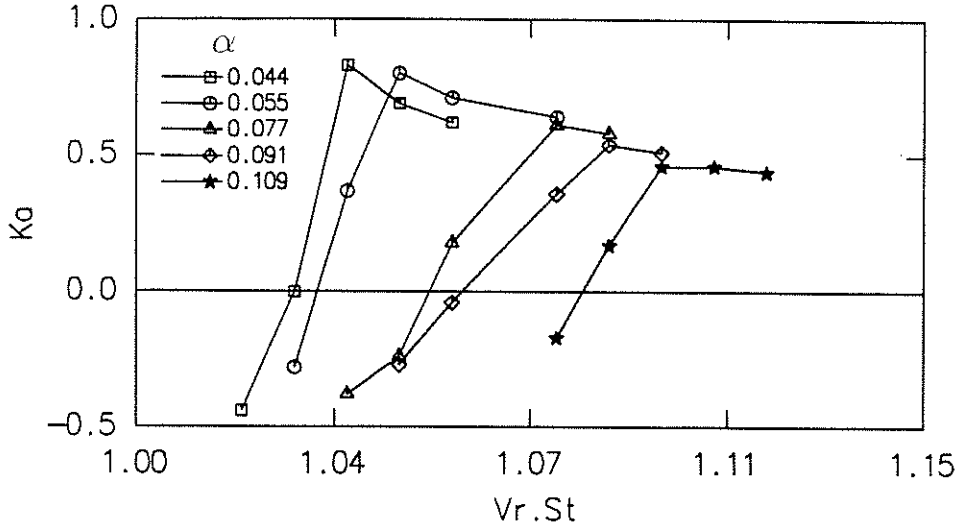

FIGURE 1.64: Values of K_a calculated from the results of Middlin & Simmons (1983).

1.6.7 Influence of Turbulence

As discussed in § 1.4.5, no experiments have directly examined the influence of turbulence on motion-correlated forces acting at sections of circular cylinders.

1.7 Prediction of Cross Flow Response

No single procedure has yet become accepted for the prediction of cross flow response of slender cylindrical structures in flows of air. This may be contrasted with the prediction of the along flow response of such structures in turbulent flows, where the "Gust Factor" method is now commonly used. Much of the difficulty is due to the fact that the vortex shedding process and particularly its interaction with structural oscillation is poorly understood. Further problems are introduced by a lack of understanding of the influence of turbulence on vortex shedding, and to a lesser extent the influence of structural taper, surface roughness, wind shear, and mode shapes. Finally there is the difficulty of verifying the performance of prediction methods since it is costly to measure the forces which act on, and the resulting response of full-scale structures and the characteristics of the flows to which they are subjected.

For a general structure, the shapes of the vibration modes must be taken into account; the mode j with characteristic frequency f_{nj} is described by a mode shape $\Psi_j(z)$. In this case, the most natural generalization of m, the mass per unit length of the structure, is the "mode-generalized" mass per unit length

$$m_{ej} = \frac{\int_0^L m(z)\Psi_j^2(z)\,dz}{\int_0^L \Psi_j^2(z)\,dz}\,, \tag{1.44}$$

which is usually similar to the mass per unit length over the portion of the mode which shows significant response. Similarly, the average diameter in that region, D_j, may be

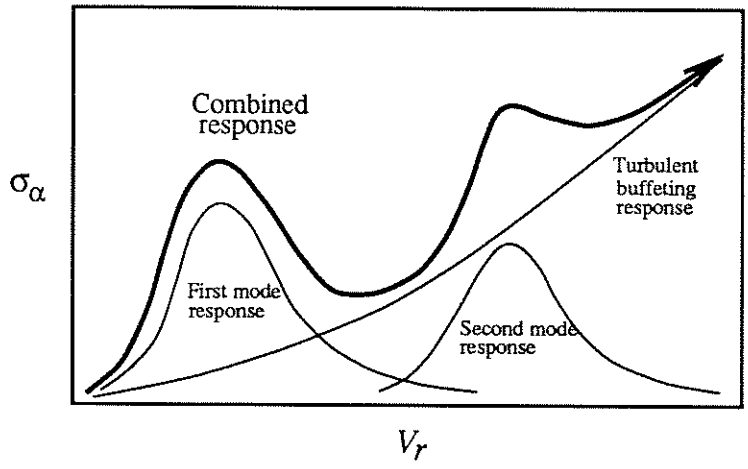

FIGURE 1.65: Sketch of the progression of the cross flow response of a slender structure in a turbulent flow as the mean flow speed changes.

computed. Together these may be used to estimate the mass-damping parameter for the jth vibration mode

$$K_{sj} = \frac{\zeta_j m_{ej}}{\rho D_j^2} \,. \tag{1.45}$$

1.7.1 Summary of Response Characteristics

Vortices are formed in the wake of bluff structures as a result of concentration and interaction of the shear layers (separated boundary layers) which leave it. The vortices are formed alternately on the two sides of the wake in a quasi-periodic manner, giving rise to regions of low pressure which exert forces on the structure. Significant vortex-induced vibration amplitudes only occur when the frequency band of the vortex shedding forces overlaps that of a structural vibration mode. The progression of forced random vibration response amplitude with mean flow speed is sketched for an idealized slender structure in figure 1.65. At lower speeds, vortex induced vibration of the first few modes provides most of the response, which eventually becomes dominated by response of the lowest modes to cross-flow buffeting caused by the lateral components of turbulence.

The characteristics of the vortices shed by slender structures change with the amplitude of structural vibration response. If the amplitude is large enough there is an interaction between the movement of the structure and the formation of vortices. This fact greatly complicates the prediction of vibration amplitudes.

The nature of the forces and response is observed to be a strong function of the mass-damping parameter K_{sj} which partly characterizes the ratio of the structural damping forces to the forces produced by vortex shedding.

Forced Random Vibration

If the mass-damping of the structure is sufficiently large the amplitude of response is small ($\sim 1\%\ D$) and there is little interaction between the vortex forces and the structural movement. In this case the vortex shedding process is not completely organized in time or space. The statistical properties of the forces produced by vortex shedding are those of a narrow band random process. At any one site the forces are not characterized by a single frequency and fixed phase, but the energy is spread over a band of frequencies. The PDF of the forces has the typical bell shape of a Gaussian distribution. The organization of the vortices along the span of the structure is also incomplete.

From the point of view of predicting the mean-squared structural response to vortex induced loads, this lack of organization is reflected in the description of how the cross-spectral density of forces acting at any two points on the structure varies with the location of the points. A simpler but less complete alternative is to describe the lack of organization using a correlation function which measures the correlation between forces acting at different sections of the cylinder at the same instant, in conjunction with autospectra of lift forces. The value of the correlation function is observed to drop from unity to zero as the spanwise distance between the sections at which the forces are measured increases.

For lightly-damped structure the response shows typical characteristics of forced random vibration of a lightly damped system driven by random loads which have a bandwidth comparable to or larger than the Half-Power Bandwidth of the structural admittance $4\pi\zeta_s f_{nj}$. The structural response has a PDF which is near-Gaussian, and its spectral density is concentrated in a narrow band around the structural natural frequency; the structure acts as a mechanical band-pass filter of the vortex-shedding loads.

Motion-Correlated Forces

If the mass-damping of the structure is small the amplitude of response can become large enough to influence the vortex shedding process, so tending to produce vortices which are more organized in space and time. Some proportion of the forces produced by these vortices are correlated with the motion of the cylinder. When averaged over a long period of time, some of the otherwise apparently random force has a definite phase relationship to the motion of the structure; as amplitude of motion increases, the vortices and the forces become less random, and the portion of the force correlated with structural motion increases. The cross flow forces become more sinusoidal in character at each section along the structure as the amplitude of response rises, and the correlation between forces along the span increases as the vortices fall into a spanwise-constant phase relationship to the structural motion. This is a non-linear feedback effect, since the motion of the structure produces more organized vortices which exert greater loads on the structure, giving a larger structural response which in turn leads to still better-organized vortices, and so on. The change in response amplitude with K_s is illustrated in figure 1.29, from the tests conducted by Wootton (1969) on a model stack. The increasing organization of the vortices is reflected in the statistics of the vortex shedding forces and the response. The spectrum of the forces becomes sharper

and the PDF of the response approaches that for a sinusoidal process, with a peak factor of $\sqrt{2}$ (fig. 1.30).

If the centre frequency of the vortex shedding is removed from the structural natural frequency then two peaks may be observed in the spectra of the cross flow vortex shedding forces, one at the structural vibration frequency and one at the vortex shedding frequency. If the separation of the frequencies is not too large, the non-linear feedback between the structural motion and the vortices can result in the the synchronization of vortex shedding with the structural oscillation ("lock-in", see fig. 1.16). The range of separation of frequencies for which this entrainment or lock-in can occur increases as the mass-damping of the structure is reduced (fig. 1.28).

Ultimately as the mass-damping is reduced to zero, a limiting response amplitude is reached, typically of the order of one cylinder diameter.

Implications for Design

For most civil engineering structures, the stresses induced by large amplitudes of motion are high enough to produce significant fatigue damage, if not to produce failure immediately, so the designer must ensure that the mass-damping of the structure does not become so low that there is danger of entering the regime where the non-linear feedback effect discussed above can take hold. If this is a problem, possible solutions are to add damping or mass so that the mass-damping of the structure increases, to raise the natural frequency of the structure by stiffening so that the critical velocity (where the frequencies of vortex shedding and the structures coincide) lies above the design range, or to disrupt the vortex-shedding process by adding devices such as helical strakes to the structure.

Often the simplest alternative is to add damping to the structure. At the transition from the forced random vibration to the motion-dependent regime, the response amplitude is sensitive to comparatively small changes in damping. This means that while small increases in damping can reduce the response significantly, uncertainties in damping estimates should be allowed for in design, since a variation in damping below the design estimate can bring about a transition between regimes. Once the low-amplitude forced vibration regime is reached, the amplitude of the response becomes less sensitive to further addition of damping: the RMS response is halved each time the damping is increased by a factor of four. The various options open to the designer have been more thoroughly discussed by Vickery, Isyumov and Davenport (1983).

Features of Alternative Response Models

The greatest amplitude of vortex-induced response occurs when vortex shedding and structural natural frequencies coincide and most prediction models available concentrate on this condition. For structures under examination for vortex induced vibrations in air, response occurs mainly at the natural frequencies of the structure even if the vortex shedding forces have a significant bandwidth.

A number of different models for predicting structural response of slender cylindrical structures have been produced, with varying degrees of sophistication and success in

predicting observed responses. Often the models and their numerical parameters are based around a comparatively small set of calibration data, and are found to work poorly when extended to new situations. The models tend to fall naturally into two main groups; those used to predict large- and low-amplitude motions. In the regime where large amplitudes of response are observed there have been two major sets of models, the *wake oscillator* and *correlation length* types. Typical examples of both types are presented by Blevins (1977). *Negative-damping* models (§ 1.7.5) provide a transition between low and high amplitude response regimes.

1.7.2 Low Amplitude Response—Forced Random Vibration

Turning first to the low amplitude regime, the response is typically found to be narrow band random, and the more successful models are based in random vibration theory as applied to line-like structures. Crandall (1979) gives a detailed account of the theoretical development. If, as is typically the case for the lowest vibration modes of lightly-damped slender structures, there is no significant frequency overlap between the responses of the different modes, the theory requires a description of the spatial distribution along the structure of the co-spectra[9] of vortex shedding loads.

Most of the costly civil engineering structures in this regime have been chimney stacks, so the methods and their calibration have been oriented towards stack design. The first significant model of this type was that of Vickery and Clark (1972). ESDU (Item 85038) appear to have used that model as the basis of their *broad band*[10] method and while it seems that there has been some adjustment to the numerical values of the parameters, the responses predicted using the two models are likely to be very similar.

The ESDU *broad band* method assumes that the bandwidth of the excitation is much broader than that of the resonant peak of the admittance function. Specifically the approximation is that the vortex shedding is a white noise process with a constant value of spectral density equal to that at the peak of the actual spectrum of vortex shedding forces. This simplifying assumption is often used for structures with lightly damped vibration modes and natural frequencies that are widely separated (see Newland 1984 ch. 14). The inaccuracies incurred by this assumption are small compared to the uncertainties in the parameters of the response model.

The general form of the RMS response predicted by these methods is

[9]The real parts of the cross-spectra.

[10]While the terms "broad band" and "narrow band" are conventionally used to describe the relative frequency bandwidth of a stochastic process compared to the frequency at which the maximum spectral density is observed, the ESDU usage is slightly different. ESDU use the terms to describe the relative bandwidth of the forces produced by vortex shedding compared to the Half Power or Mean Square bandwidths (Newland 1984, ch. 14) of the structural mechanical admittance function. At low amplitudes of structural response the vortex shedding forces have a bandwidth greater than or comparable to the structural mechanical admittance bandwidth (*broad band*). When the response amplitude becomes sufficiently large the vortices become organized by the structural motion. The bandwidth of the vortex shedding forces then narrows significantly to become smaller than that of the mechanical admittance (*narrow band*). *Emphasized* text is used here to denote the ESDU usage.

$$\sigma_\alpha = \frac{1}{D_{\text{ref}}} \cdot \sqrt{\frac{\pi f_j S(f_j)}{4\mathcal{K}_j}} \cdot \frac{1}{\sqrt{\zeta_j}} \,. \tag{1.46}$$

Here, f_j is the frequency of oscillation of the jth vibration mode, $\mathcal{K}_j$ is the modal stiffness for that mode, and $S(f_j)$ is the value of the spectral density of the mode-generalized cross flow force at the frequency f_j. D_{ref} is some reference diameter, and σ_α is the RMS modal response amplitude made dimensionless with respect to D_{ref}.

1.7.3 Wake Oscillator Models

The wake oscillator models are empirical dynamical models based on observations such as that made by Bishop and Hassan (1964 b), that the behaviour of the wake of the cylinder shows some of the characteristics of a "non-linear self excited oscillator" coupled to the motion of the structure. The mathematical progenitor of these models is contained in the paper by Birkhoff (1953). Models of this sort are able to reproduce in a qualitative way much of the observed behaviour such as sensitivity to structural damping, self limiting amplitude and frequency entrainment. Many wake-oscillator models have been produced; ten such models are discussed by Scanlan in Dowell et al. (1989). Dowell (1981) expressed the general aim in the construction of these models:

> The desire, of course, is to obtain the equations of the solid oscillator and the fluid oscillator by separate, independent means and to use them together to *predict* the behaviour of the combined fluid-elastic system.

The main difficulty is that the models are empirical, with no detailed relationship to the fluid dynamics being given. Often they have three or four free parameters, fitted to match the model to particular experimental results, and so have limited or uncertain wider application. None of them has been developed to the point where it could be used in high Reynolds number applications in turbulent flow, partly because there have been insufficient experiments to enable all the parameters to be matched (it is often unclear what the physical significance of the parameters is).

The wake oscillator models are as yet unsuited to the prediction of response of typical civil engineering structures, perhaps largely because emphasis has been placed on predicting the large oscillations which occur with low values of the mass-damping parameter, and not on the low amplitude forced random vibration regime. For example, the wake-oscillator models have thus far been unable to incorporate or account for the observed change with oscillation amplitude in the spanwise correlation of vortex shedding forces (they assume perfect correlation). More importantly, cross flow forces have been assumed vary sinusoidally with time, while observations show that the actual variation is narrow-band random in nature at small amplitudes of structural oscillation. On the other hand, the models are capable of predicting frequency entrainment, hysteresis, and amplitude-limited behaviour at low values of K_s.

1.7.4 Correlation Length Models

Correlation length models concentrate specifically on the situation where the vortex shedding frequency matches that of the structure, which is when the largest vortex shedding forces and vibration amplitudes occur. The lift forces are separated into parts in phase with the velocity and acceleration of the structure. This is based on the fact that when the amplitude of response is large enough to significantly influence vortex shedding, the forces produced by the vortices are found to have a definite average phase relationship to the structural motion. Only the part of the lift force which is in phase with the velocity of the structure is dealt with. For high values of mass ratio ($m/\rho D^2$) the part in phase with the acceleration is usually small in relation to the stiffness and inertia forces in the structure (which are in balance since the structure is at resonance), so its main effect is to change the natural frequency by a small amount, usually ignored. The part in phase with the velocity of the structure is balanced by the structural damping forces (which are relatively small).

These models also deal with the fact that the spanwise correlation of the vortex shedding forces is observed to increase with amplitude of structural movement. This is done by employing a spanwise correlation function which is used to describe the correlation between vortex shedding forces acting at different sections at the same time. The function is dependent on amplitude of response, being closer to unity for a greater distance along the structure the larger the amplitude of oscillation. The functional relationship is based on experimental data.

The construction of the models begins with observed responses, and works back to arrive at an amplitude-dependent local coefficient of lift (but only that part in phase with velocity), allowing for mode shape and amplitude dependence of spanwise correlation. This process has been described by Blevins (1977).

The ESDU *narrow band* method is a correlation length model. Examination of the design charts in ESDU 85038/9 shows that the coefficients used are functions of Reynolds number, surface roughness, turbulence intensity and scale. The dependence has been estimated on the basis of experimental results and observations of coefficients found for full size structures as explained in ESDU 85038. The data on which this process has been carried out are somewhat limited and the resulting estimates can consequently show quite large scatter, but at least the physical basis of the coefficients is more clear than is the case for wake oscillator models, and trends in behaviour can be accounted for.

As indicated above, ESDU 85038/9 adopt two different approaches to the prediction of response amplitudes. If the dimensionless amplitude of structural response, αrms, is greater than 2% then *narrow band* responses are predicted using the correlation length model and a peak factor of $\sqrt{2}$ appropriate to a sinusoidal process is used. Otherwise a *broad band* response is assumed and the amplitude is re-estimated with a forced random vibration method (with similar aerodynamic parameters) using a peak factor of 4 appropriate to a Gaussian process. The method to be described next is more realistic in that it predicts a smooth transition between low and high response amplitudes as the structural mass-damping is reduced.

1.7.5 Negative Damping Models

Negative damping models account for experimentally-observed motion-correlated forces by introducing forces proportional to structural motion in the modelling equations. At appropriate reduced velocities, these forces (on average) act in phase with cylinder velocity, and hence have some similarity to negative damping forces. In order to predict structural vibrations at low response amplitudes (high values of K_s), the models also incorporate lift forces which act independently of structural motion. Scanlan (Simiu & Scanlan 1986, § 6.1.1) describes the basis of one such model, but the most significant and well-developed model of this kind is that described first by Vickery (1978) and subsequently developed by Vickery and Basu (1983 a, b, c; 1984, Basu 1982). This model is also discussed in Simiu and Scanlan's book (§ 6.1.2 & ch. 10).

Vickery and Basu's model

The model extends the forced random vibration prediction scheme proposed by Vickery and Clark (1972) by modifying the overall system damping to account for velocity-correlated forces. As such, it is primarily directed to the low amplitude regime, but some work has been carried out in order to calibrate it to observed high amplitude responses (Daly 1986). The form of the model allows a natural progression from low to high responses as K_s drops. The basic assumption used is that the vortex shedding forces and their interaction with cylinder motion may be expressed as the sum of two independent processes. One is the narrow-band-Gaussian vortex shedding process and the other—the motion-correlated part—models velocity-correlated forces as a negative aerodynamic damping, the magnitude of which decreases as response amplitude increases. Although forces correlated with both cylinder acceleration and velocity are observed in experiments (§ 1.6), the model only attempts to describe forces correlated with velocity. This approach is reasonable, since for most structures in flows of air the mass ratio $m/\rho D^2$ is comparatively high, so aerodynamic forces which are correlated with cylinder acceleration are small in relation to the forces required to accelerate the structural mass at resonance. On the other hand, the aerodynamic velocity-correlated forces are often comparable in magnitude to the structural damping forces. Motion-correlated forces vary with reduced velocity, with maximum values of velocity-correlated force coefficients observed at reduced velocities the same as or slightly above the value for coincidence of structural and vortex shedding frequencies. As a result, the maximum values of vortex-induced cross flow response amplitude are expected at reduced velocities in the range 5 to 6.

The velocity-correlated forces are described in terms of the aerodynamic damping parameter K_a. Experimental observations using forced oscillations (e.g. fig. 1.63) suggest that this reaches a maximum value as the amplitude of motion drops to zero and decreases monotonically with increased amplitude until zero values of K_a are reached. This is in agreement with experimental observations for freely-vibrating structures, where it is found that the amplitude of motion is self-limiting as K_s drops to zero. In Vickery and Basu's model, the form adopted for the variation of K_a with α is parabolic, as illustrated in figure 1.66 (a):

$$K_a = K_{a0}\left[1 - \left(\frac{\alpha}{\alpha_L}\right)^2\right] , \tag{1.47}$$

or, equivalently for a uniform cylinder oscillating with a uniform mode shape:

$$\zeta_{\text{aero}} = -\frac{\rho D^2}{m} K_{a0}\left[1 - \left(\frac{\alpha}{\alpha_L}\right)^2\right] . \tag{1.48}$$

Here, K_{a0} is the aerodynamic damping parameter in the limit $\alpha \to 0$; α_L is a limiting amplitude, reached as $K_s \to 0$.

This two-parameter model for the velocity-correlated cross flow forces can alternatively be considered in the form of a coefficient the of lift forces correlated with structural velocity, using equation 1.35, i.e.

$$C_{lv} = \frac{16\pi^2 K_{a0}}{V_r^2}\left[\alpha - \frac{\alpha^3}{\alpha_L^2}\right] . \tag{1.49}$$

as shown in figure 1.66 (b).

Stripped to its essentials, the model suggests that significant amplitudes of response only arise when K_s drops to reach K_{a0}, and if it falls below this, the amplitude settles at such a level that the overall system damping is zero, as shown in figure 1.66 (a).

The negative aerodynamic damping is incorporated into the random vibration prediction procedure described in § 1.7.2 simply by subtracting it from the structural damping. As described there, the approximation for the response of a lightly-damped mode is of the form

$$\sigma_\alpha = \frac{1}{D_{\text{ref}}} \cdot \sqrt{\frac{\pi f_j S(f_j)}{4\mathcal{K}_j}} \cdot \frac{1}{\sqrt{\zeta_j}} .$$

The introduction of negative aerodynamic damping is most straightforward in the case of a constant-diameter cylinder oscillating with a uniform mode shape in a uniform flow, in which case the equation is modified as follows:

$$\sigma_\alpha = \frac{1}{D_{\text{ref}}} \cdot \sqrt{\frac{\pi f_j S(f_j)}{4\mathcal{K}_j}} \cdot \frac{1}{\sqrt{\zeta_j - \frac{\rho D^2}{m} K_{a0}\left[1 - \left(\frac{\sigma_\alpha}{\alpha_L}\right)^2\right]}} . \tag{1.50}$$

Since the vibration is random, it is assumed that the negative aerodynamic damping is a function of the RMS amplitude σ_α; likewise the value of α_L in equation (1.50) is now interpreted as a limiting RMS amplitude.

Some slight complications in the coefficients of equation (1.50) are introduced when the assumptions of uniform mode shape, uniform diameter and flow are relaxed, but the form of the equation does not change. The detail may be found in the papers by Vickery and Basu (1983 a, b).

The form of the variation of RMS response with amplitude predicted by the model is shown in figure 1.67 (a). At high values of K_s, the response amplitude is primarily

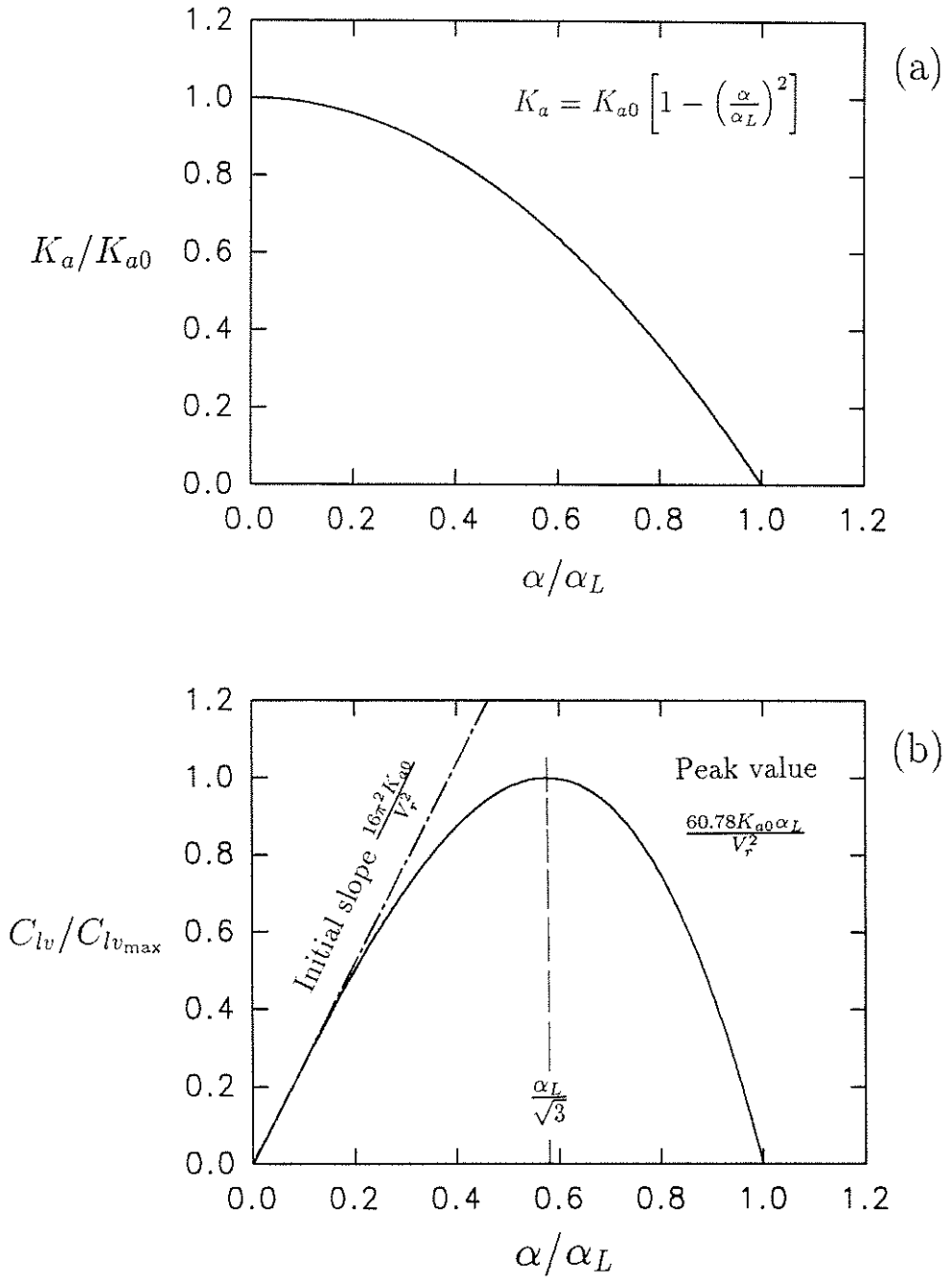

FIGURE 1.66: Dependence of negative aerodynamic damping with response amplitude incorporated in Vickery and Basu's model. (a); variation of K_a with α, (b); variation of C_{lv} with α.

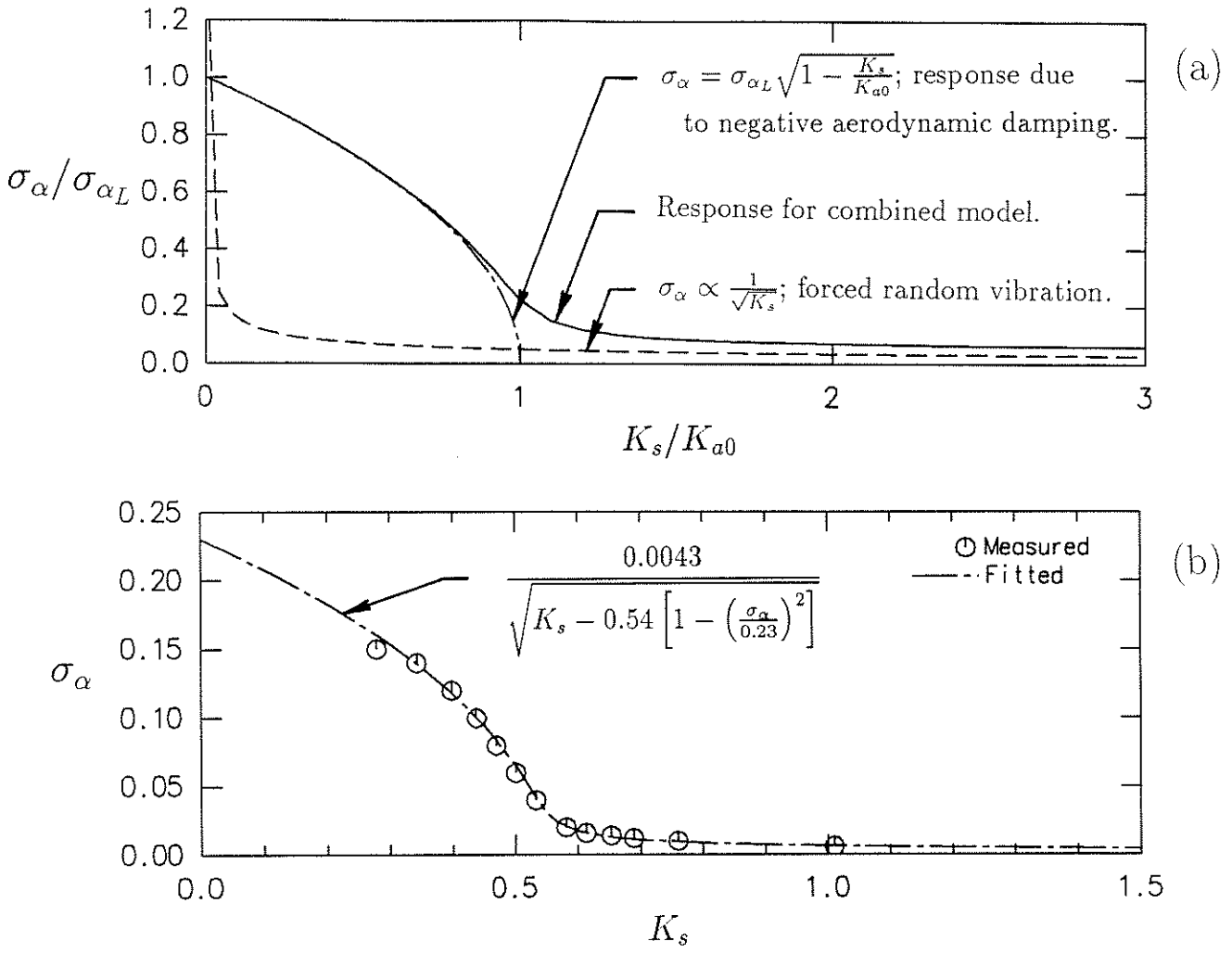

FIGURE 1.67: Variation of RMS response amplitude α with mass-damping parameter K_s predicted by Vickery and Basu's model. (a) Schematic, with shape of K_a–α curve. (b) Comparison of fitted curve with the form of equation (1.50) to Wootton's (1969) results for a cantilevered stack model with a rough surface and AR=11.5:1 (after Vickery and Basu 1983 c).

dependent on the random excitation provided by vortex shedding, and the negative aerodynamic damping has little effect, so that the RMS response amplitude is nearly inversely proportional to $K_s^{1/2}$ (or $\zeta_s^{1/2}$). As K_s drops to become comparable with K_{a0}, the response amplitude becomes very sensitive to changes in K_s, since the overall system damping approaches zero. When K_s drops below K_{a0}, the response amplitude is determined primarily by the shape of the K_a–α curve, and becomes almost independent of the size of the excitation provided by the random vortex shedding excitation.

A comparison between a fitted curve with the form of equation (1.50) and experimental results obtained on a model stack by Wootton (1969) is given in figure 1.67 (b). The fit (computed by Vickery & Basu) is good (except in the low K_s limit), but note that the three coefficients were fitted to the results rather than estimated from independent sets of experiments. The fitted value of $K_{a0} = 0.54$ is however in the range of what would be expected on the basis of tests made using forced oscillation (e.g. fig. 1.54).

In its simplified form (eq. (1.50)), the model predicts RMS response amplitudes but contains no information concerning the PDF of the response. It is known that the response PDF changes in form from that for a Gaussian process at high values of K_s to that for a sinusoidal process at low values (e.g. fig. 1.30). Vickery and Basu (1983 a) conducted numerical simulations in which second-order ordinary differential equations incorporating the appropriate form of nonlinear negative aerodynamic damping were driven by Gaussian noise. It was found that the response PDFs changed their form with K_s in the expected manner, and that the peak factor g could be approximated by

$$g = \sqrt{2}\left[1 + 1.2 \arctan\left\{0.75\left(\frac{K_s}{K_{a0}}\right)^4\right\}\right] . \tag{1.51}$$

The model is able to account for the increase in spanwise correlation of lift forces which is observed with increased oscillation amplitude. It is assumed that the motion-correlated forces are well-correlated along the span. In that case, since the motion-correlated forces initially increase with increased amplitude, the spanwise correlation increases above that which is provided by the random vortex shedding forces. Vickery (1978) showed that a model in which motion-correlated lift forces initially increase linearly with amplitude could account for the increases in spanwise correlation observed by Novak and Tanaka (1975, fig. 1.23). As a consequence of the eventual decrease in motion-correlated lift forces at the limiting amplitudes which is incorporated in the model, it also predicts that spanwise correlation should decrease back to that observed on a stationary cylinder as the amplitude of oscillation reaches a maximum.

The effect of large-scale turbulence on the variation of K_a with V_r has also been incorporated in the model, in a similar way to the quasi-steady variation in the spectra of lift force described in § 1.5.5. The PDF of the along-flow velocity fluctuations is convolved with the K_a–V_r curve for smooth flow. The results of this process are shown in figure 1.68, which was originally presented by Vickery and Basu (1983 a). No attempt is made to account for the possible influence of turbulence on the spanwise correlation of motion-correlated forces.

Shape of K_a–α curve

Now that the basic aspects of this kind of model have been introduced, some attention will be given to the assumptions on which it is based, in particular to the forms of the K_a–α and C_{lv}–α curves. Much of the discussion rests on the fact that, aside from the constants $V_r^2/(16\pi^2)$, the K_a–α curve is obtained from the C_{lv}–α curve by dividing by α. It is presumed that the C_{lv}–α curve passes through $C_{lv} = 0$ at $\alpha = 0$ (reasonable since the velocity-correlated lift must be zero when $\alpha = 0$) and, in the case of positive velocity-correlated forces at least, rises as α increases and finally drops to zero at some maximum amplitude (based on experimental observations that limiting amplitudes are reached as $K_s \to 0$).

Taking a polynomial form for the C_{lv}–α curve

$$C_{lv} = a_1\alpha + a_2\alpha^2 + a_3\alpha^3 + \cdots + a_n\alpha^n , \tag{1.52}$$

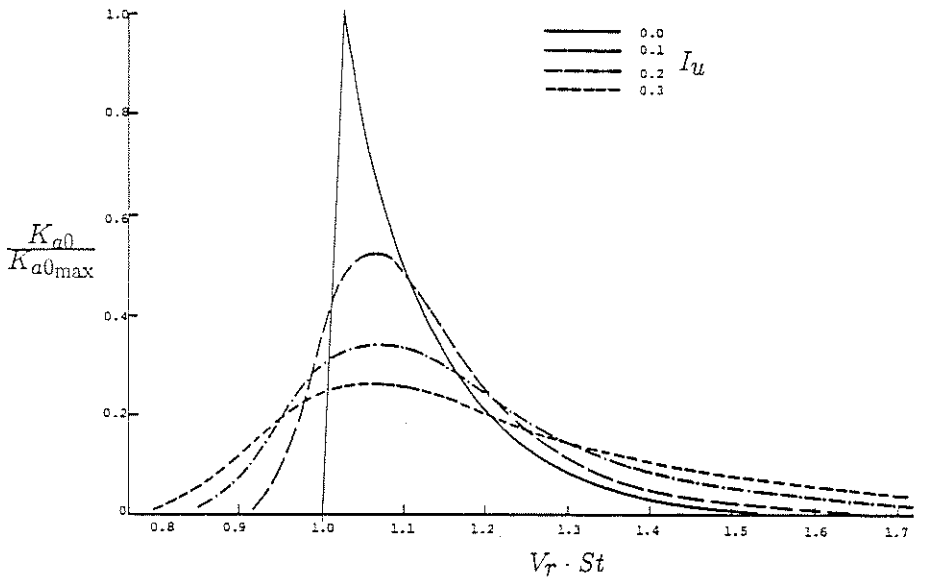

FIGURE 1.68: Quasi-steady variation produced by turbulence in the shape of the K_a–V_r curve predicted by Vickery & Basu's model (from Basu 1982).

it can be seen (with the aid of eq. 1.49) that the slope of the curve at the origin (a_1) is proportional to K_{a0}. Put another way, the requirement of a positive value of $\partial C_{lv}/\partial\alpha$ at the origin forces a positive value of K_{a0}. Next it can be seen that the slope of the K_a–α curve at $\alpha = 0$ is positive, zero or negative according to the sign of coefficient a_2. In equation (1.49), a_2 is zero and correspondingly the slope $\partial K_a/\partial\alpha$ in equation (1.47) is zero at the origin. Given the basic shape of the C_{lv}–α curve (rising from the origin, then falling) and a polynomial description, the characteristics of the K_a–α curve vary with the number of coefficients (a_i) used. If two coefficients are used then, for a quadratic

$$C_{lv} = a_1\alpha + a_2\alpha^2 \,, \tag{1.53}$$

a_1 must be positive and a_2 negative, leading to a form of the K_a–α curve which drops linearly from K_{a0} to zero as α increases. For a cubic, a_1 must be positive, a_2 zero and a_3 negative, as for Vickery and Basu's model.

This process could be continued by introducing more coefficients or using higher-order polynomials, but the point is that many different shapes and characteristics of the K_a–α and C_{lv}–α curves can be produced. From the point of view of producing a workable model, the less number of parameters the better. Support for the two-parameter form used by Vickery and Basu is provided by the curve fit shown in figure 1.67(b), however, other experimental evidence suggests different forms. Figure 1.69 presents results of tests conducted by Vickery and Watkins (1962) in which the mass-damping parameters of a series of geometrically-similar tubes were varied. Reynolds numbers were in the range 10^4–10^5. It can be seen that there was no rapid increase in α as K_s dropped below some critical value (as observed in Wooton's tests), so these results do not support the assumption that $\partial K_a/\partial\alpha = 0$ at low amplitudes. A curve similar to Vickery and Watkins' was presented by King (1977). Vickery and Watkins provided estimates of velocity-correlated coefficient of lift on the basis of the results in figure 1.69; these are presented in figure 1.70. It can be seen that the shape of the fitted curve does

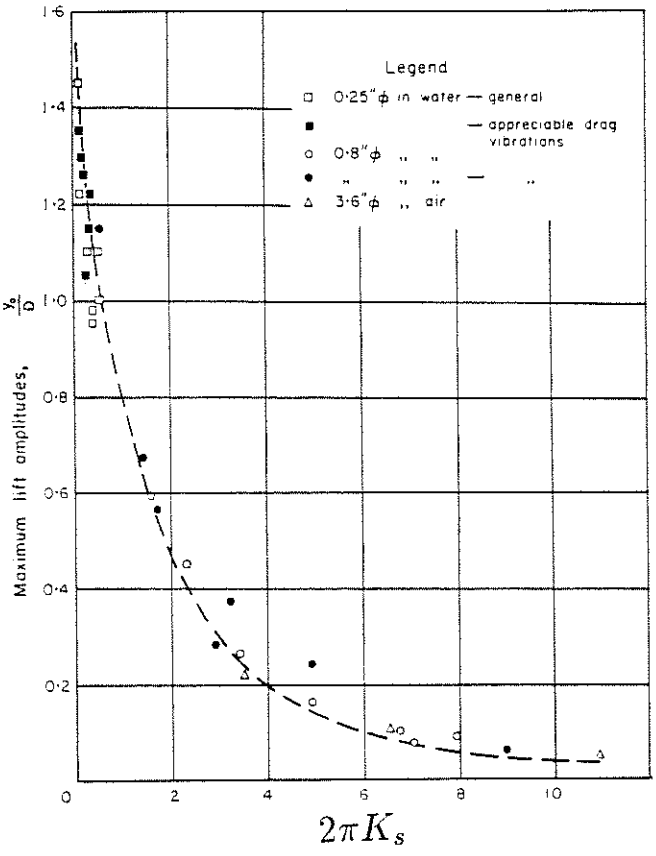

FIGURE 1.69: Test results for a series of geometrically-similar cylinders of varying mass-damping parameters. Maximum amplitude as a function of $2\pi K_s$. Vickery & Watkins (1962).

not match that of figure 1.66 (b) in detail. Finally, it may be noted that in figure 1.63 values of K_a initially drop as α increases, then rise again before falling to zero. Again, this is at variance with the model proposed by Vickery and Basu for the change of K_a with α.

1.7.6 Comparisons of Predictions with Observed Responses

The final test of a response prediction method is to compare its predictions with observed responses. Difficulties can arise because the observations of significant responses of full-size structures are comparatively few. The difficulties may be summarized as follows:

- There is often considerable uncertainty about the parameters of the structure and conditions in the flow. For instance, in most cases the structural damping can only be estimated, which is unfortunate because this is of prime importance. Hence there must be uncertainty when comparing predicted and observed responses, as to how much error can be attributed to the poor performance of the prediction method and how much to errors in the parameters input to the model.

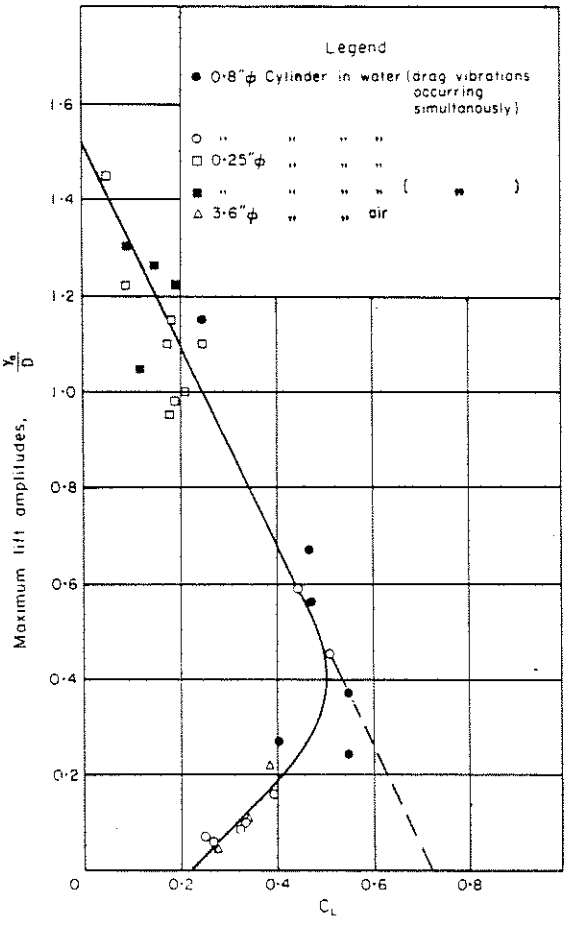

FIGURE 1.70: Coefficient of velocity-correlated lift (C_L) as a function of maximum cross-flow amplitude (y_0/D). Vickery & Watkins (1962).

- The observations of structural movement tend to leave out the majority of structures which do not show significant movement, so the observation set may be biased, for instance towards those structures which have unusually low structural damping.

- Since the Reynolds numbers for the full-size observations often lie above the range available in wind tunnel studies there is an obvious temptation to use the results to adjust model parameters for the high Reynolds number regime to force greater agreement between observation and prediction. This means that there is a lack of independence between the models and the observations, and so doubt about the applicability of the models to new situations.

A significant set of observed responses of full-sized steel stacks has been published by Pritchard (1984), and responses of concrete stacks have been compared with predictions by Vickery and Basu (1984). Pritchard's data covered isolated stacks, stacks which are reported as being members of groups of stacks, and stacks for which grouping was not reported.

ESDU compare the predictions of its methods with an edited set of Pritchard's data and that supplied by Vickery and Basu. The results are plotted as Figure 8.1 of ESDU Item 85038. Study of that figure indicates that the ESDU procedures tend on average to underpredict response in the transition region from *broad* to *narrow band* regimes, and to overpredict response in the limit as mass-damping drops to zero. Since the response data are not referenced in 85038 Table 8.1 which lists the publications from which the model parameters were derived, ESDU make it possible to conclude that the set of observations provides an independent check of their procedures.

To provide further comparison of ESDU predictions with the observed data, the observed and predicted responses from 85038 Table 8.2 are re-plotted here (fig. 1.71) as functions of the mass-damping parameter K_s. Comparing figures 1.71 (a) and (b) shows the considerable amount of scatter that exists between the predicted and observed responses. Some scatter is attributable to errors in estimates of model parameters and observed responses, as discussed above.

Basu and Vickery (1984) published a comparison of measured and predicted responses for five reinforced concrete stacks, using the negative-damping model described above. The coefficient of variation of 25% between predicted and measured responses is quite large, but because of the small sample size and the number of unknowns in their model it is difficult to draw definite conclusions from the comparison.

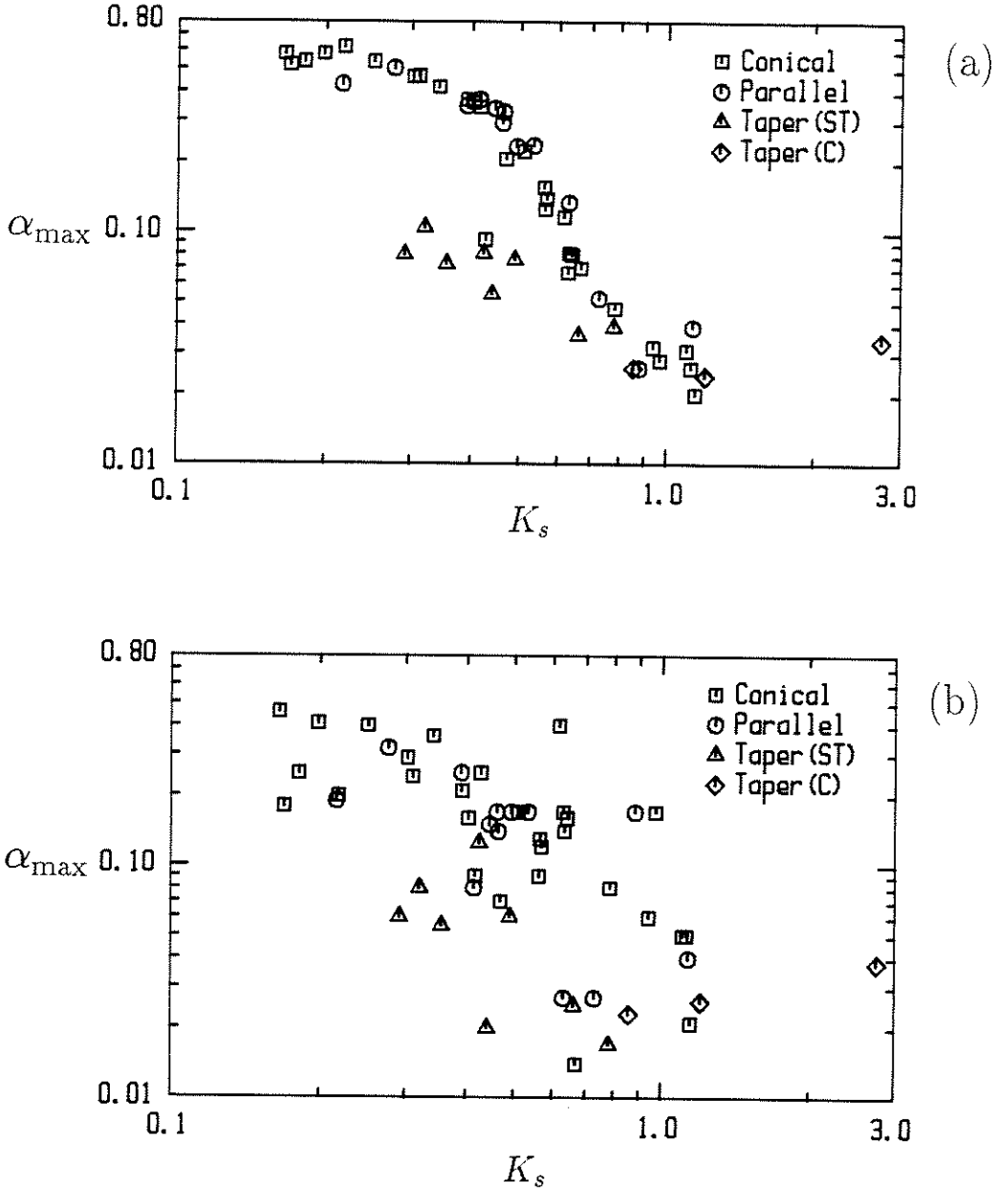

FIGURE 1.71: Comparison of (a); responses predicted by ESDU and (b); observed responses of chimney stacks as functions of K_s

1.8 Issues for Research

A number of topics which require further investigation arise from this review. The underpinning motivation is the desire to extend the range of data available for cross flow response prediction, and to improve the understanding of the vortex shedding process and interaction with cylinder motion, so that response prediction models may better match reality.

A recurring theme has been that the influence of turbulence on lift forces and vortex shedding needs more detailed investigation, particularly at super- and transcritical Reynolds numbers. For fixed cylinders, the general expectation (see e.g. Zdravkovich 1990, quoted in § 1.5.5), is that high levels of turbulence will reduce the extent of the supercritical regime and trigger a return to the organized vortex shedding of the transcritical regime at lower Reynolds numbers than is the case in smooth flow. The investigations of Cheung (1983, § 1.5.6) indicate that this is the case, but more detail concerning the spectral composition and spanwise relationships of sectional forces is required. For oscillating cylinders, the effect of turbulence on motion-correlated forces has never been directly investigated (see the discussions of §§ 1.4.5 and 1.7.5).

Concerning oscillating cylinders, several points for study have been noted, in addition to the one just referred to. The first is that uncertainty surrounds the oscillation amplitude required for lock-in in subcritical flows; some studies (e.g. Koopman 1967, § 1.4.1) have indicated that an amplitude threshold exists, below which lock-in does not occur. The relationship of motion-correlated forces and increased spanwise correlation needs attention: are they aspects of the same phenomenon, as suggested by Vickery and Basu (§ 1.7.5), or should they be addressed separately, as the correlation length models discussed in § 1.7.4 imply? The partition of lift forces into motion-correlated and residual parts has not been studied as a specific experimental issue; this partition is an assumption of negative damping models for prediction of cross flow response, as discussed in § 1.7.5. Wootton's investigation (1968, 1969; see § 1.4.1) suggested that imposition of cylinder motion could produce a return to organized vortex shedding in the supercritical Reynolds number regime in smooth flow past smooth cylinders, a suggestion that is accepted in at least one text (Sarpkaya & Isaacson 1981). This is of interest because of the implication that large amplitude cross flow oscillations are possible in the supercritical regime, in which it is usually assumed that cross flow forces are small.

It was decided that an experimental programme employing forced cross flow oscillations could examine these issues. For this purpose, a wind tunnel model was devised. The model was a 200 mm diameter, 900 mm long smooth cylinder containing six force transducers at which forces acting on thin (20 mm width) slices of cylinder could be measured. Oscillation amplitudes up to ±6 mm (3% diameter) could be obtained over a frequency range 10 Hz to 50 Hz. Reynolds numbers in the range 1×10^5 to 6×10^5 could be achieved in smooth and turbulent flows using the 2 m×1 m working section of the Monash University 450 kW wind tunnel. The comparatively moderate aspect ratio (4.5:1) and tunnel blockage (10%) are compromise values, allowing high supercritical Reynolds numbers in smooth flows and transcritical Reynolds numbers in turbulent flows.